Lithium dendrite growth through solid polymer electrolyte membranes

By

Katherine Joann Harry

A dissertation submitted in partial satisfaction of the

requirements for the degree of

Doctor of Philosophy

in

Engineering – Materials Science and Engineering

in the

Graduate Division

of the

University of California, Berkeley

Committee in charge:

Professor Nitash P. Balsara, Chair
Professor Andrew M. Minor, Chair
Professor Ronald Gronsky
Professor Bryan D. McCloskey

Spring 2016

Lithium dendrite growth through solid polymer electrolyte membranes

by Katherine Joann Harry

Abstract

Lithium dendrite growth through solid polymer electrolyte membranes

by

Katherine Joann Harry

Doctor of Philosophy in Materials Science and Engineering

University of California, Berkeley

Professor Nitash P. Balsara, Chair

Professor Andrew M. Minor, Chair

The next generation of rechargeable batteries must have significantly improved gravimetric and volumetric energy densities while maintaining a long cycle life and a low risk of catastrophic failure. Replacing the conventional graphite anode in a lithium ion battery with lithium foil increases the theoretical energy density of the battery by more than 40%. Furthermore, there is significant interest within the scientific community on new cathode chemistries, like sulfur and air, that presume the use of a lithium metal anode to achieve theoretical energy densities as high as 5217 W·h/kg. However, lithium metal is highly unstable toward traditional liquid electrolytes like ethylene carbonate and dimethyl carbonate. The solid electrolyte interphase that forms between lithium metal and these liquid electrolytes is brittle which causes a highly irregular current distribution at the anode, resulting in the formation of lithium metal protrusions. Ionic current concentrates at these protrusions leading to the formation of lithium dendrites that propagate through the electrolyte as the battery is charged, causing it to fail by short-circuit. The rapid release of energy during this short-circuit event can result in catastrophic cell failure.

Polymer electrolytes are promising alternatives to traditional liquid electrolytes because they form a stable, elastomeric interface with lithium metal. Additionally, polymer electrolytes are significantly less flammable than their liquid electrolyte counterparts. The prototypical polymer electrolyte is poly(ethylene oxide). Unfortunately, when lithium anodes are used with a poly(ethylene oxide) electrolyte, lithium dendrites still form and cause premature battery failure. Theoretically, an electrolyte with a shear modulus twice that of lithium metal could eliminate the formation of lithium dendrites entirely. While a shear modulus of this magnitude is difficult to achieve with polymer electrolytes, we can greatly enhance the modulus of our electrolytes by covalently bonding the rubbery poly(ethylene oxide) to a glassy polystyrene chain. The block copolymer phase separates into a lamellar morphology yielding co-continuous nanoscale domains of poly(ethylene oxide), for ionic conduction, and polystyrene, for mechanical rigidity. On the macroscale, the electrolyte membrane is a tough free-standing film, while on the nanoscale, ions are transported through the liquid-like poly(ethylene oxide) domains.

Little is known about the formation of lithium dendrites from stiff polymer electrolyte membranes given the experimental challenges associated with imaging lithium metal. The objective of this

dissertation is to strengthen our understanding of the influence of the electrolyte modulus on the formation and growth of lithium dendrites from lithium metal anodes. This understanding will help us design electrolytes that have the potential to more fully suppress the formation of dendrites yielding high energy density batteries that operate safely and have a long cycle life.

Synchrotron hard X-ray microtomography was used to non-destructively image the interior of lithium-polymer-lithium symmetric cells cycled to various stages of life. These experiments showed that in the early stages of lithium dendrite development, the bulk of the dendritic structure was inside of the lithium electrode. Furthermore, impurity particles were found at the base of the lithium dendrites. The portion of the lithium dendrite protruding into the electrolyte increased as the cell approached the end of life. This imaging technique allowed for the first glimpse at the portion of lithium dendrites that resides inside of the lithium electrode.

After finding a robust technique to study the formation and growth of lithium dendrites, a series of experiments were performed to elucidate the influence of the electrolyte's modulus on the formation of lithium dendrites. Typically, electrochemical cells using a polystyrene – *block* – poly(ethylene oxide) copolymer electrolyte are operated at 90 °C which is above the melting point of poly(ethylene oxide) and below the glass transition temperature of polystyrene. In these experiments, the formation of dendrites in cells operated at temperatures ranging from 90 °C to 120 °C were compared. The glass transition temperature of polystyrene (107 °C) is included in this range resulting in a large change in electrolyte modulus over a relatively small temperature window. The X-ray microtomography experiments showed that as the polymer electrolyte shifted from a glassy state to a rubbery state, the portion of the lithium dendrite buried inside of the lithium metal electrode decreased. These images coupled with electrochemical characterization and rheological measurements shed light on the factors that influence dendrite growth through electrolytes with viscoelastic mechanical properties.

Next, the morphology of lithium dendrites formed upon many charge and discharge cycles were compared to the morphology of those grown upon a continuous charge using a combination of X-ray and electron microscopy techniques. When cycled, the lithium dendrite morphology consisted of multiple interconnected lithium globules that amassed to form a structure that punctured the electrolyte causing the cell to fail by short-circuit. When charge is passed in only one direction until the samples fails by short-circuit, the dendrite morphology is markedly different. Instead of observing a multi-globular morphology, a single lithium-filled globule encased in a polymer sac expands until it touches the counter-electrode. These blunt structures formed in solid polymer electrolytes are in stark contrast to the needle-like morphologies observed in lithium dendrites formed in liquid electrolyte systems.

Time-resolved hard X-ray microtomography was used to monitor the internal structure of a symmetric lithium-polymer cell during galvanostatic polarization. The microtomography images were used to determine the local rate of lithium deposition, i.e. local current density, in the vicinity of a dendrite growing through the electrolyte. Measurements of electrolyte displacement enabled estimation of local stresses in the electrolyte. At early times, the current density was maximized at the dendrite tip, as expected from simple current distribution arguments. At later times, the current density was maximized at the dendrite perimeter. We show that this phenomenon is related to the local stress fields that arise as the electrolyte is deformed. The local current density, normalized for the radius of curvature, decreases with increasing compressive stresses at the

lithium-polymer interface. To our knowledge, our study provides the first direct measurement showing the influence of local mechanical stresses on the deposition kinetics at lithium metal electrodes.

Table of Contents

List of Figures

List of Tables

Acknowledgements

I would like to start by thanking my parents. Their support in both my academic and personal endeavors through my childhood and my young adult life has been unwavering. Throughout the challenges of graduate school, they consistently supported me with encouraging conversation, humor, and love. Their interest in my work enabled me to take a step back from my day-to-day problems and appreciate the role of my research in the broader sphere. They also provided a consistent reminder that I get to work on really amazing things and with truly extraordinary people. I've had so much joy in my life and much of it can be attributed to my parents. I am enormously grateful to them for that.

My siblings have also greatly supported me in my time at Cal. I am consistently amazed by my brother and his ability to build just about anything he puts his mind to. Similarly, my sister's creativity and eye for beauty opens up an alternate view of the world to me. I've always looked up to my brother and sister and they have shaped me in more ways than I can count. Thank you for taking care of your little sister! I love you both so very much. Also, Tina, you are like a sister to me. You have been such a supportive friend for so many years. I don't know how we still manage to talk on the phone for hours even now that we are both adults, but it is awesome! I value your friendship so much, and I look up to you for your incredible strength, empathy, and independence.

One of the best decisions of my life so far was to choose Nitash as my research adviser. His excitement about our research is contagious, and he is talented at seeing where our work fits into the bigger picture. He truly cares about the academic and personal well-being of all of the students in his lab, and his caring nature helps ease many of the stresses that are seemingly inherent in our challenging Ph.D. program. He gave me space to go in my own direction with my research, but provided guidance when I became stuck in the details of my work. I hardly knew what a polymer was when I joined this lab, but I feel like my eyes have been opened to this fascinating new world and I thank Nitash for introducing me to this field. I look up to Nitash as a scientist and a mentor and hope that I will someday touch people's lives as he has. I would also like to acknowledge my Materials Science adviser Andy Minor. Andy is one of the people who told me that Nitash was a great person to work for, which largely influenced my decision to join his group. Furthermore, he has been supportive of me from a distance through our soft matter electron microscopy group. I especially needed a window into the Materials Science department when I was preparing for my preliminary exam and qualifying exam and Andy always made himself available to help me when I needed it.

When I started working in our lab, I was mentored by Dan Hallinan. He showed me how to make samples, came with me to the beamline for the first time, and helped me do my first experiments in graduate school. He was incredibly generous with his time, and I am immensely grateful to him for that. I could not have succeeded in graduate school without his mentorship. Shortly after joining the lab, I was assigned a desk next to Scott Mullin. That was a lucky day for me. Since Scott was on his way out of graduate school, he had years of experience under his belt and took the time to pass on a massive amount of brutally honest advice. He steered me away from certain projects and encouraged me when he thought I had reasonable ideas. Now that I am finishing graduate school, I look forward to working with Scott again at Seeo. Shrayesh also served as an important mentor for me while we were in graduate school together. He is extraordinarily patient, encouraging, and kind. His research was truly amazing and yet he always carried himself with humility. I feel fortunate to have had the chance to work with Shrayesh. Alex Teran was also a highly influential labmate. He seemed to know everything about batteries/renewable energy and

was so efficient in the lab. I knew that if I didn't understand the technical details of somebody's work, I could count on Alex to explain it to me. Nick Young was a solid figure in our lab. No matter how early I came into lab, Nick would already be sitting at his desk working. He was generous with his time and very patient when I would ask him questions. I really appreciate all of his help. Similarly, David Wong was a staple of the lab for my first few years at Cal. I remember him giving me a tour of our labs in Tan Hall before I decided to join the group, and our tour went for more than an hour! He was very patient with me as I barraged him with hundreds of questions about the group, and his easygoing and supportive attitude continued after I joined the group. I remember Keith teaching me how to use the microtome shortly after I joined the lab. He made really boring situations fun and was always approachable and willing to answer any questions that I had. Greg Stone worked on a project that eventually led to my research topic. He was very honest and direct with me about the challenges inherent to this area of research. His honesty is what led me to seek out alternative approaches to study lithium dendrite growth and saved me from what could have been a grueling graduate school experience.

My entering class of labmates feel like family to me at this point. It's difficult for me to find the words to thank Chaeyoung for everything she is. She is such an incredible friend. She took care of me after my surgery, listens to me when I'm happy and when I'm grumpy, and is always up for getting together to do something fun. I really can't express how grateful I am to have her in my life. Mahati made my graduate school experience extra lovely. She is so witty and positive. I feel like I'm missing out on a little bit of life whenever I am not around her. Jacob is the best cook I've ever met. I will never forget his vegetarian chili. Really. Never. He is also extra fun to be around. I could always count of Jacob to listen when I needed someone to talk to, and he is astonishingly empathetic (likely a consequence of having a zillion siblings) and thoughtful. I wish I could have spent more time listening to Kevin play the guitar and piano. He is so musically talented in addition to his knack for science. He is always laughing and is a genuinely wonderful person to be around.

I've also had the opportunity to learn huge amounts from the younger students in our lab. Doug and Alex W are both so witty. Their puns would strike unexpectedly and make me laugh so hard! My APS hotel-buddy Adri shaped the safety culture in our lab and kept us all in line. She works so hard in lab and I'm very excited to see what she will discover. I've been highly impressed by the progress that Danielle and Ksenia are making toward really understanding the factors that influence ionic conductivity in polymers. Both Ksenia and Danielle have extraordinary intellect and work ethic. Rita is a little ball of energy in the lab. She is always bursting at the seams with questions and thoughts, and I am consistently impressed by her scientific mindset.

The post docs in our group also shaped my graduate school experience. My cubicle-mate, Chelsea, put up with years of me pestering her while she was trying to get real work done. I really appreciate her patience with me. Also, I loved getting to see all of her beautiful TEM images! I really had the best seat in the lab for viewing beautiful micrographs. I loved having Spanish speaking lunches with Irune. I am so impressed by the plethora of unique electrolytes that Irune has synthesized in her time here. She is a polymer electrolyte wizard! Didier and Mahesh are the glue that keeps our battery labs from falling apart. Didier's jovial spirit persists through normal working hours to ridiculous overnight beamtimes. I don't know how he does it. Mahesh always makes himself available when I have questions or problems with equipment in lab. I'm very grateful for his patience. I only began working with Hee Jeung recently, but she is a joy to be

around and has an incredible work ethic. I'm excited to learn about the things she will discover in the next few years.

I also had the opportunity to work with two stellar undergraduate students while here. Nicole is outstanding in so many ways. She is a highly independent researcher and is quick to pick up new skills in the lab. She took charge of her research project and drove it to completion as evidenced by her well-deserved first author paper. While her academic skills are phenomenal, I've learned to appreciate her even more as a friend. She took me on my first backpacking trip and is always up for a hike. She is amazingly humble and is a very genuine and fun person to be around. I am so glad that Nicole decided to do research with me. I've learned an incredible amount from her and have also made a wonderful friend. Vincent has also been a joy to work with. He came into our lab excited to get experience using a variety of different characterization tools. He is a fantastic listener and always has insightful questions for me. I hope that both Nicole and Vincent will have lots of success when they go on to graduate school. I'm excited to see what new science they come up with!

Our first year students this year have really blown me away. I have had so much fun training Jackie for the last few months. In addition to being hilarious, she is patient and eager to learn. I am excited to see what she ends up working on in graduate school. She's off to a great start! It's also been great getting to know Whitney and Deep. Whitney's ability to remember song lyrics blows me away and Deep has such an awesome laugh! They make a fantastic trio, and I hope that they will support each other through the ups and downs of graduate school and come out the other side feeling that they learned a lot and maybe even discovered some new things about polymer physics.

In addition to my work friends, I'd like to acknowledge all of my friends outside of work who have supported me through countless hikes, dinners, and long conversations. Graduate school can be difficult at times, and I am fortunate to have a good group of friends to lean on, learn from, and enjoy life with.

Chapter 1 – Introduction

Transitioning from a fossil fuel based transportation and grid infrastructure to a low-emission, renewable-energy based system requires high performance, reliable energy storage solutions [1,2]. The primary problems precluding the large-scale adoption of electric vehicles today are vehicle cost and range anxiety: both are problems associated with the battery [3]. With help from industry partners, the Department of Energy's Vehicle Technologies Program published a series of performance targets for rechargeable batteries that would help enable a transition to electric vehicles [4]. As the specific energy and energy density of the battery pack increases, the amount of material required for each W·h of energy decreases. Therefore, one approach to creating a rechargeable battery that meets or exceeds these targets is to design electrochemical cells that have a significantly higher energy density than a traditional lithium ion battery while preserving the use of earth-abundant materials.

1.1 Specific energy of rechargeable batteries

The specific energy of an electrochemical cell is a function of the energetic difference between the active material in the anode and the cathode, and the mass of the components in the cell. The theoretical specific energy of the cell can be calculated in a couple of ways. First, one can calculate the Gibbs free energy of reaction, ΔG^0, by taking the difference between the Gibbs free energy of the products and the Gibbs free energy of the reactants as shown in equation (1).

$$\Delta G^0 = \sum_{reactants,i} s_i \Delta G^0_{f,i} - \sum_{products,i} s_i \Delta G^0_{f,i} \text{ [5]} \quad (1)$$

where s_i is the stoichiometric coefficient of component i in the reaction and $\Delta G^0_{f,i}$ is the Gibbs free energy of formation of component i. The theoretical specific energy, E, is then calculated by dividing the Gibbs free energy of reaction divided the molar masses, M_i, of the reactants.

$$E = \frac{\Delta G^0}{\sum_{reactants,i} s_i M_i} \text{ [5]} \quad (2)$$

Note that this approach does not include the masses of the electrolyte, separator, binder, current collectors, or inactive material in the battery. Therefore, the practical energy density of a battery is typically on the order of three times smaller than the theoretical energy density [5].

A second method one can use to calculate the specific energy of an electrochemical cell is to integrate the instantaneous power of the cell over the full discharge time and divide this by the mass of the active materials in the cell, m_{cell} [6,7].

$$E = \frac{1}{m_{cell}} \int_0^{t_d} IV dt \text{ [6]} \quad (3)$$

where *I* is the superficial current density, V is the cell potential, and t_d is the time to discharge the cell.

A conventional lithium ion battery consists of a graphite anode and a metal oxide cathode separated by a liquid or gel electrolyte [8,9]. Figure 1.1 shows the theoretical specific energy calculated using equation (2) for a variety of battery chemistries. The series color indicates the anode material used in the battery. Table 1.1 tabulates the specific energy and the energy density for the battery chemistries shown in Figure 1.1. If one were to simply replace the graphite anode in a lithium ion battery with a lithium metal foil, the theoretical energy density of the

electrochemical cell would increase by 40%. Additionally, next generation cathode chemistries like sulfur and air (oxygen) presume the use of a lithium metal anode to achieve theoretical specific energies that approach that of octane [5,10-12].

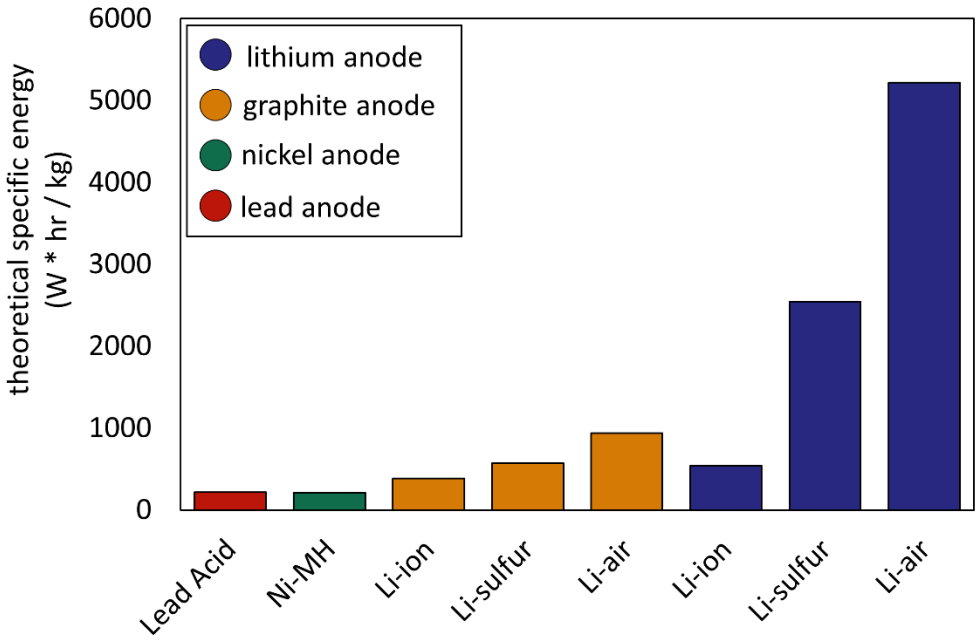

Figure 1.1 The theoretical specific energy calculated using equation (2) is shown for a variety of rechargeable battery chemistries.

Battery chemistry	**specific energy (W*h/kg)**	**energy density (W*h/l)**
Lead Acid	218	929
Ni-MH	216	1386
Li-ion (graphite anode)	385	1168
Li-sulfur (graphite anode)	576	1473
Li-air (graphite anode)	939	2170
Li-ion (lithium anode)	545	1595
Li-sulfur (lithium anode)	2548	3665
Li-air (lithium anode)	5217	5997

Table 1.1 The theoretical specific energy and energy density is tabulated for a variety of rechargeable battery chemistries.

1.2 Problems when lithium metal anodes are used with traditional liquid electrolytes

Unfortunately, lithium metal is highly unstable against traditional carbonate liquid electrolytes [13-15]. Upon electrochemical cycling, the electrolyte reacts with lithium metal to form a solid electrolyte interphase (SEI) layer [16,17]. When traditional liquid electrolytes are used, the SEI layer is brittle resulting in the unstable layer crumbling apart as the battery is cycled. This unstable SEI layer results in significant heterogeneity in the current density profile across the lithium metal anode. Since the ionic current density is heterogeneously distributed across the lithium metal surface, small protrusions of lithium form as lithium is preferentially deposited in regions where the SEI layer is broken. Once a protrusion forms, ionic current concentrates at the protrusion tip resulting in the formation of mossy and needle-like dendrites that can cause the battery to fail by short-circuit [8]. Since traditional liquid electrolytes are highly flammable [18], the rapid release of energy that coincides with an internal short-circuit in the battery can cause catastrophic cell failure and a fire [19]. As applications demand a higher number of electrochemical cells (e.g. an electric car vs. a cell phone), the probability of catastrophic failure increases. For these reasons, lithium metal is considered an unsafe anode material for use in conventional rechargeable lithium ion batteries [9].

In 1973, poly(ethylene oxide) (PEO) was shown to efficiently conduct lithium ions in its melt state [20]. Since then, a large body of research has focused on studying the ionic transport properties of polymer electrolytes as a safe alternative to traditional liquid electrolytes [21-25]. When PEO is cycled with a lithium metal anode, the SEI layer that forms is an elastomer [8]. This stable interface that forms allows for a more homogeneous current distribution at the lithium metal anode. However, lithium dendrites still form and result in electrochemical cell failure by short-circuit [26-33]. Fortunately, PEO is significantly less flammable than traditional liquid electrolytes, so cell failure is not catastrophic. Given the large energy densities that are accessible when using a lithium electrode, there is considerable interest in developing a lithium metal – electrolyte system that can cycle safely and reliably.

1.3 Dendrite growth

There are several factors that contribute to the formation and growth of lithium dendrites. Before getting into the details of dendrite growth from electrolytic solutions, let's discuss classical dendrite growth in the solidification of metals. When one cools a molten metal below its melting point, there is a thermodynamic driving force for its solidification. The greater the undercooling, the higher the driving force. Opposing the formation of the solid phase is an increase in surface energy associated with the new solid-liquid interface, sometimes requiring significant undercooling to initiate solidification. The temperature gradient ahead of the liquid-solid interface during such undercooling is key to the morphological development of the solid phase [34-38]. As shown in Figure 1.2, when the gradient is positive, Figure 1.2 a, fluctuations in the shape of the liquid-solid interface are inhibited, retaining a planar interface. But when the gradient is negative. Figure 1.2 b, fluctuations are favored, as solid protrusions grow very rapidly into deeply undercooled liquid. The resulting solid phase is known as "cellular" when the protrusions are smooth-walled, or "dendritic" when the protrusions develop side branches [39]. In severe temperature gradients, or in the case of "constitutional supercooling" of alloys, branching can be considerable, including secondary, tertiary, and even higher order [40].

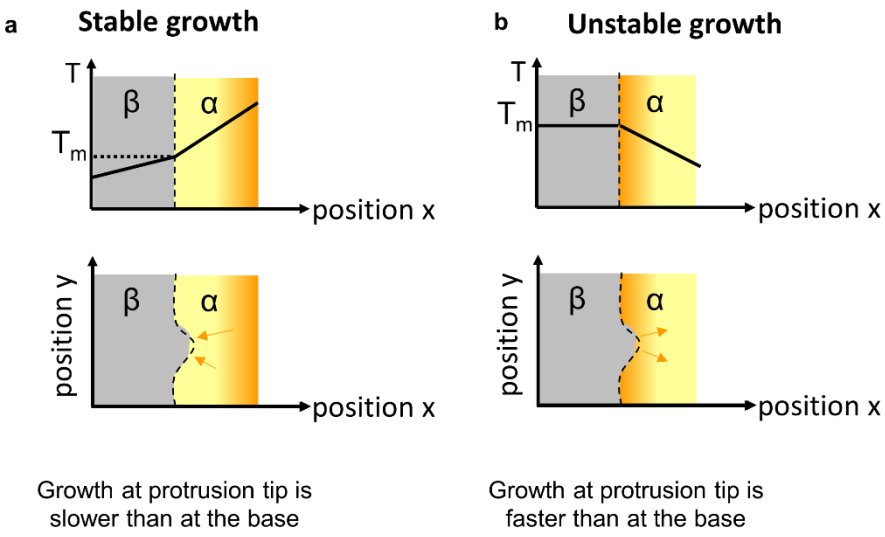

Figure 1.2 **Thermal dendrite growth a** When a metal solidifies, the propensity of the metal to form dendrites depends on the temperature gradients present in the liquid phase. **a** If the liquid phase, α, has a temperature gradient that increases at positions ahead of the solidification front, the metal will not form dendrites. **b** If the liquid phase, α, is undercooled, there will be a larger thermal driving force for solidification at positions on the solid phase, β, that protrude into the liquid phase resulting in the formation of dendrites.

In electrochemical systems, metals can solidify upon the reduction of salts from ionic solutions [41,42]. In the case of a lithium ion battery with a lithium metal anode, lithium ions in the electrolyte combine with an electron at the anode surface when the battery is charging, to form a layer of lithium metal. Ideally, the lithium metal anode would thicken evenly as lithium is deposited on the anode. However, similarly to the case of undercooled molten metals, the lithium metal preferentially deposits on the tip of protrusions yielding structures that propagate in length, like a growing needle, across the electrolyte and cause the cell to fail by short-circuit [43]. Salt concentration gradients electric field gradients in electrochemical systems are analogous to the thermal concentration gradients that favor fluctuations at the liquid-solid interface in thermal processing. Given their similarity to the dendrites formed upon the thermal solidification of metals, the protrusions formed in electrochemical systems are frequently referred to as dendrites. It is worth noting that classical dendrites are branched like trees, but structures referred to as dendrites in the body of literature surrounding electrochemical dendrite growth are frequently unbranched [29]. Moreover, the morphology of the protrusions observed growing through solid block copolymer electrolytes were not branched and are more similar to cellular morphologies. However, given the ubiquity of the term "lithium dendrite" used to describe any structure that causes a battery to fail by short-circuit in the electrochemical literature, the term lithium dendrite is used interchangeably with lithium globule throughout the text. A detailed description of the morphology of these structures is given in Chapter 5.

There are several factors that are thought to contribute to the formation of dendrites, or any non-plane front morphology of lithium, in electrochemical systems. First, in electrostatic systems, electronic charge tends to concentrate at sharp edges, or regions of low radius of curvature on

electronically conductive materials in an electric field [44-46]. In the case of an electrodynamic lithium ion battery, the electrons can move significantly faster through the lithium metal ($\sigma_{e,Li}$ = 10.7×10^6 S/cm [47]) than the rate at which lithium ions are transported to the electrode surface ($\sigma_{i,SEO} = 1 \times 10^{-4}$ S/cm [22]) for a given voltage. Therefore, one would expect for the concentration of electronic charges to be higher at a protrusion tip than elsewhere on the electrode. A higher concentration of electrons would likely yield an increased rate of lithium ion reduction at the dendrite tip.

Secondly, when a battery is charging, both the cation and anion that form the salt in the electrolyte are influenced by migration and diffusion [48]. Since lithium ions are consumed at the lithium anode during the charging step, the concentration of lithium ions is smaller at the anode surface than it is in the electrolyte, as shown in Figure 1.3 [43]. Therefore, if a protrusion forms on the lithium metal anode, the driving force for electrochemical reduction of lithium ions is higher in regions with a higher concentration of lithium ions, or at the tip of the dendrite. This problem can be eliminated by tethering the anion to the backbone of the electrolyte, forcing the salt concentration to be uniform throughout the battery [24].

Finally, as the dendrite grows closer to the counterelectrode, the ohmic losses at the dendrite tip are lower than elsewhere on the electrode. This results in a larger amount of energy available to reduce ions at the tip of the dendrite compared to other places on the electrode, contributing to dendrite growth.

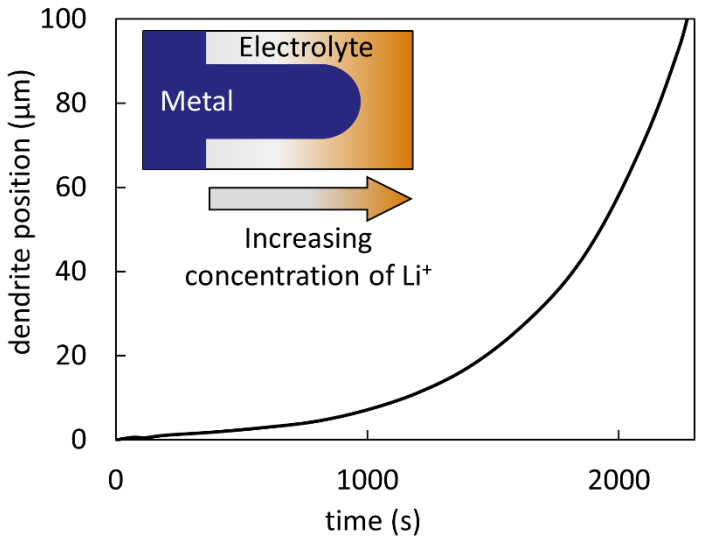

Figure 1.3 **Influence of salt concentration gradient on electrochemical dendrite growth.** A figure reproduced from reference [40] showing the results of a model predicting the position of a lithium dendrite as it protrudes into an electrolyte. As a battery using a conventional electrolyte with a transference number less than unity is charged, the concentration of lithium ions is larger at the cathode interface than at the anode interface as shown in the inset. This results in a larger driving force for the reduction of lithium ions at the tip of protrusions on the anode. Given this phenomena, one would expect the rate at which a protruding dendrite grows across the electrolyte to increase with time.

1.4 Methods to suppress dendrite growth

In 2005, Charles Monroe published a study where he modeled the growth of lithium dendrites through a stiff electrolyte [49]. In the case of a stiff polymer electrolyte, one would expect for there to be a resistance to the electrochemical reduction of an ion in a region where the electrolyte is experiencing high strain, and consequently, high stress. As a dendrite pushes into the electrolyte, the electrolyte will experience high strain at the tip of the dendrite. If the modulus of the electrolyte is high enough, one would expect for the reduction of lithium ions at the dendrite tip to slow to a rate that is comparable to other regions of the sample resulting in a uniform thickening of the lithium electrode upon charge. Monroe's models suggest that a shear modulus twice as high as that of lithium metal is required to slow the deposition rate of lithium ions at a protrusion to the rate elsewhere on the electrode. While a shear modulus of this magnitude would be difficult to achieve in a polymer electrolyte, one can create polymer electrolytes that are considerably stiffer than a conventional PEO electrolyte [23].

Good electrolytes are typically liquids or soft polymers because the motion of the molecules helps to move the ions through the electrolyte yielding reasonable ionic conductivity [50]. Since the rate at which polymer electrolytes can transport ions is a function of the segmental chain motion of the polymer, soft, liquid-like polymers, like rubbery PEO, are typically used as electrolytes. Stiff, glassy electrolytes, like polystyrene (PS), have low segmental chain motion and do not solvate electrolytic salts and are thus ineffective as electrolytes. In order to design an electrolyte that has a reasonably high modulus while still conducting ions, one can take advantage of a block copolymer's ability to self-assemble into co-continuous domains of two separate polymer blocks [51]. In this work, I use a 240 – 260 kg/mol block copolymer of poly(ethylene oxide) and polystyrene mixed with lithium bis(trifluoromethane)sulfonimide (LiTFSI) salt. This polymer self-assembles into a lamellar morphology with domains on the order of 241 nm. A scanning electron micrograph showing the lamellar morphology of this block copolymer is shown in Figure 1.4. The lithium ions are solvated by and transported in the liquid-like PEO domains while the PS provides mechanical rigidity to the electrolyte resulting in a solid, free-standing electrolyte film.

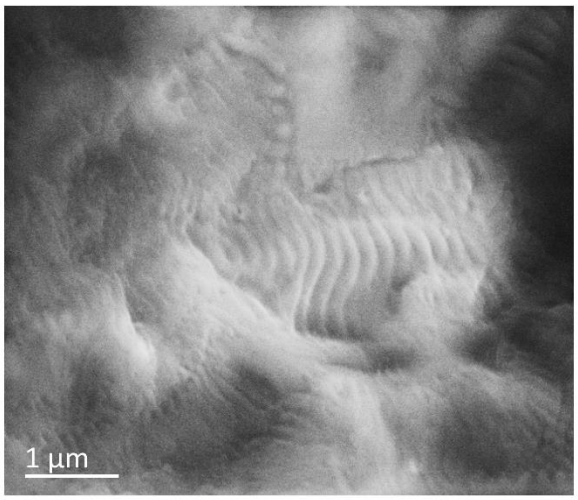

Figure 1.4 A scanning electron micrograph of a 240 – 260 kg/mol block copolymer of poly(ethylene oxide) and polystyrene mixed with lithium bis(trifluoromethane)sulfonimide

(LiTFSI) salt on lithium foil. The block copolymer self-assembles into a lamellar morphology with an average domain spacing of 241 nm.

1.5 Methods used to study lithium dendrite growth

A variety of experiments have been performed studying the stability of lithium metal against liquid electrolytes [52,53]. However, it is more difficult to study the formation and growth of lithium dendrites through solid electrolytes because cell disassembly is non-trivial. In order to view lithium dendrites grown in a solid polymer electrolyte using scanning electron microscopy, one must either dissolve the electrolyte away and carefully separate the two electrodes from one another without disturbing the morphology of the electrode [30], or make a battery that can function inside of the microscope and hope that a dendrite forms on the surface of the electrolyte where it is visible [29]. Imaging dendrite growth with transmission electron microscopy is even more challenging because it requires either sectioning a large sample into slices on the order of 100 nm thick and hoping to see a dendrite (a classic needle in a haystack problem), or designing a 100 nm thick battery that can cycle inside of the microscope, a heroic task [54].

While these experiments are highly challenging, some groups have had success using these techniques to capture a glimpse of the process by which lithium dendrites form in these systems [55]. However, the techniques are not robust, and it is difficult to know how the sample geometry, or the act of disassembling the samples influenced the results. Therefore, it was important to find a robust technique for imaging morphological changes that occur inside of a solid state battery in order to more thoroughly study lithium dendrite growth in solids.

1.6 Hard X-ray microtomography

Given the challenges inherent to using electron microscopy to study lithium dendrite growth, several non-destructive techniques have been used to study the phenomena. These include nuclear magnetic resonance [56], magnetic resonance imaging [57], and optical microscopy [31]. In this work, synchrotron hard X-ray microtomography is used to non-destructively image the interior of solid-state, lithium metal based electrochemical cells. The advantage of this technique is that conventional battery geometries can be placed directly into the X-ray beam with only minor modifications to the packaging design. This allows one to monitor the three-dimensional morphology of the interior of the battery to a resolution of about 1 μm^3 as it is electrochemically cycled. To image a sample using synchrotron hard X-ray microtomography at the Advanced Light Source (ALS) [58], the sample is illuminated by a beam of monochromic X-rays at a selected energy in the range of about 10 – 40 keV. The beam spot is 40 mm wide and about 4.6 mm tall. A portion of the incident beam is transmitted through the sample where it passes through a scintillator where it is converted to optical light. The optical light is then magnified by a traditional optical lens and the radiograph image is captured on a CCD screen. Radiograph images are taken at over a thousand angles as the sample rotates 180° about a single axis of rotation as shown in Figure 1.5. The radiograph images are processed using an algorithm based on the Fourier Slice Theorem. After processing, the two-dimensional radiographs are converted into a stack of three-dimensional tomographic slices. The stack of tomographs form a three-dimensional X-ray absorption map of the sample. Details of the reconstruction algorithm can be found in reference [59].

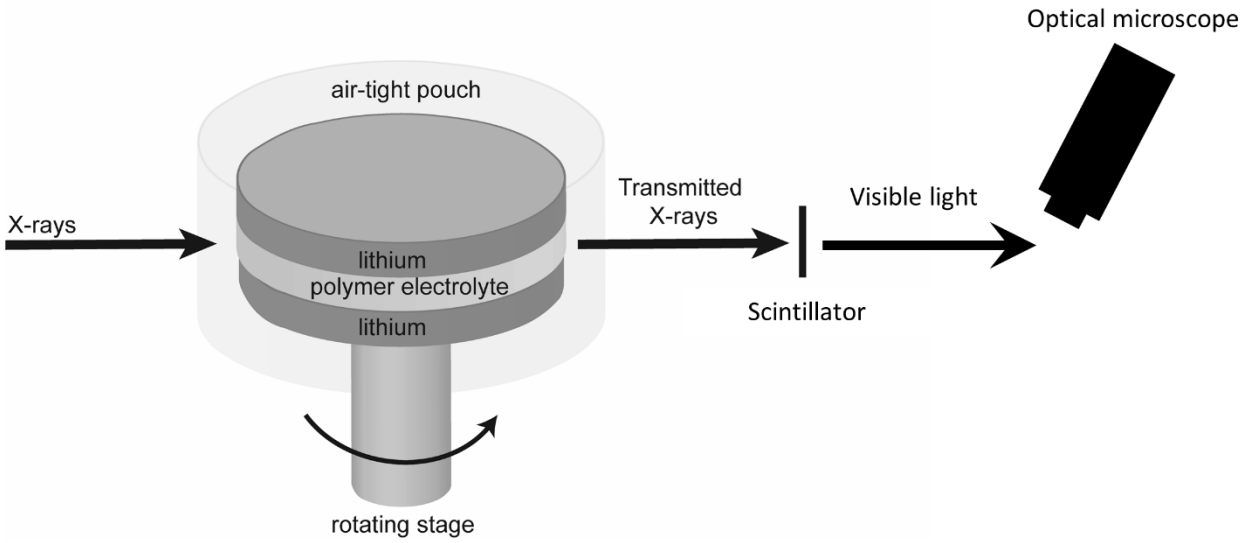

Figure 1.5 **A schematic of the sample configuration during hard X-ray microtomography imaging.** Monochromatic X-rays illuminate the pouched electrochemical cell. The transmitted X-rays are converted to optical light by a scintillator. The optical light is then magnified with conventional optical microscope lenses and captured on a CCD screen. The sample is continuously rotating about a single axis as approximately 1000 radiograph images are taken between the angles of 0 – 180 °.

The primary mode of contrast between different materials in the sample comes from differences in the photoelectric absorption of the materials. The photoelectric absorption of a material is a function of the energy of the incident beam, the density of the material, and the atomic number (z) of the atoms that make up the material [60]. Generally, as the atomic number of the material increases, the photoelectric absorption increases. In our case, lithium metal ($z_{Li} = 3$) absorbs less incident X-rays than the polymer electrolyte ($z_C = 6$) resulting absorption contrast between the two phases. The X-ray absorption of a polymer electrolyte, lithium metal, and LiTFSI salt are shown as a function of X-ray energy in Figure 1.6 [61].

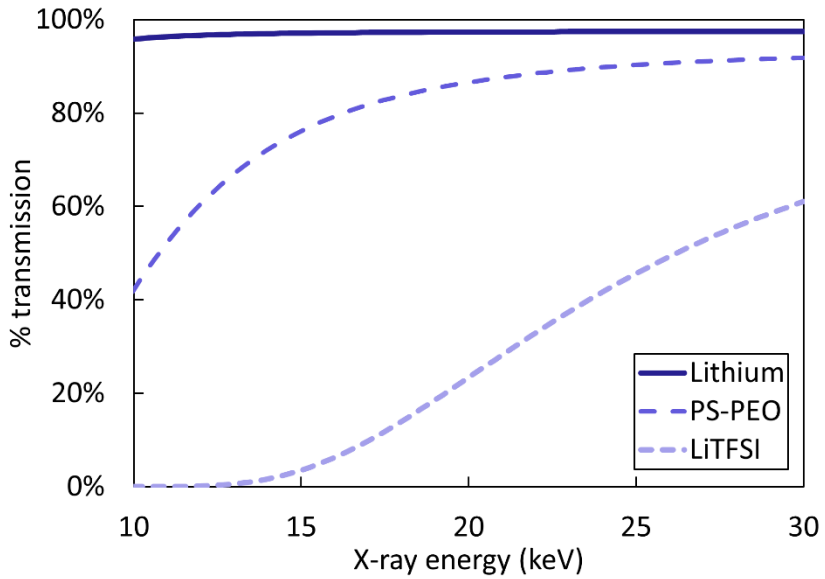

Figure 1.6 The percent of X-rays transmitted through 3175 μm (1/8 inch) of lithium, PS – PEO, and LiTFSI are shown as a function of X-ray energy. These % transmission values were calculated using the filter transmission tool on the Center for X-ray Optics website [http://henke.lbl.gov/optical_constants/filter2.html].

In addition to absorption contrast, phase contrast can also help delineate the border of two materials in the sample. When X-rays pass through a material, the phase of the X-ray shifts depending on the material. If two materials share a border, the phase of the light that leaves one material will differ from the phase of the light that leaves the neighboring material. If there is a non-negligible distance between the sample and the detector, the out-of-phase wave fronts will interfere with each other yielding Fresnel Phase contrast as shown in Figure 1.7 [62,63]. These two contrast mechanisms are both always present in X-ray microtomography images. However, the phase contrast effect can be exaggerated by increasing the sample to detector distance. Some researchers have taken advantage of this effect to exaggerate contrast between materials that have similar photoelectric absorption using a microtomography technique called holotomography [64].

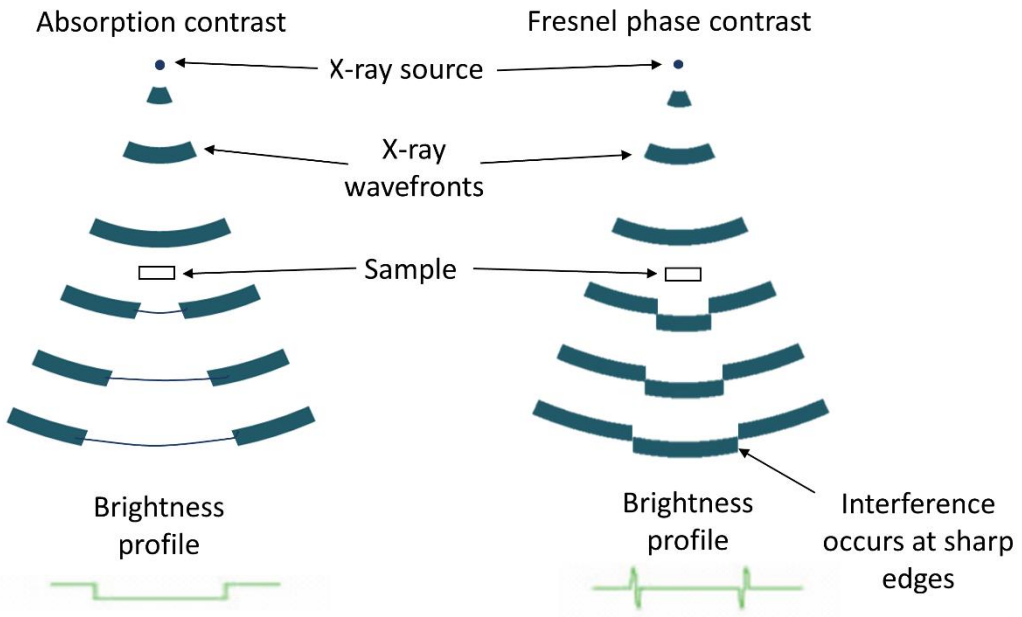

Figure 1.7 Contrast in hard X-ray microtomography images come from two sources. First, materials with different photoelectric absorption coefficients will absorb a different amount of the incident X-rays resulting in absorption contrast. Additionally, as light travels through different materials, the phase of the light is changed. The out-of-phase X-ray wavefronts will interfere resulting in Fresnel phase contrast at the interface of two different materials. The resulting brightness profile collected on the CCD screen is a combination of absorption contrast and phase contrast. Phase contrast can be lowered by reducing the sample to detector distance. This schematic was reproduced from [65].

Although X-ray imaging is largely non-destructive, the sample does interact with light, so it is important to consider the influence of beam damage in these experiments. Some groups have reported radiation damage to hydrated polymer electrolytes used in fuel cell applications imaged at the TOMCAT X-ray microtomography beamline at the Swiss Light Source. They observed obvious voltage drops in their galvanostatic charging curves when the sample was exposed to anything larger than 26 kGy (1 Gy = 1 J/kg) of radiation energy [66,67]. Other groups have reported significant reduction in fracture toughness of bone after irradiation with hard X-rays during microtomography experiments. X-rays can damage bone by radiolizing water molecules and releasing free radicals that induce cross-linking of collagen within the bone. When collagen cross links, it loses much of its elasticity, significantly reducing the fracture toughness of the bone. It is generally accepted that radiation doses larger than 70 kGy will damage bone [68].

At the beamline used for our experiment, the radiation dose at 20 keV is approximately 0.12 kGy/s. With an exposure time of 350 ms per image and 1025 images per scan, the sample experiences about 43 kGy of radiation per scan. Nonetheless, no measurable changes to our samples are observed during or after irradiation. The key difference between our samples and the hydrated polymer electrolytes used for fuel cell studies is the absence of water. Because our samples are completely dry, there is no potential for the radiolysis of water and subsequent free radical initiated degradation of the polymer. In fact, it is known that deep freezing or freeze drying bone samples before imaging can protect the sample from radiation damage caused by free radical

formation. We suspect that our samples show no sign of radiation damage, even after repeated scans, because the samples do not contain any materials that are easily radiolized, like water.

1.7 Outline of dissertation

In the enclosed work, X-ray microtomography is coupled with electron microscopy, rheological measurements, and conventional electrochemical testing methods to study the formation and growth of lithium metal globules through a solid block copolymer electrolyte membrane. Chapter 2 discusses a study examining the evolution of globule growth in cycled symmetric lithium – block copolymer electrolyte – lithium cells using X-ray microtomography. Chapter 3 provides a detailed description of the use of X-ray microtomography to study the failure of symmetric cells and batteries. Chapter 4 discusses the influence of the viscoelastic properties of the polymer electrolyte on the morphology of lithium globules and the resulting propensity for the cell to fail by short-circuit. Chapter 5 details a stop-motion X-ray microtomography experiment showing the formation and growth of lithium globules in electrochemically polarized symmetric cells. A discussion on the mechanism for globule and void formation in these systems is provided. Details on the factors influencing dendrite morphology are also discussed. Chapter 6 provides a quantitative analysis of the formation of lithium globules through a stiff electrolyte. The local deposition current density is measured and mapped in the vicinity of growing globules. The current density is observed to delocalize from the globule tip. The experimental data is coupled with finite element models to determine the influence of stresses at the lithium – electrolyte interface on the deposition current density of lithium ions.

Chapter 2 – Detection of Subsurface Structures Underneath Dendrites formed on Cycled Lithium Metal Electrodes[†]

ABSTRACT

Failure caused by dendrite growth in high-energy-density, rechargeable batteries with lithium metal anodes has prevented their widespread use in applications ranging from consumer electronics to electric vehicles. Efforts to solve the lithium dendrite problem have focused on preventing the growth of protrusions from the anode surface. Synchrotron hard X-ray microtomography experiments on symmetric lithium-polymer-lithium cells cycled at 90 °C show that during the early stage of dendrite development, the bulk of the dendritic structure lies within the electrode, underneath the polymer-electrode interface. Furthermore, we observed crystalline impurities at the base of the subsurface structures. The portion of the dendrite protruding into the electrolyte increases upon cycling until it spans the electrolyte thickness causing a short circuit. Contrary to conventional wisdom, it appears that preventing dendrite formation in polymer electrolytes depends on inhibiting the formation of subsurface structures in the lithium electrode.

2.1 Introduction

Reliable, rechargeable batteries with a high specific energy are vital for a wide variety of applications [69]. From many perspectives, the most attractive anode for a rechargeable battery is lithium metal because it is the lightest and most electropositive metal [70,71]. A major problem that emerges when batteries containing a lithium metal anode are cycled is the growth of dendrites that appear to protrude from the lithium metal surface [72,73]. The passage of current through these structures can result in ignition of the electrolyte and catastrophic failure [74,75]. Efforts to prevent dendrite growth have primarily focused on blocking these protrusions [49,76-78]. This paper demonstrates the presence of subsurface structures within the lithium electrode that lie underneath the dendrites. Furthermore, the formation of the subsurface structures dominates early stages of dendrite growth in polymer electrolyte cells at 90 °C, suggesting that the key to preventing dendrite formation is the elimination of filamentous cavities inside the electrode.

The electrodes in today's lithium ion batteries are porous, and about 30 vol% of the electrode is taken up by inactive phases[79]. With a lithium metal anode however, the simplicity of the reactions at the lithium electrode and facile transport of electrons within the metal eliminates the need for designing porous electrodes containing separate phases for transporting ions and electrons. Furthermore, many of the high-energy-density battery technologies being researched today, such as lithium-sulfur and lithium-air batteries, assume the presence of a lithium metal anode [11,80]. It is thus not surprising that researchers have used a variety of tools to study dendrite formation in lithium batteries. These include optical and electron microscopy [31,81-85], nuclear

[†] This chapter was reported in *Nat Mater* **13**, 69-73 (2014).

magnetic resonance [86], magnetic resonance imaging [87], etc. These techniques have detected "tree-like" or "moss-like" structures that emanate from the lithium surface and protrude into the electrolyte [88-90]. A key advance in this paper is the use of synchrotron hard X-ray microtomography that enables the imaging of structures residing on either side of the lithium metal electrode-electrolyte interface, illuminating the presence of subsurface structures in the lithium anode beneath dendritic protrusions.

2.2 Procedure

The cells used in these experiments are symmetric lithium-polymer-lithium cells assembled and pouched inside an argon filled glovebox. The polymer electrolyte was a polystyrene-*block*-poly(ethylene oxide) copolymer (SEO) mixed with lithium bis(trifluoromethanesulfonyl)imide (*LiTFSI*) salt. Details about the procedure used to prepare the electrolyte film are given in the Methods section of the supplementary material. Two 150 μm thick, 8 mm diameter lithium electrodes were punched out of lithium foil (FMC Lithium). One 9.5 mm piece of copolymer electrolyte was punched out of the prepared 30 μm thick film and sandwiched between the lithium electrodes. Nickel current collector tabs were placed on the electrodes and the whole cell was vacuum sealed in a polypropylene lined, aluminum pouch. The cells were cycled in an oven at 90 °C using a Bio-Logic VMP3 potentiostat at atmospheric pressure.

The cycling routine for all cells was as follows. Each cycle consisted of a 4 hour charge followed by a 45 minute rest and a 4 hour discharge. The cells were first cycled fifteen times at a low current density of 0.02 mA/cm^2. This was followed by cycling at a current density of 0.175 mA/cm^2 until the experiment was stopped for cell imaging or when the cell shorted. A typical cycling routine is shown in Figure 2.S1 where the time dependence of the measured cell voltage and the applied current is shown.

After cycling, the cells were taken back into the glovebox where a 3 mm punch was used to remove a small portion of the cell for imaging. Additionally, the nickel current collectors were removed. The smaller cell size and elimination of the nickel current collectors improved the quality of the X-ray microtomography images. The punched out portion of the cell was vacuum sealed in a pouch and transferred from the glovebox to the microtomography beamline.

2.3 Results and Discussion

The cells were imaged using hard X-ray microtomography at the Advanced Light Source at Lawrence Berkeley National Laboratory [91]. Slices through typical tomograms obtained from our cells are shown in Figure 2.1. Figure 2.1a shows an image obtained from an uncycled cell. The image is dominated by three phases, two lithium electrodes that surround a 30 μm thick electrolyte. Since both electrolyte and the electrodes are composed of light elements, the tomography data mainly reflect the interface between these phases. The electrode-electrolyte interfaces of uncycled cells are devoid of any noticeable features (Figure 2.1a). We examined four uncycled cells with a total electrode-electrolyte interface of 12 mm^2 and found no dendritic structures. Figure 2.1b shows an image of a cell after fifteen conditioning cycles at 0.02 mA/cm^2 (C = 9 C/cm^2). The image shows the presence of heterogeneities in the lower lithium electrode. The entire cell at this stage had six identifiable heterogeneous structures located in both electrodes. Figure 2.1c shows an image of an unshorted cell after the conditioning cycles and an additional 15 cycles at the full current density of 0.175 mA/cm^2 (C = 84 C/cm^2). Numerous dendritic structures were seen in the cell. The bottom electrode in Figure 2.1c shows one example. No electrolyte-spanning structures

were seen in this cell. Figure 2.1d shows an image of a shorted cell after 63 full cycles at 0.175 mA/cm^2 (C = 296 C/cm^2). Shorted cells showed dendritic structures that were bigger than those shown in Figure 2.1c. They also showed electrolyte-spanning structures and an example is shown in Figure 2.1d. Videos showing the full-tomogram of the cells shown in Figure 2.1 are available in the supplementary information. In a given cell, dendrite growth was observed on both electrodes with roughly equivalent prevalence. For simplicity, the images in Figure 2.1 are oriented so that the dendritic structures are in the bottom electrode.

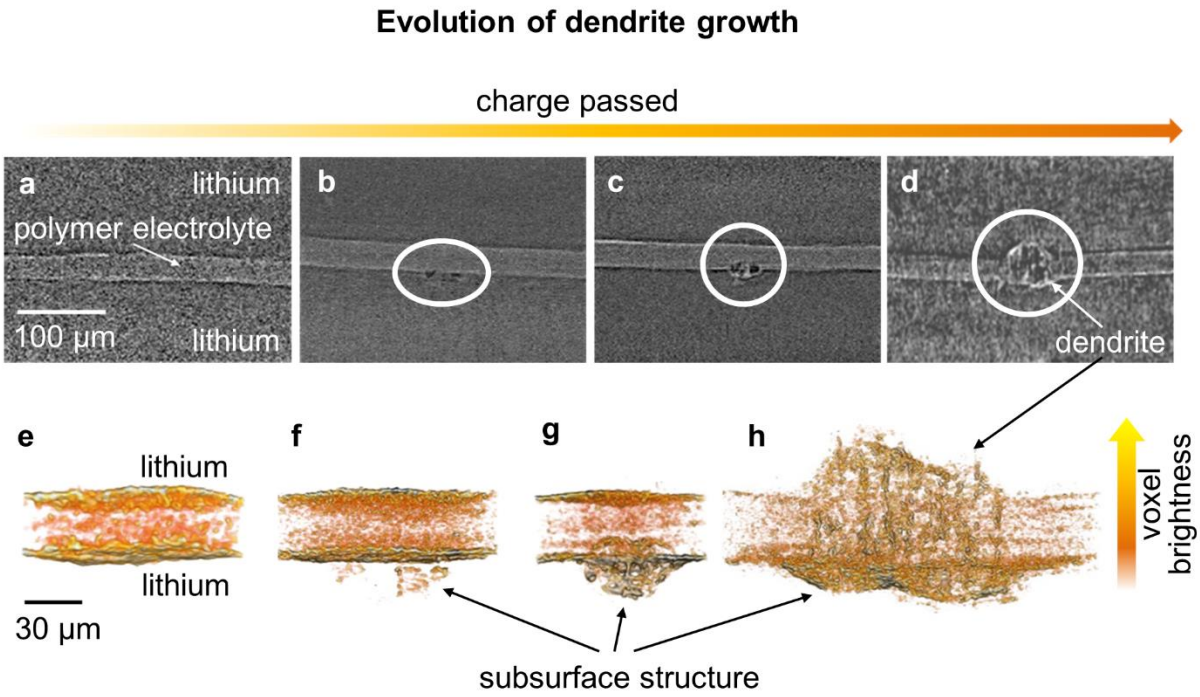

Figure 2.1 **Evolution of dendrite growth a,b,c,d** X-ray tomography slices showing the cross-sections of symmetric lithium cells cycled to various stages. The thin, bright horizontal strip through the center of the images is the polystyrene-*block*-poly(ethylene oxide) copolymer electrolyte sandwiched between two lithium metal electrodes. The amount of charge passed, C, for each cell is: (**a**) 0 C/cm^2 (**b**) 9 C/cm^2 (**c**) 84 C/cm^2 (**d**) Shorted Cell: 296 C/cm^2. Dendritic structures are evident in B, C, and D. **e,f,g,h** Magnified, three-dimensional reconstructed volumes of cells shown in the top panel. (**e**) An uncycled cell with no dendritic structures, C = 0 C/cm^2 (**f**) Heterogeneous structures begin to form in the bottom electrode in early stages of cycling, C = 9 C/cm^2 (**g**) Dendritic structures in both electrolyte and electrode phases are seen at the intermediate stage of cycling, C = 84 C/cm^2 (**h**) Dendritic structures that span the thickness of the electrolyte are seen in the shorted cell, C = 296 C/cm^2.

Note: As discussed in Chapter 1, the term "dendrite" implies branching. The structures shown here are unbranched and would be more aptly described as multi-globular structures. However, given the prevalence of the use of "lithium dendrite" to describe the structures that cause batteries to fail by short-circuit in the electrochemical literature, these globular structures are referred to as dendrites in this chapter.

The bottom panel of Figure 2.1 shows three-dimensional (3D) reconstructed volumes of selected regions around the slices shown in the top panel. Each reconstructed volume may be viewed as a three-dimensional array of brightness values. Voxels with brightness below a certain threshold were rendered transparent and the rest were placed on a color-scale with yellow indicating the brightest voxels. The voxel brightness is proportional to the local electron density, while the electrolyte-electrode interface is highlighted by Fresnel phase contrast[92,93]. In addition, the data was subjected to an edge-enhancement protocol wherein the change in voxel intensity with position is recorded and areas where these changes are steep are highlighted. All of the analysis described above was conducted using the commercial image processing package, Avizo.

The 3D nature of the dendritic structures formed in our cells is clearly evident in the bottom panel of Figure 2.1. In Figure 2.1e, we mainly see two flat sheets representing the uncycled electrode-electrolyte interfaces. X-ray absorption is higher for the SEO electrolyte than the lithium electrode resulting in brighter voxels in the electrolyte phase. The presence of dark orange features between the sheets in Figure 2.1e and the absence of features above and below the sheets is due to this effect. Since the resolution of this imaging technique is on the order of a micrometer, some speckling is visible in the images due to noise. The lightly cycled cell shown in Figure 2.1f (C = 9 C/cm^2) exhibits orange features below the bottom electrode-electrolyte interface. Figure 1g shows the reconstructed volume of the dendritic structure seen in Figure 2.1c (C = 84 C/cm^2). The dendritic structure has two parts, one that lies within the electrolyte and the other that lies within the electrode. Since our imaging technique highlights interfaces, it is evident that both parts of the dendrites are filled with ramified lithium-polymer interfaces.

Since one expects dendrites to be filamentous structures, the presence of lithium-polymer interfaces on the electrolyte side is not surprising. The presence of filamentous structures on the electrode side is the surprising new finding of this study. It is clear that most of the dendrite in Figure 2.1g resides within the electrode, not within the electrolyte. Figure 2.1h shows a reconstructed volume of the electrolyte-spanning dendritic structure pictured in Figure 2.1d. Here we see lithium polymer interfaces that run across the electrolyte and the presence of filamentous structures in both top and bottom electrodes.

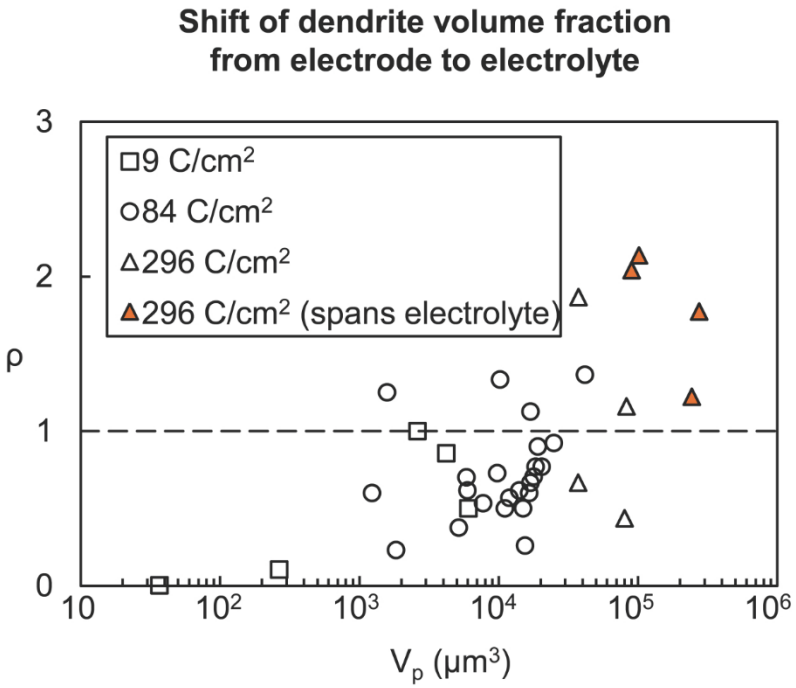

Figure 2.2 **Shift of dendrite volume fraction from electrode to electrolyte** Properties of dendritic structures obtained from three cells with C = 9, 84, and 296 C/cm^2. The ratio of the volume of the dendritic structure in the polymer electrolyte to the volume of the structure in the electrode (ρ) is graphed against the volume of the dendritic structure in the polymer electrolyte (V_p). In the initial stages of cycling (C = 9 C/cm^2), most of the data points lie below the ρ = 1 line indicating that the majority of the dendritic structures in these cases lie within the electrode. As the dendrites develop and V_p increases, the portion of the structure extending into the electrolyte grows until the dendritic structure spans the electrolyte resulting in cell failure.

For the case of the non-electrolyte spanning dendritic structures, (e.g. Figure 2.1c) we approximate the volume of the structure that lies in the electrolyte and the part that lies in the electrode as two half-ellipsoids. The method used to quantify the volume of the dendritic structures that lie in the electrode or in the electrolyte is explained in detail in the Methods section of the supplementary material. We define ρ to be the ratio of the volume of the dendritic structure in the electrolyte to the volume in the electrode. Figure 2.2 shows a plot of ρ versus V_p, the volume of the dendritic structure in the polymer electrolyte, for three cells cycled to difference values of C. Data obtained at different stages of cycling are identified by different symbols. The values of ρ of all of the dendritic structures obtained during the early stage of cycling (C = 9 C/cm^2) are equal to or less than unity. The average value of ρ for this data set is 0.4 indicating that the dendritic structures lie mostly within the electrode. The values of ρ obtained at the intermediate stage of cycling (C = 84 C/cm^2) scatter between 0.2 and 1.4 but 19 out of the 23 dendritic structures observed have values of ρ less than unity. The average value of ρ for this data set is 0.7 indicating that even at this stage, the dendritic structures lie mostly within the electrode. Half of the dendritic structures obtained in the shorted cell spanned the electrolyte (Figure 2.1d). We approximate these structures as elliptic cylinders that run through the electrolyte capped by two half-ellipsoids. The methodology to determine ρ for these structures is analogous to that described in the supplementary

information. Most of the values of ρ obtained in the shorted cell are greater than one (average value of ρ is 1.4) indicating that in this stage the dendritic structures lie mostly in the electrolyte.

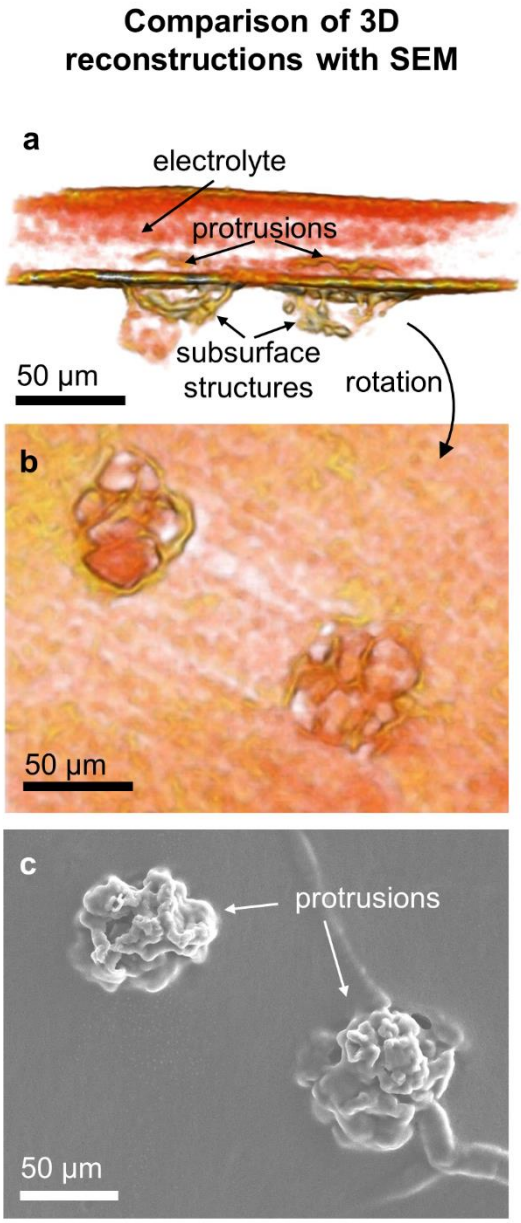

Figure 2.3 **Comparison of 3D reconstructions with SEM a** Three-dimensional reconstructed volume of a cell with $C = 84$ C/cm^2 containing two, closely spaced dendrites. **b** The reconstructed volume was rotated such that the viewer is within the electrolyte looking at the dendrites. **c** Scanning electron micrograph (SEM) of the bottom electrode of the same cell, after dissolving away the electrolyte, showing the dendritic structures. The SEM images contain no direct evidence for the presence of subsurface structures under the dendritic protrusions.

Figure 2.3a and 2.3b show a reconstructed 3D volume of a portion of a cell that contained two dendritic structures near each other obtained during the intermediate stage of cycling. (This is a different portion of the same cell shown in Figures 2.1c and 2.1g.) After X-ray imaging, the cell shown in Figure 2.3a and 2.3b was brought back into an Argon filled glovebox where it was submerged in a 1:9 by volume mixture of tetrahydrofuran and benzene for two weeks. The polymer electrolyte dissolved away enabling the imaging of the lithium electrodes using scanning electron microscopy (SEM). The presence of two dendritic structures near each other was rare and thus it was relatively easy to identify the portion of the electrode from which the reconstructed 3D volume was obtained in the scanning electron microscope. The SEM image thus obtained is shown in Figure 2.3c. The dendrites seen in this image are similar to structures reported in the literature [70,85]. In particular there is only a hint of the existence of a subsurface structure underneath these dendritic structures. Figure 2.3a provides a more complete description of these dendritic structures. The values of ρ for these dendritic structures are 0.7 and 0.6 indicating that large portions of the dendritic structures imaged in Figure 2.3c lie beneath the electrode-electrolyte interface and are not visible in the SEM image.

It is important to determine if the characteristics of dendritic structures reported above apply only to nanostructured electrolytes. This was addressed by conducting experiments on a symmetric lithium-lithium cell with a mixture of PEO homopolymer and LiTFSI as the electrolyte. The average electrolyte thickness in this cell was 200 μm which is considerably larger than that of the SEO electrolytes described above. We were unable to create thin PEO based electrolytes in our lab. The ability to create thin films is a strong function of the mechanical properties of the material, and the modulus of SEO electrolytes is a factor of about 100 larger than that of PEO [83]. We used a slightly different cycling protocol for this cell from that used for SEO cells due to the electrolyte thickness difference as described in the Methods section of the supplementary material. The dendritic structure observed by X-ray microtomography after the cell shorted is shown in Figure 2.S2. Subsurface structures were clearly observed in this case. While the detailed shape and location of the dendritic structures depend on a variety of experimental parameters such as thickness, modulus, and morphology of the electrolyte, current density, and total amount of charge passed per cycle, subsurface structures were observed in all of the experiments conducted thus far. Figure 2.S3 shows the effect of total amount of charge passed per cycle on dendrite morphology.

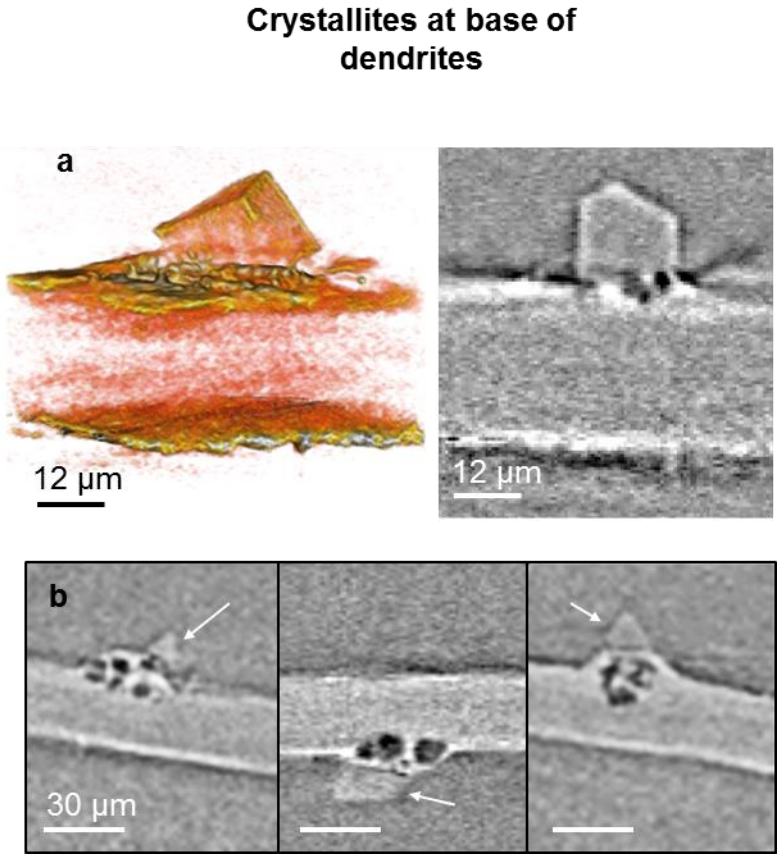

Figure 2.4 **Crystallites at base of dendrites a** A high magnification image of a crystallite sitting at the SEO electrolyte, lithium metal electrode interface. This cell was cycled to C = 18 C/cm^2. **b** X-ray microtomography images of dendrites with crystallites at their base. The first and last images were taken from different locations within the cell cycled to C = 84 C/cm^2. The center image was taken from a cell cycled to C = 16 C/cm^2.

The mechanism by which the dendritic structures shown in Figure 2.1 nucleate and grow is an important question that we cannot definitively answer at this stage. In the future we will address this issue by conducting *in situ* X-ray microtomography experiments during cycling. Our hypothesis at this juncture is that contaminants in the lithium electrode are responsible for the nucleation of subsurface dendritic structures. The manufacturer of the lithium foil used in this study (FMC Lithium) lists the concentrations of a number of elements other than lithium. The most abundant element listed, at a concentration of 300 wppm, for example, is nitrogen which is probably in the form of Li_3N[4,94]. The deposition of lithium on an electrode containing such a contaminant would result in slower deposition in the region near the insulating Li_3N crystallite relative to that in surrounding regions. Figure 2.4a shows a high-resolution X-ray tomography image of a symmetric lithium-SEO-lithium cell with a crystalline contaminant at the electrode-electrolyte interface. Under low resolution, these crystallites appear as bright specks in the lithium electrode and are clearly visible in Supplementary Video 3. Every dendritic structure that we have observed appears to have a bright speck at the base. Examples of X-ray tomograms emphasizing the bright specks at the base of dendrites are shown in Figure 2.4b. Our results suggest that eliminating insulative contaminants from the lithium electrodes is the key to solving the lithium

dendrite problem in polymer electrolytes. More work is needed to establish a general framework for understanding the relationship between dendrite formation in lithium electrodes and properties of the electrolyte (e.g. viscosity, modulus, salt concentration, etc.). Previous work of Rosso et al. [95,96] and Monroe et al. [49,77] provides a starting point for developing such a framework, including the effect of lateral heterogeneity in the electrode on dendrite growth [97].

2.4 Conclusion

The growth of dendritic structures from lithium metal anodes is a major problem precluding the widespread use of high-energy-density, rechargeable batteries with lithium metal anodes. Synchrotron hard X-ray microtomography was used to study the morphology of cycled lithium-polymer-lithium cells at 90 °C. The data show conclusively that under these conditions, buried under every dendritic structure emanating from the electrode-electrolyte interface were subsurface structures located within the lithium electrode. In the early stages of dendrite formation, the volume occupied by the subsurface structure is significantly larger than that occupied by the dendritic structure protruding out from the electrode surface. Current approaches for preventing dendrite growth on lithium metal electrodes are based primarily on suppressing the protrusions. This work indicates the need for a fresh start; preventing the growth of lithium dendrites may involve suppressing the nucleation of subsurface structures in the lithium electrode itself, long before the dendrites extend into the electrolyte.

2.5 Methods

2.5.1 Sample preparation

The samples discussed in this study were prepared using the following technique. A polystyrene-*block*-poly(ethylene oxide) copolymer electrolyte (SEO) was prepared by anionic polymerization, as described in previous work[23,98,99]. The molecular weight of the polystyrene (PS) and polyethylene oxide (PEO) blocks were 240 kg/mol and 260 kg/mol, respectively, with a PEO volume fraction of 0.50 and an overall polydispersity index of 1.26. The copolymer was dissolved in N-methyl-pyrrolidone (*NMP*) and mixed with lithium bis(trifluoromethanesulfonyl)imide (*LiTFSI*) salt such that the molar ratio of lithium ions to ethylene oxide groups was 0.085. This salt concentration was found to maximize conductivity in SEO electrolytes[100]. An electrolyte film was then cast with a nickel foil coated solvent caster forming a 30 μm thick sheet after the NMP evaporated away.

In Supplementary Figure 2.1a, we show typical results obtained during the first 30 cycles. In Supplementary Figure 2.1b, we show typical data from a cell as it shorted. It is clear that the total amount of charge passed through the cell prior to shorting, C, is easily detected. For the cell in Supplementary Figure 2.1b, $C = 593$ C/cm^2.

2.5.2 X-ray microtomography

The cells were imaged using monochromatic hard X-rays with energies chosen in the 22 – 25 keV range on beamline 8.3.2 at the Advanced Light Source at Lawrence Berkeley National Laboratory. X-rays generated by the synchrotron illuminated the entire sample, and the X-ray shadow cast by the sample was converted into visible light using a scintillator. An optical microscope magnified this image and converted it into a digital image file. The sample was then rotated by a fraction of a degree and repeatedly imaged until 1025 images were collected from the sample as it was rotated through 180°. After a series of data processing steps, these shadow images

were converted to cross-sectional slices that were then stacked together to render a three-dimensional reconstruction of the cell.

2.5.3 Methods for calculating dendrite volume

For the case of the non-electrolyte spanning dendritic structures (e.g. Figure 2.1c) we approximate that each structure is composed of two half-ellipsoids. The half-ellipsoid in the lithium electrode has characteristic lengths a, b_l, and c. The half-ellipsoid in the polymer electrolyte has characteristic lengths a, b_p, and c. We obtained these lengths by examining our images in a Cartesian coordinate system defined in Supplementary Figure 2.4. Also shown in Supplementary Figure 2.4 is a magnified view of a particular slice through the dendritic structure shown in Figure 2.1c. The electrode-electrolyte interface is approximately parallel to the xz plane. We examined xy slices at various z locations and found the slice that contains the largest number of dendritic voxels. We refer to this location as $z = z_D$. We assume that the length of the structure along the x-direction is $2a$. The half-minor-axes of the two half ellipsoids are depicted by line segments $\overline{AD}$ and $\overline{DB}$ in Supplementary Figure 2.4. The plane of the interface between the electrode and the electrolyte within the dendritic structure is determined by extrapolating the line that defines the interface away from the structure in the $z = z_D$ plane as shown in Figure 2.S4. This plane intersects $\overline{AB}$ at point D.

$$b_p = m(\overline{AD})$$

$$b_l = m(\overline{DB})$$

where subscripts p and l stand for polymer electrolyte and lithium electrode. We then examine xy slices in the $z < z_D$ regime until the structure disappears at $z = z_{Df}$. Similarly, we examine xy slices in the $z > z_D$ regime until the structure disappears at $z = z_{Db}$. We take $2c = |z_{Df} - z_{Db}|$. The volume of the dendritic structure in the phase of interest is given by, $V_i = \frac{2}{3}\pi a b_i c$ where $i = p$ or l. We define ρ to be the ratio of the volume of the dendritic structure in the electrolyte to the volume in the electrode ($\rho = V_p/V_l$).

A symmetric lithium – PEO – lithium cell was prepared by pressing homopolymer polyethylene oxide, molecular weight 240 kg/mol, into a 3/16 inch diameter spacer cut from pouch material. Two pieces of lithium foil were placed on either side of the PEO film. The cell was vacuum sealed then cycled at 90°C on a Bio-Logic VMP3 at atmospheric pressure. The cycling routine was as follows. The cells were first cycled fifteen times at a low current density of 0.06 mA/cm^2. This was followed by cycling at a current density of 0.175 mA/cm^2. After 23 cycles at 0.175 mA/cm^2, the current density was increased to 0.34 mA/cm^2 for two cycles at which point the cell shorted. X-ray tomographs of the shorted cell were compared to an uncycled lithium-PEO-lithium cell prepared in the same manner. No structures like those seen in Figure 2.S2 were visible in the uncycled cell.

2.6 Acknowledgments

Primary funding for the work was provided by the Electron Microscopy of Soft Matter Program from the Office of Science, Office of Basic Energy Sciences, Materials Sciences and Engineering Division of the U.S. Department of Energy under Contract No. DE-AC02-

05CH11231. The battery assembly portion of the project was supported by the BATT program from the Vehicle Technologies program, through the Office of Energy Efficiency and Renewable Energy under U.S. DOE Contract DE-AC02-05CH11231. Hard X-ray microtomography experiments were performed at the Advanced Light Source which is supported by the Director, Office of Science, Office of Basic Energy Sciences, of the U.S. Department of Energy under Contract No. DE-AC02-05CH11231. Katherine J. Harry was supported by a National Science Foundation Graduate Research Fellowship.

2.7 Supplementary Information

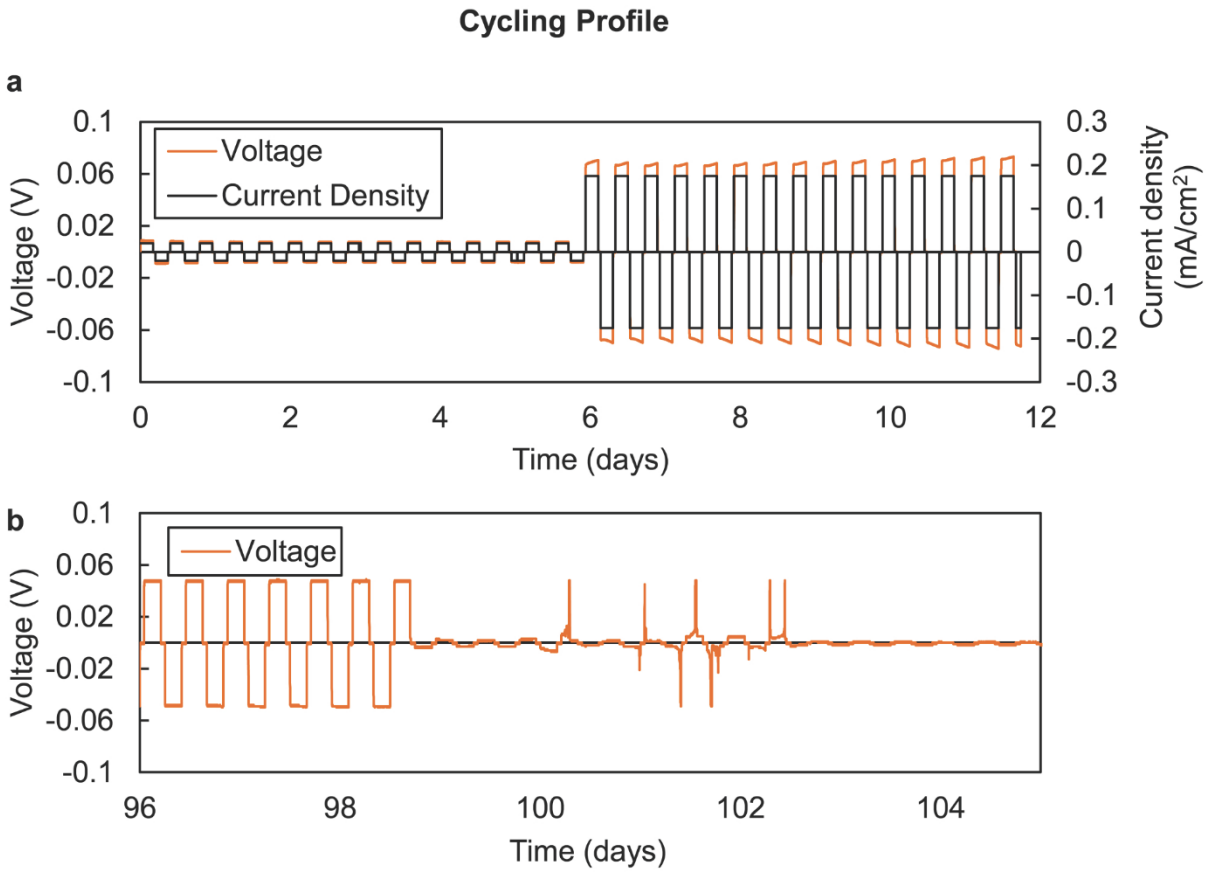

Figure 2.S1 **Cycling Profile a** A typical cycling profile of cells. The first 15 cycles use a lower current density to condition the cells. After these conditioning cycles, the cell was cycled at a current density of 0.175 mA/cm^2 until it shorted or was stopped for imaging. **b** The cycling profile of a cell as it shorts. After 98 days, the cell can no longer maintain a voltage difference between the electrodes indicating that the cell has short-circuited. Applied current density (± 0.175 mA/cm^2) is not shown in lower panel for clarity.

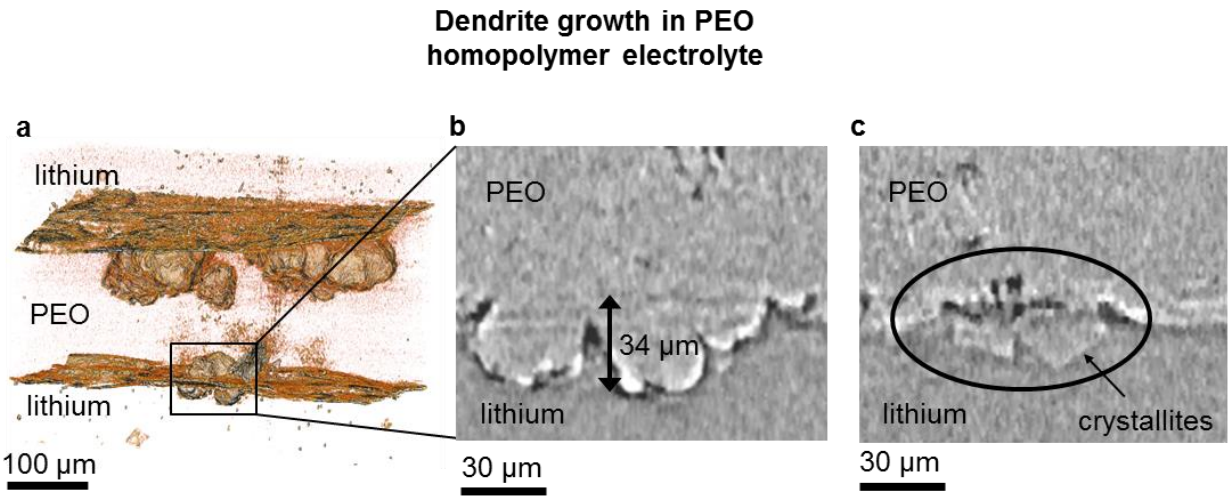

Figure 2.S2 **Dendrite growth in PEO homopolymer electrolyte a** A 3D reconstruction of a cycled and shorted symmetric lithium-lithium cell imaged by X-ray microtomography. **b** A cross-section slice through the dendritic structure shows subsurface structures of comparable depth to those seen in SEO electrolytes. **c** Crystallites also appear at the base of the dendritic structure seen in the shorted PEO cell.

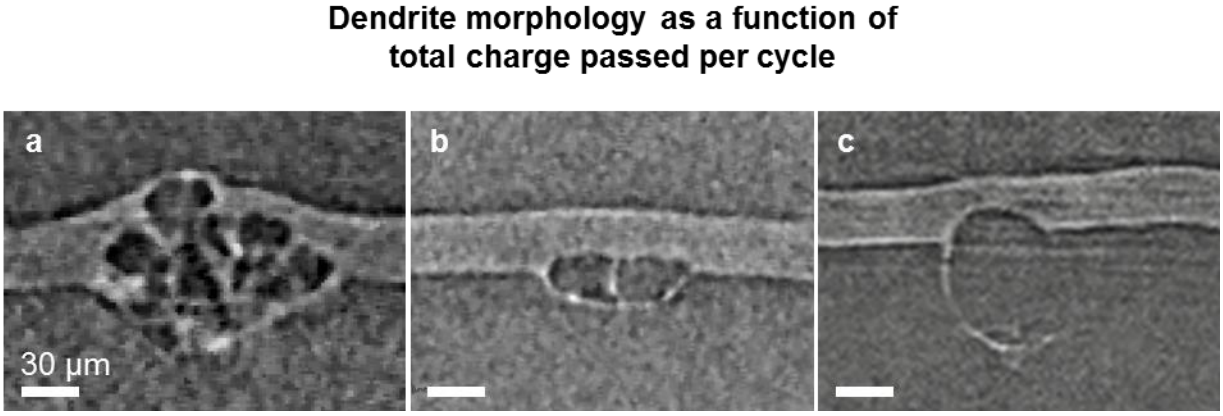

Figure 2.S3 **Dendrite morphology as a function of total charge passed per cycle** Dendrites of different morphologies formed on shorted lithium – SEO – lithium symmetric cells. All cells were cycled at a constant current density of 0.175 mA/cm^2. The total charge passed per cycle was varied by changing the time used for charge and discharge. **a** This cell was cycled with a charge/discharge time, τ, of 4 hours and this corresponds to stripping and plating a 3.4 µm thick layer of lithium (L = 3.4 µm) . Cell imaged at C = 83 C/cm^2. **b** τ = 16, L = 13.6 µm. The cell was imaged at C = 101 C/cm^2. **c** After preliminary cycling, charge was passed in only one direction for 48 hours from top to bottom (τ = 48, L = 40.8 µm) . The cell was imaged at C = 115 C/cm^2. When the amount of charge passed per cycle increases, the size of the cell-like structures within the dendrite also increases, but subsurface structures are seen in all cases.

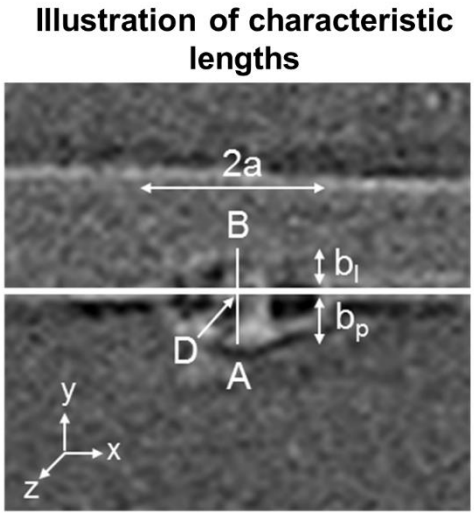

Figure 2.S4 **Illustration of characteristic lengths** The variables used to quantify the size of the dendritic structures are illustrated by showing a tomographic slice through the $z = z_D$ plane. The characteristic lengths, a, b_l, and b_p, of the two half-ellipsoids approximating the dendritic structures are shown. Line segment $\overline{ADB}$ and the coordinate system used in the analysis are also shown.

Chapter 3 – Failure analysis of batteries using synchrotron-based hard X-ray microtomography

ABSTRACT

Imaging morphological changes that occur during the lifetime of rechargeable batteries is necessary to understand how these devices fail. Since the advent of lithium-ion batteries, researchers have known that the lithium metal anode has the highest theoretical energy density of any anode material. However, rechargeable batteries containing a lithium metal anode are not widely used in consumer products because the growth of lithium dendrites from the anode upon charging of the battery causes premature cell failure by short circuit. Lithium dendrites can also form in commercial lithium-ion batteries with graphite anodes if they are improperly charged. We demonstrate that lithium dendrite growth can be studied using synchrotron-based hard X-ray microtomography. This non-destructive imaging technique allows researchers to study the growth of lithium dendrites, in addition to other morphological changes inside batteries, and subsequently develop methods to extend battery life.

3.1 Introduction

Researchers are actively investigating battery chemistries with theoretical energy densities over an order of magnitude larger than traditional lithium-ion batteries [5,11]. These high-energy-density batteries will make electric vehicles more competitive with their gasoline-powered counterparts [101]. However, these new chemistries have several failure modes that preclude their use in commercial technologies. For example, these battery chemistries require a lithium metal anode to achieve large enhancements in energy density; unfortunately, lithium metal is prone to dendrite growth as lithium ions are reduced at the anode surface during charging [15,56,57,72,102,103]. Additionally, breakage of active particles in the cathode and poor adhesion within the battery can cause cell failure [104].

Many modes of battery failure occur on the micrometer scale. However, most battery materials are air sensitive making sample preparation for analysis by electron microscopy and traditional optical microscopy difficult. Synchrotron hard X-ray microtomography allows one to visualize the interior of a battery without disassembly [105-108]. Furthermore, the technique produces a three-dimensional (3D) reconstruction of the assembled cell making it easy to find locations of failure [109]. Finding robust techniques that enable researchers to develop the scientific understanding required to accurately predict the lifetime of a battery is critical for the design of next generation battery technologies. The procedure discussed herein will specifically demonstrate how one can prepare and image model batteries to study the growth of lithium metal dendrites through solid polymer electrolyte membranes.

[†] This chapter was reported in *JoVE*, e53021 - e53021 (2015).

Computed tomography (CT) scanning is not a new technique and has been used frequently for failure analysis in industry. Synchrotron-based X-ray microtomography is advantageous because the high brightness and flux of the source allow collection of images with high resolution and good signal to noise in a much shorter amount of time [110]. Additionally, one can take advantage of the X-ray energy resolution to image at energies around a chemical species' absorption edge, causing the components containing that chemical species to be identified [111]. It was found that the synchrotron source provides sufficient flux to achieve good contrast between lithium metal and solid polymer electrolyte membranes enabling one to image lithium metal dendrites [109].

The study discussed herein uses a high modulus, block copolymer electrolyte membrane [23]. These high modulus membranes suppress lithium dendrite growth, lengthening the lifetime of batteries [83,112]. However, dendrites still eventually puncture the membrane causing the battery to fail by short-circuit. It is important to understand the nature of dendrite formation and growth in these high modulus electrolyte membranes in order to design strategies to prevent their growth.

3.2 Protocol

3.2.1 Electrolyte preparation

a. Synthesize a 240 kg/mol – 260 kg/mol poly(styrene) - *block* - poly(ethylene oxide) copolymer (SEO) using anionic polymerization.

b. Peform all additional sample preparation in an Argon glovebox where the water and oxygen levels are controlled and remain <5 ppm.

c. Dissolve 0.3 g of polymer in anhydrous N-methyl-2-pyrrolidone (NMP) with dry lithium bis(trifluoromethane)sulfonimide (LiTFSI) salt. Use an LiTFSI salt to SEO mass ratio of 0.275 and an NMP to SEO mass ratio of 13.13. Note: This quantity of polymer will yield a membrane large enough to make approximately 20 samples.

d. Cast all of the polymer and salt mixture prepared in the steps above onto an approximately 15 cm by 15 cm square piece of nickel foil using a doctor blade. Dry the resulting film at 60 °C overnight.

e. After drying, peel the film from the Nickel foil and allow to dry further under vacuum at 90 °C.

f. Wrap the resulting freestanding film in Nickel foil and store inside an air-tight box in the glovebox for later use.

3.2.2 Lithium – lithium symmetric cell preparation

a. Use a 7/16 inch diameter, round metal punch to cut out two lithium metal electrodes from a roll of 99.9% pure, battery-grade lithium metal foil.

b. Use a 1/2 inch diameter metal punch to cut out a piece of polymer electrolyte film.

c. Note: The lithium metal is softer and easier to punch than the polymer electrolyte.

d. Sandwich the polymer electrolyte film between the two lithium metal electrodes and press the nickel tabs onto the electrodes.

e. Vacuum seal the sample in an air-tight pouch made of polypropylene and nylon lined aluminum.

f. Note: One of the lithium electrodes is easily swapped with a cathode if one wants to study a full battery.

3.2.3 Symmetric cell cycling

a. Place the vacuum-sealed sample into an oven held at 90 °C and cycle using electrochemical cycling equipment. Heat the sample during cycling to achieve reasonable ionic conductivity through the electrolyte membrane. For safety, ensure that the sample does not approach the lithium metal melting point of 180 °C.

b. Pass a current density of 0.175 mA/cm^2 through the sample for four hours and follow with a 45 minute rest. Next, pass a current density of -0.175 mA/cm^2 through the sample for four hours and follow with a 45 minute rest. Repeat this cycling routine as many times as desired.

c. Observe the voltage response for this current density passed through a 30 μm thick SEO electrolyte and compare with that shown in Figure 3.1. Stop the cycling routine when the cell voltage response drops to 0.00V, because the battery has failed by short-circuit indicating the growth of lithium dendrites.

3.2.4 Synchrotron hard X-ray microtomography imaging

a. After the symmetric cell is cycled, bring it back into the glove box and remove it from its pouch.

b. Use a 1/8 inch metal punch to cut out the center portion of the cell. Vacuum seal the center portion of the cell in pouch material and remove from the glovebox for transport to the synchrotron facility. Note: By imaging a sample with a reduced diameter, the amount of material outside of the field of view of the X-ray detector is reduced. This improves the overall image quality by reducing noise caused by this extra material. Furthermore, removal of the highly X-ray absorptive Nickel current collectors is necessary, for this particular pouch design, to obtain clear X-ray images.

c. Once at the beamline, use polyimide tape to affix the sample to the sample stage. If desired, tape a small metal marker on top of the sample to aid with alignment. Place the metal marker roughly in the center of the sample to mark the location around which the sample will rotate once aligned.

d. Use 20 keV X-rays to image the sample with an exposure time optimized for the system. Optimize the exposure time by balancing the scan time and the number of counts per image. Estimate the total scan time by multiplying the exposure time by the number of images collected. Note: In our experiment, an exposure time of 300 ms was used, resulting in a scan time of 5 to 10 minutes.

e. Measure the pixel size associated with the optical lenses at the beginning of every beamtime shift. Note: For the 4x lens used to take the image shown in Figure 3.2, the pixel size was 1.61 μm / pixel. Higher magnification lenses (10x and 20x) are also available for use.

f. Position and align the sample on a rotation stage with respect to the detection system so that it remains in the detector's field of view as it rotates through 180°.

g. Position the sample as close to the detector as is possible while ensuring that the sample does not hit the detector at any rotation angle. Note: As the sample to detector distance increases, the Fresnel phase contrast will become more pronounced in the reconstructed images. This can obscure features and result in poorer resolution. For pouch cells, the sample to detector distance is typically on the order of 3 cm away from the detector.

h. Once aligned, perform a scan consisting of 1025 images collected over sample rotations between 0 and 180°. Collect "Bright field" (also known as "flat field" or "background") images by moving the sample out of the field of view. Additionally, collect "dark field" images by taking images while the beam is off. Use these to normalize the sample images for inhomogeneous illumination, scintillator response, and CCD camera response.

3.2.5 Image Reconstruction

a. Tomographically reconstruct the set of 1025 radiographs into a stack of images where each image represents a slice in the volume using the following procedure.

b. First, normalize the images by subtracting the "dark field" images from both the radiograph images and the "bright field" images. Divide the resulting radiograph images divided by the resulting "bright field" images.

c. Next, perform tomographic reconstruction, the process by which the series of projection angles is transformed into a 3D image, on the normalized radiograph images

d. The reconstruction software outputs a series of images, each representing a horizontal slice through the sample.

e. When stacked, this set of reconstructed images form a three-dimensional X-ray absorption map of the sample.

f. Visualize the individual slices or the sample in three-dimensions to see what the sample looks like on the inside.

3.2.6 Data visualization and processing

a. Use one of a multitude of commercial and open source image processing software packages available for data visualization and analysis [113,114].

b. Upon opening the stack of reconstructed images with the desired software, create orthoslices to show the xy, xz, and yz perspectives of the reconstructed data.

c. Pan through these images and search for features of interest, like the lithium dendrite shown in Figure 3.2.

d. Next, use segmentation (digital labeling) and 3D rendering tools to render the feature of interest in three-dimensions.

e. To digitally segment the image, create a label field and use thresholding tools to select regions of the sample corresponding to a material.

f. To recreate an image like that shown in Figure 3.2b, label the dark pixels lithium and the bright pixels electrolyte. Label the lithium contained in the dendrite separately from the top and bottom lithium electrodes. Render the dendritic lithium in orange and the polymer electrolyte in blue. Render the top and bottom lithium metal electrodes in gray and adjust the transparency value to reveal the orange dendritic lithium. Rotate this three-dimensional reconstruction to view the structure from many perspectives.

3.3 Representative Results

When the symmetric lithium-lithium cells described above are cycled at 90 °C, the voltage response looks like that shown in Figure 3.1. Eventually, lithium dendrites will grow through the electrolyte and cause the cell to fail by short circuit. When this happens, the voltage response to the applied current will drop down to 0.00 V. Dendrites, like the one shown in Figure 3.2 appear in samples that have failed by short circuit. Non-electrolyte spanning dendrites are also found in the samples. Using this method, one can study the evolution of dendrite growth as a function of the cell's stage of life by imaging a series of samples cycled to various stages of life as discussed in reference 15. The dendrite morphology and size can be easily measured from the three-dimensional reconstructed images. Additionally, this technique allows the user to see structures that lie inside of the lithium metal electrode. These features are hidden when one uses other imaging techniques, like scanning electron microscopy or traditional optical microscopy.

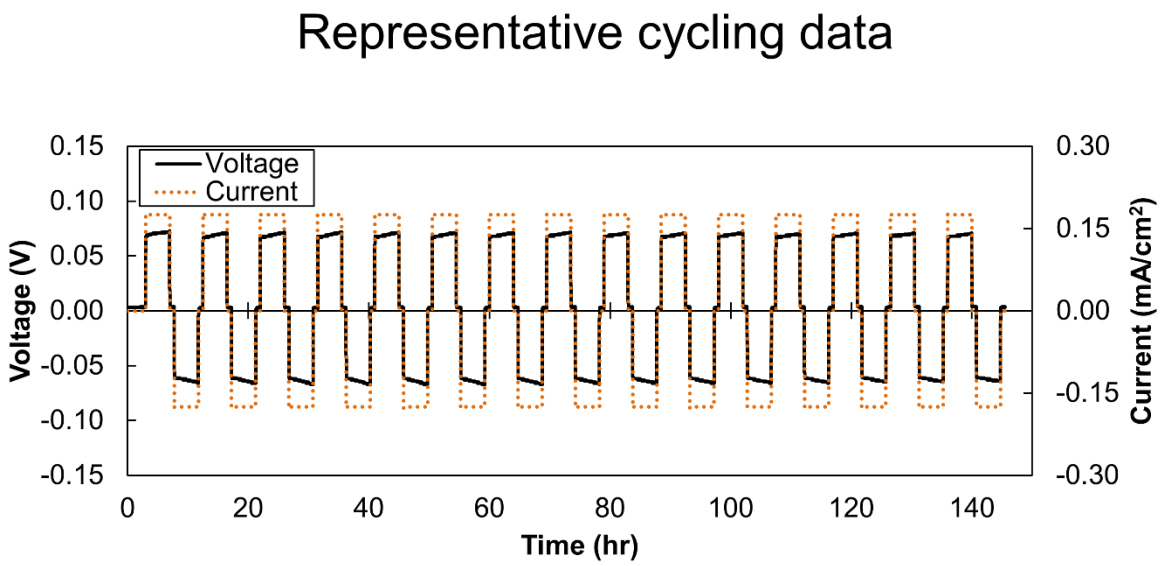

Figure 3.1 **Chronopotentiometry.** Representative cycling data for a lithium metal symmetric cell with a solid polymer electrolyte is shown. When a current density of 0.175 mA/cm^2 is applied to the cell, it responds with a voltage around 0.07 V. An alternating positive and negative current is applied to the cell to simulate the conditions of a battery charging and discharging. The sample rests for 45 minutes between each 4 hour charge and discharge.

Typical microtomography images taken of a symmetric lithium-lithium sample with a solid polymer electrolyte membrane and a schematic of the instrument used to obtain the data are shown in Figure 3.2. An example of a radiograph image is shown in Figure 3.2a. Once a series of

radiographs are collected from many angles, the radiographs are reconstructed into a stack of image files. These reconstructed image files are cross-sectional slices through the sample and can be viewed with open source software like ImageJ [113,114], or commercial software like Avizo. Figure 3.2b shows an example of a cross-sectional slice taken from the stack of reconstructed images. This symmetric cell was cycled until it failed by electronic short-circuit. From the reconstructed images, it is apparent that the majority of the lithium metal electrode interface is featureless. However, one finds globular lithium structures extending through the solid polymer electrolyte membrane like that shown in the 3D rendering in Figure 3.2c. The globular features in the polymer electrolyte in Figure 3.2c are shrouded by the electrolyte itself. In contrast, the uniform character of the globular dendrite is clearly seen in the cross-section (Figure 3.2b). It is, perhaps, interesting to note that the radiograph image in Figure 3.2a has much less noise than the reconstructed slice shown in Figure 3.2b. The main advantage of the reconstruction is the clarity with which the dendritic structure can be seen; the dendritic structure cannot be discerned in Figure 3.2a.

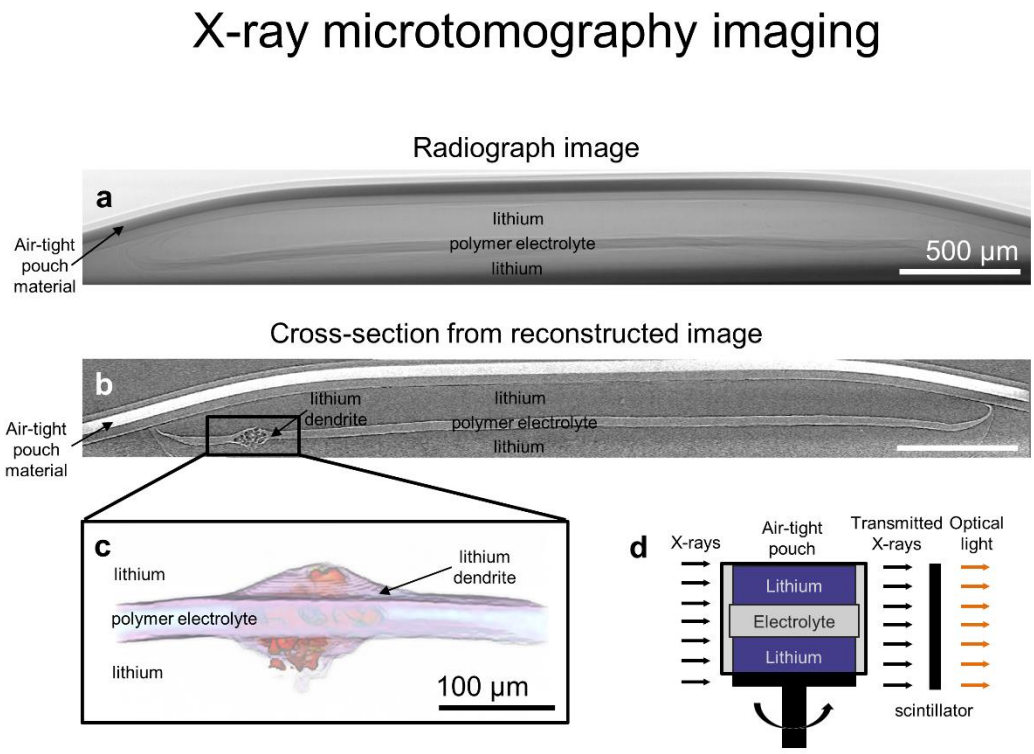

Figure 3.2 **X-ray microtomography.** Synchrotron hard X-ray microtomography is used to image a symmetric lithium cell that was cycled and failed by short circuit. **a** A radiograph image of the sample shows a dark polymer electrolyte band sandwiched between two lithium metal electrodes. The pouch material also appears in the image. **b** A cross-section slice through the reconstructed tomogram containing a lithium dendrite is shown. After reconstruction, the polymer electrolyte appears as a bright band sandwiched between two dark lithium metal electrodes. The pouch material also appears in the image. **c** Image segmentation was used to make a three-dimensional rendering of features in the sample. The dark, globular lithium metal dendrite is rendered in orange, so that the viewer can see its structure, while the bright, polymer electrolyte is rendered in purple. The top and bottom

lithium metal electrodes are rendered transparent so they do not obscure the polymer electrolyte and the dendrite. **d** A schematic of the sample setup for X-ray microtomography experiments is shown.

3.4 Discussion

Hard X-ray microtomography is especially well-suited for air-sensitive samples, like many electrochemically active materials, since the X-rays can penetrate through protective pouch material, enabling facile imaging of the sample without exposure to air. Perhaps the most valuable characteristic of this imaging technique is that the penetrating X-rays allow the user to see inside of the sample without destroying it. Most common imaging techniques, like scanning electron microscopy and traditional optical microscopy, can only image the surface of the electrodes. As such, many morphological changes that occur beneath the surface are hidden. X-ray imaging, however, allows the user to easily monitor the sample interior.

The theoretical resolution of this technique is less than a micrometer, but practical resolution is limited by absorption contrast and image noise. Also, the distance between the imaged region of the sample and the detection system impacts the resolution. Depending on the size of the pouch, the detection system is often 1-5 cm away from the central portion of the pouch, which contains the imaged material. This distance limits the resolution of the scan, both due to the rise of phase contrast artifacts with increasing distance, but also due to geometric blurring. Furthermore, the pixel size, determined by the magnification of the lens, will clearly influence the achievable resolution. X-ray absorption is a function of the atomic scattering factor, incident beam wavelength, and sample dimensions [115]. Roughly speaking, in the hard X-ray regime, the larger the atom, the more X-ray absorption occurs. Therefore, when imaging lithium dendrites, one can differentiate between lithium metal and the polymer electrolyte because the carbon-based electrolyte is more X-ray absorptive than lithium metal. Next, one must consider image noise. If the sample contains components made of large atoms, like nickel, a high percentage of the 20 keV X-rays will be absorbed by those components. If the majority of the X-rays are absorbed by these heavy components, the contrast between components made of lighter elements, like carbon and lithium, becomes negligible. We thus removed the nickel tabs from the cell before imaging.

The most critical step of the protocol is ensuring that the sample is designed in such a way that heavy metals like Nickel do not block the beam trajectory during imaging. The protocol described above is for ex-situ imaging, and while less destructive than TEM or SEM imaging, still requires the sample to be destroyed. Efforts to create samples for in situ imaging by altering the position of the current collectors so that they do not block the path of the beam are currently underway.

To conclude, X-ray microtomography is a valuable tool for studying morphological changes in electrochemically active systems. Since the image resolution is limited to the micrometer scale,

---

Note: As discussed in Chapter 1, the term “dendrite” implies branching. The structures shown here are unbranched and would be more aptly described as multi-globular structures. However, given the prevalence of the use of “lithium dendrite” to describe the structures that cause batteries to fail by short-circuit in the electrochemical literature, these globular structures are referred to as dendrites in this chapter.

complementary experiments using traditional electron microscopy can help to clarify morphological changes on smaller length scales. Furthermore, some spectroscopic information can be obtained from this technique by taking images above and below the absorption edge of the element to be identified. Components in the sample containing that element will show a large change in contrast when the images are compared. However, this only works if the experimenter knows what element they wish to identify. Therefore, complementary spectroscopic techniques like Energy-dispersive X-ray spectroscopy would be necessary to identify unknown components in a sample. Using this tool, we were able to study the formation and growth of lithium dendrites through high modulus polymer electrolyte membranes [109]. We expect that the technique can be extended to study many micron-scale morphological changes that may occur upon cycling an electrochemical cell.

3.5 Acknowledgements

Primary funding for the work was provided by the Electron Microscopy of Soft Matter Program from the Office of Science, Office of Basic Energy Sciences, Materials Sciences and Engineering Division of the U.S. Department of Energy under Contract No. DE-AC02-05CH11231. The battery assembly portion of the project was supported by the BATT program from the Vehicle Technologies program, through the Office of Energy Efficiency and Renewable Energy under U.S. DOE Contract DE-AC02-05CH11231. Hard X-ray microtomography experiments were performed at the Advanced Light Source which is supported by the Director, Office of Science, Office of Basic Energy Sciences, of the U.S. Department of Energy under Contract No. DE-AC02-05CH11231. Katherine J. Harry was supported by a National Science Foundation Graduate Research Fellowship.

Chapter 4 – Lithium Dendrite Growth in Glassy and Rubbery Nanostructured Block Copolymer Electrolytes

ABSTRACT

Enabling the use of lithium metal anodes is a critical step required to dramatically increase the energy density of rechargeable batteries. However, dendrite growth in lithium metal batteries, and a lack of fundamental understanding of the factors governing this growth, is a limiting factor preventing their adoption. Herein we present the effect of battery cycling temperature, ranging from 90 to 120 °C, on dendrite growth through a polystyrene-*block*-poly(ethylene oxide)-based electrolyte. This temperature range encompasses the glass transition temperature of polystyrene (107 °C). A slight increase in the cycling temperature of symmetric lithium-polymer-lithium cells from 90 to 105 °C results in a factor of five decrease in the amount of charge that can be passed before short circuit. Synchrotron hard X-ray microtomography experiments reveal a shift in dendrite location from primarily within the lithium electrode at 90 °C, to primarily within the electrolyte at 105 °C. Rheological measurements show a large change in mechanical properties over this temperature window. Time-temperature superposition was used to interpret the rheological data. Dendrite growth characteristics and cell lifetimes correlate with the temperature-dependent shift factors used for time-temperature superposition. Our work represents a step toward understanding the factors that govern lithium dendrite growth in viscoelastic electrolytes.

4.1 – Introduction

Energy density and safety are two parameters that drive current research for improved rechargeable lithium batteries in applications such as electric vehicles and personal electronics [9]. Many groups around the world are working on innovative battery chemistries, such as lithium-sulfur [11,116-118] and lithium-air [117,119-121], in an effort to improve battery energy density. Virtually all approaches that affect a substantial increase of the energy density of rechargeable batteries beyond that of lithium-ion batteries require the use of a lithium metal anode [11,122]. Gallagher et al. show that coupling a lithium metal anode with currently available lithium cathodes results in energy densities that are three to six times larger than existing batteries used in electric vehicles. Likewise, lithium-sulfur and lithium-air chemistries rely on lithium metal anodes for improved energy density; battery energy densities obtained using a conventional graphite anode with sulfur and air cathodes are similar to those of traditional lithium ion batteries [5].

† This chapter was reported in *Journal of The Electrochemical Society* **162**, A398-A405 (2015).

The adoption of rechargeable lithium metal anode batteries has been hindered, however, by the formation of dendrites during battery cycling [9,56,57]. Upon repeated stripping and deposition, lithium metal deposits unevenly on the anode, creating protrusions that grow and eventually short the cell [109]. Not only is the battery then unusable, but the flammable nature of typical liquid and gel electrolytes based on alkyl carbonates can result in catastrophic failure [9,123]. Uncontrolled deposition of lithium metal can also take place in a conventional lithium-ion cell with a graphitic anode if the charging rate is not properly controlled [124]. Therefore, much research has focused on finding electrolytes that are stable against lithium metal anodes and on characterizing the state of lithium metal anodes during cycling [53,125-130].

Polymer electrolytes are a nonflammable alternative to conventional liquid and gel electrolytes, and undoubtedly improve device safety [20,131]. The most common polymer electrolyte studied is a mixture of lithium salts and poly(ethylene oxide) (PEO) [131-135]. Though PEO-based electrolytes address the flammability issue of liquid electrolytes, they are still unable to prevent dendrites from growing across the electrode gap [27-29,32]. Pioneering theoretical work of Monroe and Newman indicated that solid electrolytes with a high shear modulus would suppress dendrite growth [49]. This turned attention to improving electrolyte mechanical properties [84,125,136,137]. Unfortunately, PEO-based electrolytes are only conductive in the rubbery state [138]. One method to increase the electrolyte modulus is to use block copolymers, combining PEO with a rigid polymer such as polystyrene (PS) [23,30,139]. The well-established phenomenon of microphase separation results in the formation of cocontinuous stiff PS-rich domains and rubbery PEO-rich domains. The typical widths of these domains range from ten to several hundred nanometers [140]. Previous studies have shown that nanostructured electrolytes based on polystyrene-*b*-poly(ethylene oxide) (SEO) greatly improve cycle lifetime compared to PEO [30,33].

Significant work is being done to gain a fundamental understanding of the complex factors that govern the formation, growth, and morphological characteristics of structures formed during lithium stripping and plating. A large majority of studies were conducted in liquid electrolytes wherein protrusions of different geometries were obtained depending on factors such as current density, electrolyte viscosity, additives, etc [53,141-143]. The switch to a solid polymer electrolyte resulted in a significant change in dendrite morphology [109]; however, the factors governing this change were unclear due to the large number of variables that change between different electrolyte systems. This present work bridges the dendrite morphology results obtained in solid and liquid electrolytes through the use of only a single electrolyte material. By changing only the cycling temperature, we are able to observe dendrite morphologies characteristic of solid electrolytes [109] and liquid

---

Note: As discussed in Chapter 1, the term “dendrite” implies branching. The structures shown here are unbranched and would be more aptly described as multi-globular structures. However, given the prevalence of the use of “lithium dendrite” to describe the structures that cause batteries to fail by short-circuit in the electrochemical literature, these globular structures are referred to as dendrites in this chapter.

electrolytes [27]. Thus, a direct connection between electrolyte modulus and dendrite morphology is revealed.

Recent X-ray microtomography experiments have shown that repeated cycling of lithium/SEO symmetric cells results in the formation of globular dendritic structures at the lithium metal/SEO interface, with much of the dendrite residing within the lithium electrode [109]. The existence of these subsurface features in the lithium electrode suggested that the mechanism of dendrite nucleation and growth in block copolymers was fundamentally different from that in liquid electrolytes: numerous studies of dendrite formation in liquid and gel electrolytes have concluded that dendrites emanate from the electrode/electrolyte interface with no evidence of subsurface structures [14,88,144,145]. The subsurface dendritic structures reported in reference [109] were obtained from cycling symmetric cells at 90 °C – below the glass transition temperature (T_g) of the PS-rich microphase and above the T_g and melting temperature of the PEO-rich microphase. It is not clear if the difference in lithium dendrite morphology observed between SEO and liquid electrolytes is due to changes in electrolyte modulus or due to the nanostructured nature of SEO.

In this paper, we report on the effect of cycling temperature on dendrite formation in lithium-SEO-lithium cells, in an effort to improve the fundamental understanding of the factors governing dendrite growth through a single polymer electrolyte system. We cover a relatively narrow range of temperatures, from 90 to 120 °C. The morphology of the nanostructured electrolyte is insensitive to temperature changes in this regime [146]. The mechanical properties of SEO, however, change dramatically over this temperature range because the T_g of the PS-rich microphase is 107 °C. The theory of Monroe and Newman [49] is limited to interfaces between lithium electrodes and ideal solid electrolytes that are characterized by a constant shear modulus. On the other hand, the shear moduli of polymers are complex, i.e. they have in-phase and out-of-phase components, and depend strongly on frequency in addition to temperature. In other words, the shear modulus is not a well-defined constant but rather, can vary by orders of magnitude depending on the frequency of interest. The energy required to deform polymers thus depends not only on instantaneous strain but strain history. One of the goals of this paper is to begin to address this complexity.

4.2 – Experimental

4.2.1 – Electrolyte Preparation

The relevant properties of the SEO copolymer used in this study are provided in Table 1 [140]. This SEO was synthesized and prepared by our group as described in Singh et. al. [23]. All sample preparation and cell assembly was carried out in an argon glovebox with less than 0.1 parts per million (ppm) H_2O and less than 8 ppm O_2. A mixture of lithium bis(trifluoromethanesulfone)imide (LiTFSI) salt and SEO was used as the electrolyte. The molar ratio of lithium ions to ethylene oxide monomers, *r*, was held fixed at 0.085. This ratio was used because it was found to maximize the conductivity of SEO electrolytes [100]. The mixture was dissolved in 1-methyl-2-pyrrolidone (NMP) at 90 °C and the solution was then cast onto smooth nickel foil using a home-built casting device operated at 60 °C. The film was left on the solvent caster at 60 °C for at least 12 h, and then placed into an evacuated antechamber at 90 °C for at least 12 additional h to remove any residual solvent. Due to natural variation on solvent casting, final film thicknesses were 27±9 μm.

There were no discernible correlations between film thickness and the results presented in this paper.

Publication Name	M_{PS}[a] (kg/mol)	M_{PEO}[a] (kg/mol)	ϕ_{EO}[b]	PDI[b]	Morphology	Domain spacing (nm)
SEO (240-269)	240	269	0.50	1.26	Lamellar	242

Table 4.1 **Key properties of the polystyrene-*block*-poly(ethylene oxide) polymer electrolyte used in this study.**

[a]M_{PS}/M_{PEO} is the molecular weight of the polystyrene/poly(ethylene oxide) block, respectively. [b]ϕ_{EO} is the volume fraction of the ethylene oxide block, and PDI is the polydispersity index.

4.2.2 – Li-SEO-Li Symmetric Cell Assembly

A 0.5 inch diameter disk of electrolyte was punched from the film prepared as stated above, and sandwiched between two 150 µm thick, 7/16 inch diameter disks of lithium foil (FMC Lithium). A nickel current collector tab was placed on both sides of the symmetric cell and the assembly was vacuum sealed on all sides in a polypropylene-lined aluminum pouch.

4.2.3 – Galvanostatic Cycling

Cells were galvanostatically cycled using either a Maccor Series 4000 Battery Tester or a Biologic VMP3 potentiostat. Cells were allowed to equilibrate at the temperature of interest for an hour before cycling. Each cell was then first subjected to five conditioning cycles. During each cycle, a current density of 0.02 mA/cm^2 was imposed in one direction for 4 h, followed by a 45 min rest period, followed by the imposition of a constant current density of 0.02 mA/cm^2 in the opposite direction, followed by another 45 min rest period. Cells were then cycled with the same time intervals at a current density of 0.175 mA/cm^2 until a sudden drop in the voltage required to maintain the target current density was observed. This was taken as the signature of a dendrite short. The thickness of lithium transferred between the electrodes in each half cycle at 0.175 mA/cm^2 was 3.13 µm.

4.2.4 – Linear Rheology Measurements

A neat polymer sample was prepared inside an argon glovebox by adding polymer into a 0.9 mm thick polycarbonate spacer with an 8 mm diameter hole, and pressing it between two Teflon sheets in a hand press heated to 120 °C. Enough polymer was sequentially added to the spacer such that a slight bulge of polymer was seen to protrude from above the spacer. The sample was left in the press at temperature for around 4 h, then removed from the spacer using a metal punch and placed back into the hand press between Teflon sheets for an additional 2 h. The polycarbonate spacer was placed in the press next to the sample so that the thickness of the sample would exactly match that of the spacer. The final sample, an opaque 8 mm diameter disk, was transferred in a dessicator to a Rheometric Scientific ARES Rheostat. Meanwhile, the rheometer plattens were cleaned and heated to 90 °C under nitrogen. The platten gap position was zeroed and then the sample was placed between the plattens – the sample had contact with air for less than 2 min before the oven was closed and nitrogen flow resumed. The plattens were then heated to 120 °C and the sample was

left to equilibrate for 1 h. At each measurement temperature, a dynamic strain test was performed at a frequency of 10 rad/s to ensure measurement in the linear regime. Then a dynamic frequency test was performed at a low strain in the linear regime, chosen such that the torque applied by the instrument was always above 0.2 gm-cm, which ensured accurate measurements. Thermal expansion of the metal plattens was accounted for when recording sample thickness at each temperature. Temperatures used for measurements were 120, 112, 105, 97 and 90 °C. Each time the temperature was changed, the sample was left to equilibrate for 30 min. A normal force between 10 and 40 gm was applied to the sample during measurement to ensure adequate adhesion to the plattens. The experiments were repeated with a salty polymer sample (r = 0.085). Due to limited material, only one sample of each type was made but experiments at each temperature were repeated several times. Slight pink discoloration of the neat sample was noticed before the tests and was taken to be a sign of contamination. An attempt to scrape away most of the discoloration was fairly successful but the sample still contained some surface contamination. Final sample thicknesses were around 0.88 mm. Good sample adhesion to the plattens was confirmed during the removal process, as significant temperature and effort were needed to separate the sample from the plattens. No significant difference in modulus between neat and salty samples was found, similar to a previous study by our group [23]. This is expected if the mechanical properties of the block copolymer are governed by the PS block; the salt resides primarily in the PEO-rich microphase. Values shown in this work are averages of both samples.

4.2.5 – Hard X-ray Microtomography

Hard X-ray microtomography imaging of our cells was performed at Beamline 8.3.2 at the Advanced Light Source at Lawrence Berkeley National Laboratory [58,105]. All of the cells studied by X-ray microtomography were first cycled until they shorted. Shorted symmetric cells were prepared for the microtomography experiments in an argon environment in a glovebox. A 1/8 inch diameter punch was used to cut out the central portion of each cell, and any remaining nickel current collectors were removed. A smaller sample and removal of the highly absorbing nickel tabs leads to better image quality. The smaller sample was then vacuum sealed in a new pouch and imaged at the beamline at 4x and 10x magnifications with a beam energy of 20 keV. A total of 7 cells were imaged at 90 °C, 8 were imaged at 105 °C and 8 were imaged at 120 °C. Thus the total electrode/electrolyte interface area imaged at each temperature was 110.8 mm^2, 126.7 mm^2, and 126.7 mm^2. The pixel size of the images was 0.00161 mm^{-2} and 0.000646 mm^{-2} for the 4x and 10x magnifications, respectively. Images were preprocessed, and tomographic reconstruction was performed using Fourier methods with the commercial Octopus software. A median filter was used to process the images prior to further analysis. Reconstructed three dimensional (3D) images were analyzed using the commercially available Avizo software package. Data acquisition and analysis builds on methods described in reference [109].

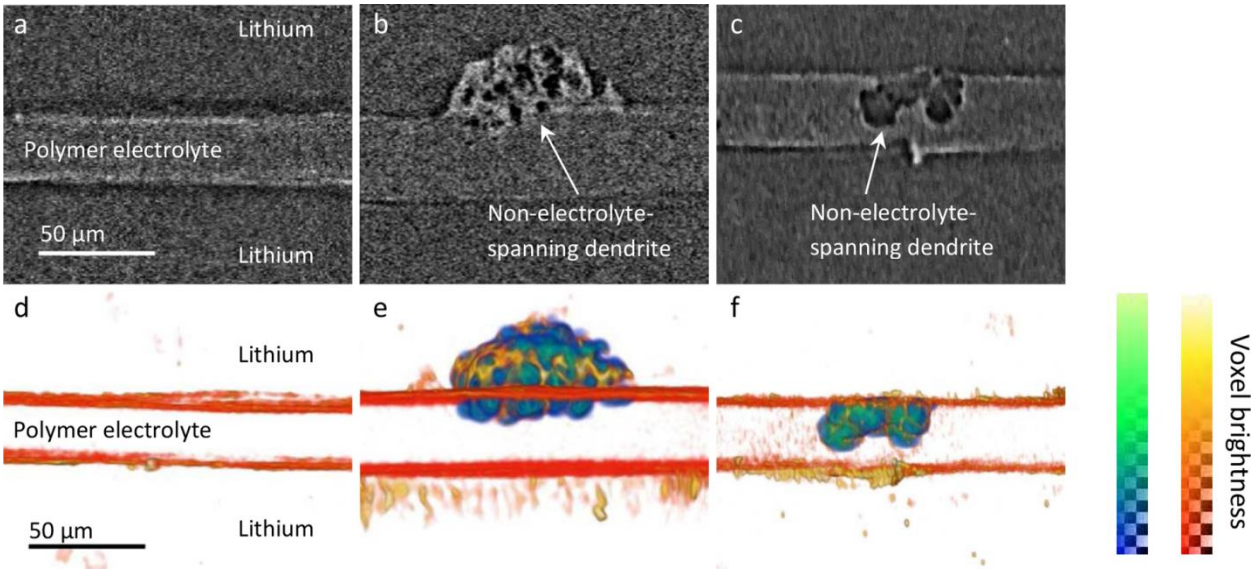

Figure 4.1 **Representative digital cross-sections of 3D reconstructed X-ray microtomography images** of **a** an uncycled symmetric cell, **b** a non-electrolyte-spanning dendrite in a cell cycled at 90 °C, and **c** a non-electrolyte-spanning dendrite in a cell cycled at 105 °C. Volume renderings of **a**-**c** are shown in **d**-**f**, respectively. The dendrites are rendered using a blue-green colormap, while the interfaces between the electrodes and electrolyte are rendered using a red-yellow colormap. The added color bars serve as a reference for voxel brightness but do not necessarily accurately depict the relative brightness values in each image.

In Figure 4.1a we show a digital cross-section through a reconstructed 3D X-ray microtomography image of an uncycled lithium symmetric cell used in our experiments. The image contains three distinct regions – a brighter 30 µm-thick polymer electrolyte sandwiched between two darker slices of lithium metal. The grayscale pixel values in the image correspond to the relative X-ray linear absorption coefficients of the material at that position – brighter pixels correspond to higher X-ray absorption at that point. Thus, the lithium electrodes appear darker than the polymer electrolyte in Figure 4.1a because they are more X-ray transmissive. The electrode-electrolyte interface is embellished by a thin dark band on the electrode side and a thin bright band on the electrolyte side; this is a result of Fresnel phase contrast arising during the imaging of samples containing interfaces [147]. Effects of Fresnel phase contrast are also apparent within the dendrites. Within each phase, there can be real variations in pixel brightness due to variation in X-ray absorption, but a portion of the variation is also due to numerous sources of noise.

In Figure 4.1b we show an X-ray microtomography cross-sectional image of a cell cycled at 90 °C. The dendritic structure obtained in the presence of our SEO electrolyte is composed of globular clusters, which is distinct from mossy or needle-like dendrites seen on lithium electrodes cycled in conventional electrolytes [28,88,148]. For simplicity, we refer to structures formed at the electrode-electrolyte interface due to cell cycling as dendrites. Consistent with data presented in reference [109], the dendritic structure shown in Figure 4.1b is a composite, comprising both lithium and polymer, and it resides predominantly within one of the lithium electrodes. We note that the brightness variations

within and around the dendrite arise in part due to phase contrast effects between the lithium and electrolyte described previously, but could also arise from the existence of compounds with greater X-ray absorption coefficients. For example, because LiTFSI salt has a higher X-ray absorption coefficient than the SEO copolymer, brighter regions in the image could indicate higher concentrations of LiTFSI salt. The image features enable differentiation of the dendritic structure from either the electrode or electrolyte phases. In Figure 4.1c, we show a typical dendritic structure formed when the cell is cycled at 105 °C. This dendritic structure is more uniform than that in Figure 4.1b; it is evident that the dendritic structure formed at 105 °C is composed of larger lithium substructures than occur in dendrites observed at 90 °C. In addition, most of the dendritic structure obtained while cycling at 105 °C resides within the electrolyte. There are thus qualitative differences in the dendritic structures formed at 90 and 105 °C. In a given cell, dendrites were observed to grow from both electrodes roughly equally; for simplicity the images in Figure 4.1 are oriented so the dendrites originate from the top electrode. Due to image editing, the pixels depict relative, not absolute, absorption values. This accounts for the slight brightness variations seen between Figures 4.1a, b and c.

Stacks of slices of the type shown in Figure 4.1a-c were combined into volumes to generate 3D visualizations of the sample volumes of interest, shown in Figures 4.1d-f. The visualizations in these figures, known as volume renderings, are based on a colormap which maps pixel values in the 3D volume array onto both color and opacity values. The dendritic structures were digitally labeled, or "segmented", by manually selecting their area on a subset of slices through the volume and then interpolating to fill in the remaining areas. The bright regions within the dendritic structures (see Figure 4.1b) were assumed to represent the electrolyte and hence were not selected as part of the lithium dendrite. For the dendrite volume renderings in Figures 4.1d-f, lower pixel brightness values are mapped to blue and transparent and higher pixel values to green and opaque. The regions outside the dendrite were rendered using a separate red-yellow colormap. Using these two colormaps facilitates the identification of the electrode-electrolyte interfaces. Thus in the figures, only the dendrite and the electrode-electrolyte interfaces are rendered, allowing clear visualization of the large difference in dendrite volume located in the lithium electrode; compare Figures 4.1d and e. After dendrite segmentation, the dendrite volume can be determined by counting the number of voxels (3D pixels) that have been labelled as dendrite.

4.3 – Results and Discussion

Figure 4.2a shows typical voltage versus time data obtained from our symmetric lithium-polymer-lithium cells. Cells were cycled galvanostatically at a constant current density of 0.175 mA/cm^2, with 45 min rest periods between switches in current direction. For the cell in the figure, at times before 257 h, the voltage response is featureless, with values varying from 0.045 to -0.045 V. The small spikes seen in the first and second cycle in Figure 4.2a were observed throughout the cycling experiments, and may be due to unavoidable temperature fluctuations in the oven or unsteady processes within the cell. Deviations from steady cycling behavior are clearly visible at t = 313 h, where a sharp increase in voltage to -0.006 V is seen in spite of the imposition of a current density of -0.175 mA/cm^2. We take this – the first time a sudden change of voltage response greater than 50% of the steady-state value was recorded and observed to persist for the remainder

of the half cycle – as the signature of cell shorting. Cells sometimes recovered from this short circuit during subsequent cycles, as seen in Figure 4.2a, but generally failed permanently shortly thereafter. Similar cycling profiles were obtained at 105 and 120 °C.

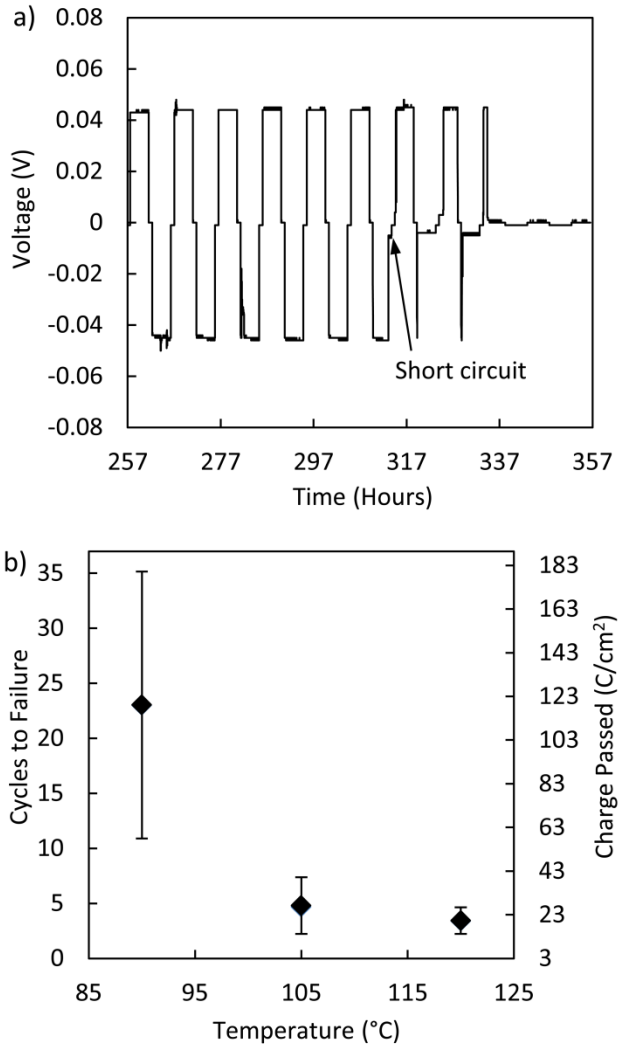

Figure 4.2 **a** Typical voltage versus time profile of a galvanostatically cycled symmetric cell, showing the last few cycles before cell shorting due to dendrite growth. **b** Average number of cycles to failure at 90, 105 and 120 °C. Conditioning cycles are not included. The right abscissa converts cycles to charge density passed, including charge passed during conditioning cycles (2.88 C/cm^2).

The total number of cycles to failure was counted as full cycles including the cycle where the voltage drop signifying a short was seen, but not including the first five conditioning cycles described in the Experimental Section. A minimum of ten cells were cycled at each temperature. Average values of the total number of cycles before failure were calculated for each temperature and the results are plotted in Figure 4.2b. All error bars shown in this study reflect the standard deviation of the data. The figure also converts this cycle number to amount of charge passed, including charge passed during the

conditioning cycles (2.88 C/cm^2), before failure – see the right-hand ordinate of the plot. The large variation in cell lifetime, especially at 90 °C, is probably due to the statistical nature of dendrite initiation and growth. We will show below that failed cells contained a wide variety of dendritic structures. Other factors such as imperfect control over electrolyte film quality, pressure applied during assembly, and impurities in the lithium foil may also contribute to the observed variance. In spite of the scatter in the data, it can be seen that cell lifetime decreases sharply as the cycling temperature is raised to 105 °C. Average lifetime decreased from 23 cycles at 90 °C to 4.7 cycles at 105 °C, a difference that is well outside experimental uncertainty. A further slight decrease in lifetime to 4.0 cycles was observed when the cycling temperature was increased to 120 °C. One might conclude that the ability of SEO electrolytes to resist dendrite growth is lost abruptly at temperatures above 90 °C.

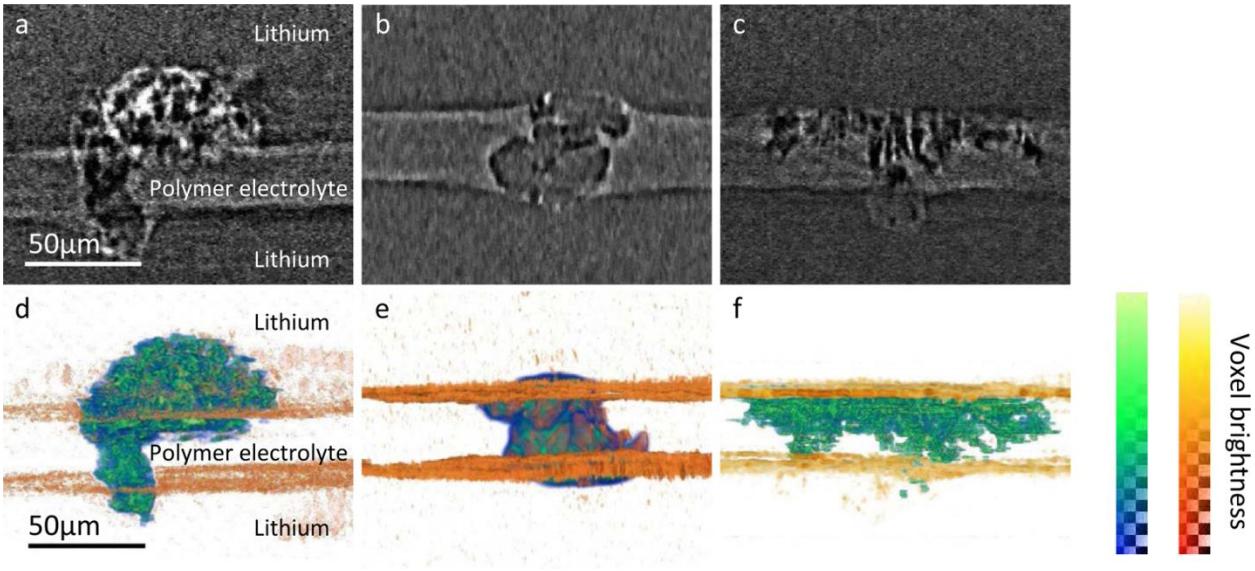

Figure 4.3 **X-ray tomography images of dendrites present in cycled symmetric lithium cells.** A typical electrolyte-spanning dendrite is shown for a cell cycled at **a** 90, **b** 105 and **c** 120 °C. **d-f** 3D volume renderings of the dendrites in **a-c** more clearly show the large difference in percentage of the dendrite located within the lithium electrodes (above top orange line and below bottom orange line) versus in the electrolyte (between the orange lines). Cycling temperatures were **d** 90, **e** 105, and **f** 120 °C. Again, the color bars show relative voxel brightness values but exact values do not directly correspond between any of the images shown.

The nature of dendrite shorts that led to cell failure was established by X-ray microtomography. Typical digital cross-sections of reconstructed tomography images of electrolyte-spanning dendrites obtained at 90, 105 and 120 °C are shown in Figures 4.3a, b, and c. Three-dimensional volume renderings of these dendrites are shown in Figures 4.3d, e, and f. At 90 °C, a large fraction of the dendritic structure is contained within the electrode (Figures 4.3a and d). In addition, the dendrite is a finely-divided composite, with 5-20 µm-wide dark globules of lithium metal surrounded by bright regions, composed of the SEO copolymer, LiTFSI and, perhaps, other organic compounds found in the SEI layer. In contrast, at 105 °C, a large fraction of the dendrite is contained within the electrolyte (Figures 4.3b and e). The lithium-rich regions in the dendrite are bulbous and much larger

at 105 °C relative to 90 °C, with correspondingly fewer inclusions of the polymer electrolyte. The dendrite at 120 °C (Figures 4.3c and f) shows elongated lithium structures in the direction of the applied current that differ qualitatively from the roughly spherical nodules seen at 90 and 105 °C. As was the case at 105 °C, most of the dendrite at 120 °C resides within the electrolyte. The polygonal structure in the bottom lithium electrode in Figure 4.3c is a crystalline impurity in the electrode. The role of crystalline impurities in the lithium metal anodes is discussed in reference [109].

In typical cells that were cycled at 90 and 105 °C, a wide variety of dendritic structures were observed. Most of them were not electrolyte-spanning, and examples of such structures are given in Figure 4.1. Since we punch out only a small fraction of the shorted cell for X-ray microtomography, electrolyte-spanning dendrites were not present in all samples imaged. At 120 °C, only a single dendritic structure was found in the 8 cells that were imaged. The remainder of the sample volumes contained no dendritic structures.

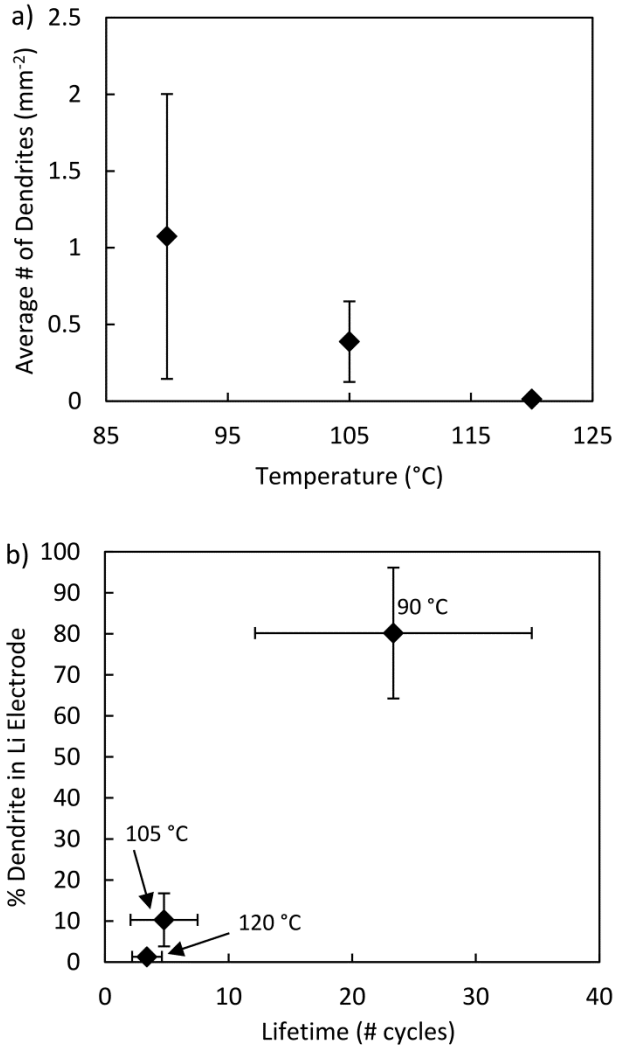

Figure 4.4 **a** Average number of dendrites seen per cell as a function of cycling temperature. **b** Average percentage of dendrite volume located in lithium electrode versus cell life-time for each cycling temperature.

In Figure 4.4a we plot the average number of dendrites per unit surface area, calculated by dividing the total number of dendrites observed by the total electrode-electrolyte interfacial area analyzed at each temperature, as a function of cycling temperature. The average number of dendrites per unit surface area decreased from 1.1 mm^{-2} at 90 °C to 0.4 mm^{-2} at 105 °C. This change in temperature resulted in a decrease in cell lifetime by a factor of 4.9 while the average number of dendrites per unit surface area decreased by a factor of only 2.8. It is unclear whether this corresponds to faster dendrite nucleation at higher temperature, since it is plausible that dendrite nucleation is nonlinear with time and amount of charge passed. The average number of dendrites per unit surface area at 120 °C was 0.008 mm^{-2}, a value significantly smaller than that obtained at lower temperatures. The reason for this dendrite scarcity, especially as compared to cells cycled at 105 °C, is unclear and cannot be explained by the slight decrease in cell lifetime. The factors that govern this nucleation rate could include changes in surface and concentration overpotential [42], and SEI layer with temperature. Further work is required to quantify these effects in low transference number electrolytes such as SEO. The influence on dendrite growth of the SEI layer is ignored in the current analysis.

Quantitative results for the average percent of dendrite residing in the lithium electrodes were also calculated from the X-ray tomograms. These percentages were then averaged over several independent dendritic structures at each temperature (16 at 90 °C, 10 at 105 °C, and 1 at 120 °C). At 90 °C, an average of 80 % of each dendrite resided within the electrode. In contrast, at 105 °C, only 10 % of each dendrite resided in the electrode, while at 120 °C this fraction reduces to 1 %. Percent of dendrite in the electrode is plotted as a function of cell lifetime in Figure 4.4b. Dendritic structures grow within the electrode in cells with long cycle life; in contrast, dendritic structures grow within the electrolyte in cells with short cycle life.

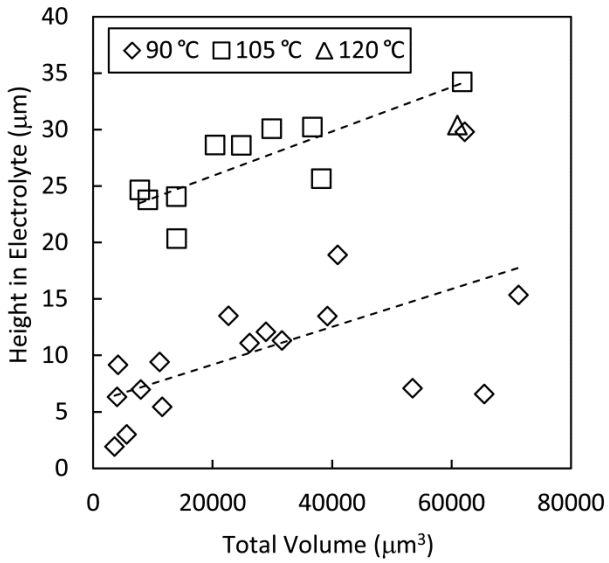

Figure 4.5 Height of dendrite protruding into the SEO electrolyte, in μm, plotted against total dendrite volume, in μm^3, for dendrites imaged in shorted cells cycled at 90, 105 and 120 °C. Linear fits to the 90 and 105 °C data are shown as dashed lines.

The average properties of dendrites reported in Figure 4.4 obscure the broad range of dendritic structures that were observed in our cells. To clarify this, we plot the dendrite height in the electrolyte versus total dendrite volume for all dendrites analyzed at each temperature in Figure 4.5. Dendrite height was measured as the perpendicular distance from the intersection of the dendrite with the electrode-electrolyte interface to the tip of the dendrite in the electrolyte. In order for a dendrite to short the cell, it must grow fully across the electrolyte; dendrite height in the electrolyte is therefore a metric for how close a dendrite is to causing cell failure. The data in Figure 4.5 indicates that this dendrite height is invariably smaller in a cell cycled at 90 °C than in a cell cycled at 105 °C across the wide range of dendrite sizes observed. Dendrites of a given volume in cells cycled at 105 °C are about 15 μm taller than those in cells cycled at 90 °C. They are thus more likely to reach the other electrode and short the cell at 105 °C.

Temperature (°C)	ΔV^a (V)	σ^b (S/cm)	$R_{int}{}^c$ (Ω cm^2)	R^d (Ω cm^2)	$\Delta V/\Delta V_{90}{}^e$	$R/R_{90}{}^e$
90	0.056	3.3×10^{-4}	136	144	1	1
105	0.021	4.5×10^{-4}	42.4	48.3	0.38	0.33
120	0.009	6.1×10^{-4}	15.5	19.6	0.15	0.14

Table 4.2 **Average symmetric cell properties at each cycling temperature.**

$^a\Delta V$ is the average steady-state voltage, $^b\sigma$ is the conductivity of our electrolyte, $^cR_{int}$ is the interfacial impedance, ^dR is the total cell impedance, and $^e\Delta V/\Delta V_{90}$ and R/R_{90} are the ratio of ΔV and R at the temperature of interest to that at 90 °C.

The average steady-state voltage during cycling, ΔV, was 0.056 V at 90 °C, 0.021 V at 105 °C and 0.009 V at 120 °C. The ranges of steady-state voltages during cycling were 0.026 to 0.133 V at 90 °C (see example in Figure 4.2a), 0.013 to 0.03 V at 105 °C and 0.0058 to 0.0115 V at 120 °C. We attribute this primarily to the decrease in resistance between the lithium electrodes as temperature increases. This is established in Table 2, where we list the temperature-dependent values of ΔV, the conductivity of our electrolyte, σ, interfacial impedance, R_{int}, and total cell impedance, R. These values were derived from ac impedance measurements made on all of the cells prior to cycling. Also given in Table 2 are $\Delta V/\Delta V_{90}$ and R/R_{90}, the ratio of ΔV and R at the temperature of interest to that at 90 °C. Similarity of R/R_{90} and $\Delta V/\Delta V_{90}$ values suggests that observations as a function of temperature are not due to differences in the rate of side reactions or changes in the electrochemical stability of the electrolyte; both factors would result in noticeable increases in interfacial impedance.

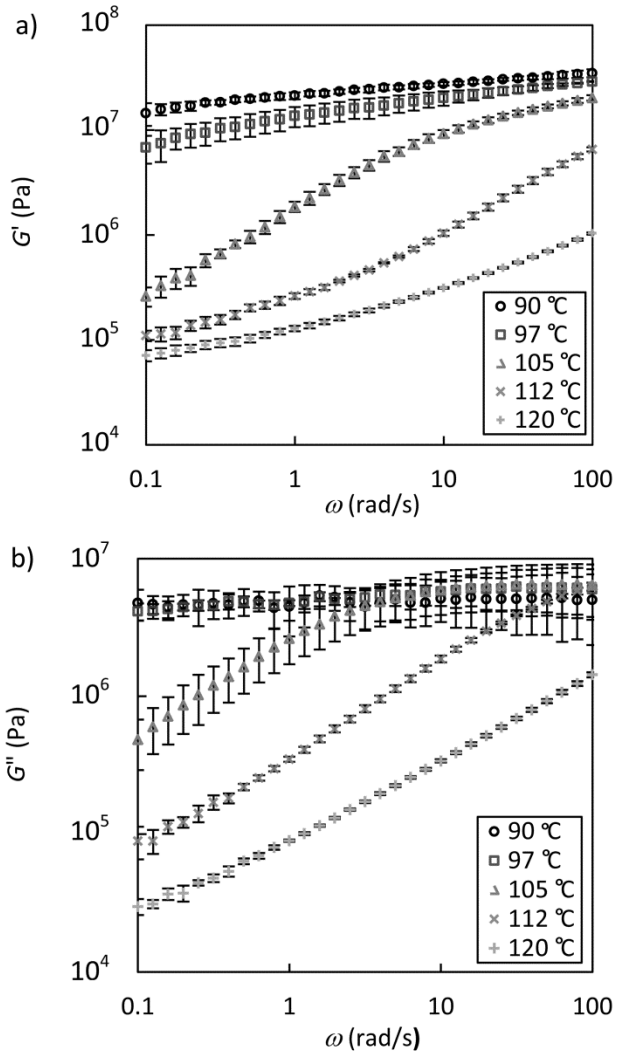

Figure 4.6 Frequency (ω) dependence of (a) storage (*G*') and (b) loss (*G*") moduli measured at 90, 97, 105, 112 and 120 °C.

Models of dendrite growth suggest that both electrochemical and mechanical properties are important in determining cell performance [43,49,149]. As established above, our cell cycling data suggest no unexpected major differences in interfacial impedance as a function of temperature. It is therefore appropriate to examine the temperature dependence of the mechanical properties of our polymer electrolyte. In Figures 4.6a and b we show the frequency (ω) dependence of the storage (*G*') and loss (*G*") moduli of SEO as a function of increasing temperature. Current models for dendrite growth assume the presence of an ideal elastic solid electrolyte [49]. Such a material would exhibit a ω-insensitive *G*' and negligible *G*" (<< *G*'). At low temperature (90 °C), the SEO copolymer is essentially elastic, reflecting the glassy rigidity of the PS domains. In contrast, at higher temperatures the magnitudes of *G*' and *G*" vary with ω and are comparable over wide ranges of ω and temperature. The softening of the SEO, seen as the temperature is increased from 97 to 105 °C, signifies the glass-to-rubber transition of the PS microphase; the T_g of the PS microphase in neat SEO and in the LiTFSI/SEO electrolyte, determined by differential

scanning calorimetry, was 108 and 107 °C, respectively. At these higher temperatures, the material becomes a viscoelastic solid, as seen by the low-ω plateau of G'. This feature could result from the elastic resistance to deformation arising from either the inter-domain interfaces or inter-grain defects.

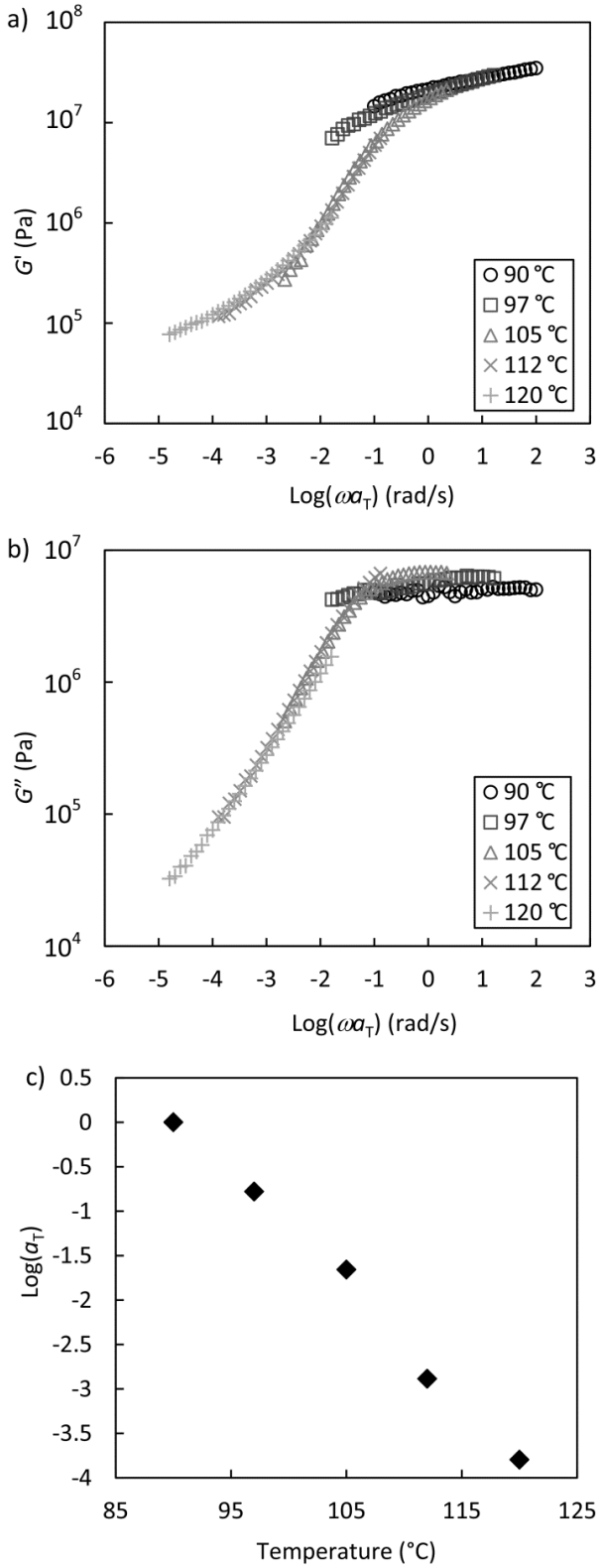

Figure 4.7 **Time-temperature superposition** of (a) *G*' and (b) *G*" of the data presented in Figure 4.6, with T_r = 90 °C. The same shift factors are used for both master curves. (c) Shift factors, log(a_T), plotted as a function of temperature.

Our observation that the SEO copolymer is a complex viscoelastic material is consistent with a large body of work on the rheological properties of block copolymers [150-154]. The standard approach for elucidating the ω-dependence of G' and G" of polymers over windows of ω that are not experimentally accessible is time-temperature superposition [155,156]. Application of this principle to the data in Figure 4.6 is shown in Figure 4.7, where the abscissa is $\log(\omega a_T)$, where a_T is the shift factor. The reference temperature, T_r, used for the time-temperature superposition is 90 °C, i.e. $a_T = 1$ at 90 °C. The G' and G" data are multiplied by a minor correction factor for entropy elasticity, $b_T = T_r/T$ (in K). The shift factors used to obtain Figure 4.7a were chosen manually to superpose the high-ω part of the G' versus ω data in Figure 4.6a onto a single master curve [151,154]. Figure 4.7b shows shifted G" versus $\log(\omega a_T)$ using the same shift factors as in Figure 4.7a. The temperature dependence of a_T is shown in Figure 4.7c. The shift works reasonably well for both G' and G" data at high temperature ($\geq$ 105 °C), though detectable deviations remain. Such deviations are often observed in nanostructured block copolymers comprising domains that present different activation energies due to differences in T_g [151,154,157,158]. The success of time-temperature superposition at high temperatures may have resulted from temperature-insensitivity of the viscoelastic response of the inter-domain interfaces and inter-grain defects [152], or from a decrease of the viscoelastic contrast between PS and PEO.

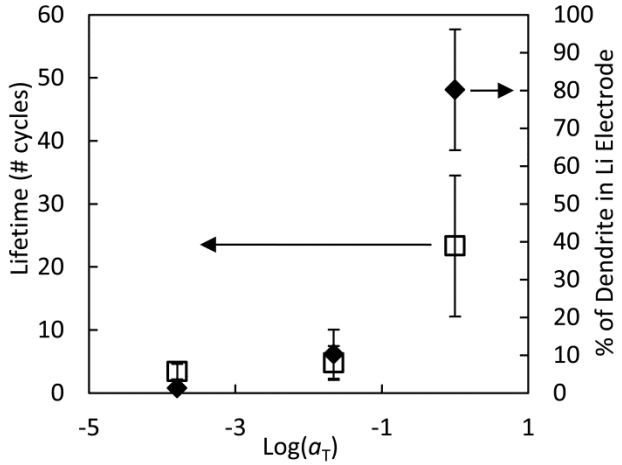

Figure 4.8 Average cell lifetime (squares) and average percentage of dendrite volume located in lithium electrode (diamonds) plotted versus shift factor, $\log(a_T)$, for data obtained at 90, 105 and 120 °C.

In Figure 4.8 we show the effect of the viscoelastic properties of the SEO electrolyte on dendrite growth. In this figure, we plot the cell lifetime, as obtained from the galvanostatic cycling data, and the percent of dendrite in the electrode, as obtained by X-ray microtomography, as a function of $\log(a_T)$. It is evident that when $a_T = 1$, dendrites reside primarily in the electrode. This may be taken as a signature of the electrolyte pushing back on the dendrite as it grows which, in turn, results in longer cycle life. The rigidity sustained by the glassy PS domain at this temperature is the main factor contributing to the mechanical resistance of the SEO. At lower values of a_T, the inter-domain interfaces and inter-grain defects are the dominant contributions to resistance of dendrite growth. As seen

from the significant decrease in cell lifetime and percent dendrite in the electrode, this resistance is much weaker compared to that arising from glassy domains. The local direction of dendrite growth is an important issue that the present experiments do not address directly. The presence of roughly spherical globular substructures at 90 and 105 °C suggests a lack of preference for a particular growth direction. Perhaps the characteristic dimensions of growing dendritic structures are large enough to average over several block copolymer domains that are randomly oriented in our samples. In contrast, the presence of elongated substructures in the direction of the electric field at 120 °C indicates a correlation between the direction of lithium migration and dendrite growth, which is consistent with a large body of literature on dendrite growth on metal surfaces against liquid electrolytes [88,148]. It is evident that our SEO electrolyte, which resisted dendrite growth at 90 °C, is similar to conventional electrolytes at 120 °C.

A thorough analysis of dendrite growth into viscoelastic polymer electrolytes would require the development of a framework that couples the deformation induced by uneven electrochemical deposition near a dendrite with the viscous flow and shear and normal stresses that occur due to the finite values of G' and G''. If the growth of the dendrite excites a particular frequency, then dendrite growth would be dependent on the values of G' and G'' at that frequency. It is, however, likely that dendrite growth excites a range of frequencies. In the absence of knowledge of the relevant range of frequencies, the proposed approach of using shift factors to compare dendrite growth at various temperatures is, perhaps, a logical first step toward characterizing dendrite growth in complex viscoelastic media. Further work is required to address this important issue.

4.4 – Conclusions

The relationship between temperature and dendrite growth in symmetric lithium/SEO electrolyte/lithium cells was studied by galvanostatic cycling and hard X-ray microtomography. A dramatic decrease in the amount of charge passed at cell failure was observed when cycling was conducted at 105 and 120 °C as compared to cycling at 90 °C. The nature of lithium dendrites that caused cell failure was determined by X-ray microtomography. At 90 °C, a large portion of the dendritic structure resided within the lithium electrode, while at 105 and 120 °C most of the dendrite was located within the electrolyte. An understanding of the reason for the shift in dendrite location with respect to the electrode-electrolyte interface was obtained by examining the rheological properties of the SEO copolymer. As the temperature was increased, both G' and G'' decreased significantly in the low frequency regime. Time-temperature superposition was employed to estimate G' and G'' over a wider range of frequencies than is experimentally feasible. Cycle life and the fraction of the dendritic structure located within the electrode were found to be sensitive functions of shift factors used to obtain time-temperature superposition.

4.5 – Acknowledgements

We thank Jing Sun of the University of California, Berkeley, for her help with the DSC sample preparation and measurements. Primary funding for the work was provided by the Electron Microscopy of Soft Matter Program from the Office of Science, Office of Basic Energy Sciences, Materials Sciences and Engineering Division of the U.S. Department of Energy under Contract No. DE-AC02-05CH11231. The battery assembly portion of the project was supported by the BATT program from the Vehicle Technologies program,

through the Office of Energy Efficiency and Renewable Energy under U.S. DOE Contract DE-AC02-05CH11231. Hard X-ray microtomography experiments were performed at the Advanced Light Source which is supported by the Director, Office of Science, Office of Basic Energy Sciences, of the U.S. Department of Energy under Contract No. DE-AC02-05CH11231. Katherine J. Harry was supported by a National Science Foundation Graduate Research Fellowship.

Chapter 5 – Electrochemical deposition and stripping behavior of lithium metal across a rigid block copolymer electrolyte membrane

ABSTRACT

Replacing the conventional graphite anode in rechargeable batteries with lithium metal results in a significant increase in energy density. However, growth of electronically conductive structures, like dendrites, from lithium anodes causes premature battery failure by short circuit. Mechanically rigid electrolytes are thought to promote smooth lithium deposition by increasing the energy required for lithium reduction at regions of high local strain, like a dendrite tip. The study reported herein used X-ray microtomography, Focused Ion Beam (FIB) milling, and Scanning Electron Microscopy (SEM) imaging to investigate the electrochemical stripping and deposition behavior of lithium in symmetric lithium – polymer cells using a rigid polystyrene-*b*-poly(ethylene oxide) membrane as the electrolyte. In situ experiments show the formation of globular lithium structures that grow to puncture the polymer electrolyte membrane. They form on faceted impurity particles that are initially located at the lithium/electrolyte interface. While the impurities are uniformly distributed throughout the lithium foil in initial images, their relative concentration near the electrolyte changes as lithium is stripped from one electrode and deposited on the other. Notably, the deposited lithium is devoid of faceted impurities. This electrolytic refining of lithium could be used to prepare anodic lithium foils for batteries with improved cycle life.

5.1 Introduction

Lithium metal is a highly desirable anode material for applications requiring a high energy density battery due to its electropositivity and low atomic mass. Simply replacing the traditional graphite anode with lithium metal in a conventional lithium ion battery results in a significant increase in specific energy. Next generation battery chemistries, like lithium-sulfur and lithium-air, presume the use of a lithium metal anodes to achieve theoretical specific energies of 2458 Wh/kg and 5217 Wh/kg respectively [5,10,159]. The theoretical specific energies of the sulfur and air battery chemistries fall to 572 and 939 Wh/kg if a traditional graphite anode is substituted for lithium metal. Given its importance in high energy density battery chemistries, there is strong motivation to understand the redox behavior of lithium metal.

Notably, lithium metal tends to form dendrites as lithium ions deposit on the lithium metal foil during battery charging [14,15,42,56,57]. Lithium dendrites propagate through the electrolyte layer, and when they reach the cathode, the battery fails by short-circuit [41,43]. This failure can be catastrophic if it occurs in the presence of a flammable electrolyte. Consequently, the use of

---

† This chapter was reported in *Journal of The Electrochemical Society* **162**, A2699-A2706 (2015).

lithium metal anodes with traditional liquid electrolytes is generally considered unsafe [9]. Furthermore, liquid electrolytes form a mechanically unstable solid electrolyte interface (SEI) layer with lithium metal. This exacerbates lithium dendrite growth, resulting in premature battery failure [8,160,161]. Polymer electrolytes, like poly(ethylene oxide), form a more stable SEI layer when cycled against lithium metal [20,162]. Additionally, high molecular weight poly(ethylene oxide) is nonflammable unlike traditional carbonate-based liquid electrolytes. Therefore, polymer electrolytes are a promising candidate for enabling the safe use of the lithium metal anode.

Despite its improved stability toward lithium metal, dendrites still grow through poly(ethylene oxide) electrolyte membranes causing battery failure by short-circuit [26,27,29,32]. Recent experiments have shown that the stability of the lithium metal anode is enhanced when a composite comprising co-continuous, nanoscale domains of rubbery poly(ethylene oxide) that conduct lithium ions and glassy polystyrene domains that provide mechanical rigidity is used as the electrolyte [30,33]. These composites are conveniently obtained by self-assembly of polystyrene-*b*-poly(ethylene oxide) (SEO) block copolymers. Theoretical work by Monroe and Newman indicates that a stiff electrolyte results in smoother deposition of lithium because there is an energetic penalty associated with a reduction event in a region of high local strain [49]. There is growing interest in understanding lithium deposition and dendrite growth through high-modulus electrolytes [109,163-166]. The goal of the present study is to expand our qualitative understanding of lithium deposition and stripping against rigid SEO block copolymer electrolytes.

5.2 Experimental

A 240-260 kg/mol polystyrene-*b*-poly(ethylene oxide) copolymer was synthesized via anionic polymerization as described previously [167,168]. This polymer self-assembles into a lamellar morphology with a domain spacing of 241 nm. The polydispersity index is 1.26 and the volume fraction of ethylene oxide is 0.50 without salt. Lithium metal foil was purchased from FMC Lithium at 99.9% purity. The foil thickness was 150 μm. All sample preparation was performed in a glovebox filled with 99.999% pure Argon gas. The oxygen and water levels were controlled and remained below 5 ppm.

5.2.1 Electrolyte preparation

Freeze-dried polymer electrolyte was mixed with lithium bis(trifluoromethane)sulfonamide salt (LiTFSI) at a concentration of 0.085 Li^+ to ethylene oxide moieties and dissolved together in anhydrous N-Methyl-2-pyrrolidone (NMP). The polymer and salt solution was cast onto nickel foil and smoothed using a doctor blade. After allowing the membrane to dry on the casting plate at 60 °C overnight, tweezers were used to peel the polymer electrolyte membrane from the nickel foil. The free standing film was allowed to dry further under vacuum at 90 °C overnight. The thickness of the polymer electrolyte membrane was measured using a micrometer and was 30 μm thick.

5.2.2 Sample preparation for ex situ, post mortem X-ray tomography

Symmetric lithium – polymer electrolyte – lithium samples for post mortem X-ray tomography imaging were assembled using the following technique. A 1/2 inch diameter metal punch was used to cut a disc from the polymer electrolyte membrane. A 7/16 inch diameter metal punch was used to cut two lithium metal electrodes from a roll of lithium metal foil. The polymer electrolyte disc was sandwiched between the two lithium metal electrodes. Nickel tabs were placed on the two

electrodes and the samples were vacuum sealed in aluminum pouch material lined with polypropylene and nylon. The sealed sample was removed from the glovebox and annealed at 120 °C in an oven overnight. After cycling, the sample was brought back into the glovebox for disassembly. The pouch material was removed and a 1/8 inch diameter punch was used to cut out only the central portion of the sample. This 1/8 inch diameter portion of the sample was vacuum sealed in pouch material and removed from the glovebox for imaging. This procedure was used to make samples A, B, C and D.

5.2.3 Sample preparation for in situ, stop-motion X-ray microtomography imaging

A 1/2 inch diameter metal punch was used to cut a polymer electrolyte disc from the previously cast electrolyte film. Three layers of lithium metal foil were stacked on top of a piece of nickel foil. The lithium electrodes were made by using a 7/16 inch punch to punch through the three layers of lithium and nickel foil backing. The thick lithium metal electrodes are necessary to prevent artifacts from the highly X-ray absorbing nickel foil from obscuring features near the lithium/electrolyte interface. The lithium was backed with nickel foil because most other metals, including aluminum, are known to react with lithium metal. The two, 450 μm thick lithium electrodes were used to sandwich the polymer electrolyte membrane. A 0.57 mm stainless steel shim was placed beneath the cell and a 0.35 mm shim was placed above the cell to keep it flat. Aluminum current collector tabs were then affixed to the stainless steel shims and the sample was vacuum sealed in pouch material. This procedure was used to make sample E.

The aluminum current collectors were relatively X-ray transparent, so the 22 keV X-ray beam was able to transmit through the current collectors and pouch material to reveal features at the lithium/electrolyte interface. The bottom stainless steel shim was thicker than the top shim so that the lithium/electrolyte interfaces are raised above the plane where the pouch material was sealed. This feature is needed to obtain clear reconstructed volumes as the sealing material through which the X-ray beam travels is minimized. An aluminum grid was placed on top of the pouch to help aid in identifying the positions where lithium globules were growing into the electrolyte. Once these positions were identified, they were marked and a higher magnification lens with a smaller field of view was used to image these positions.

The cell described above was used for in situ X-ray tomography experiments wherein charge was passed during imaging. In this study however, we focus on the growth of lithium globules through block copolymer electrolytes, a process that occurs on the time-scale of days. Due to limited access to the X-ray tomography beamline, we present results from stop-motion experiments wherein cells were cycled prior to beamtime, imaged, and returned to the cycling apparatus.

5.2.4 Cycling procedure for post mortem samples

The sample shown in Figure 5.1a was imaged shortly after assembly and was never cycled. The sample shown in Figure 5.1b and 5.2b and d was cycled on a VMP3 potentiostat test system in a 90 °C oven using the following routine. First a 0.175 mA/cm^2 of current for four hours followed by a 45 minute rest. Next a -0.175 mA/cm^2 current was passed through the cell for four hours followed by a 45 minute rest. This routine was repeated until the sample failed by short-circuit. The sample shown in Figure 5.2a and 5.2c was cycled using the above routine 15 times, then charge was passed in only one direction for 47 hours when it failed by short-circuit.

5.2.5 Cycling procedure for in situ sample

The sample for in situ imaging was initially cycled 17 times using the previously described cycling routine. After these preliminary cycles, the sample was imaged using X-ray microtomography. Charge was then passed in a single direction at a current density of 0.175 mA/cm^2 for 4.5 hours. The sample was then removed from the oven and brought to the beamline for imaging. This was repeated until reconstructed volumes were collected at fourteen time points. At this point, charge was allowed to pass in the same direction for 31 hours before imaging. Since the sample still had not failed by short-circuit, charge was allowed to pass through the sample for another 114 hours when it finally failed. The sample was then brought back to the beamline for final imaging. Reconstructed volumes were collected at sixteen total time points.

The in situ experiment that we focus on in this paper was carried out over a period of 16 months. There were several months over which the sample was at rest at room temperature in the laboratory. The measured voltage across the sample varied by as much as 0.05 V after prolonged rest periods, or when the cycling equipment was changed, or the sample was repaired (for instance when the tabs broke in the middle of our study and the sample was repouched). We do not know what caused this; typical uncertainties in measured voltage of different cycling equipment available in our laboratory is 0.02 V.

5.2.6 X-ray microtomography imaging parameters and procedure

At the beamline, the stop-motion samples were imaged using an X-ray energy of 22 keV. Lenses with magnifications corresponding to image pixel sizes of 3.2 μm and 1.3 μm were used to image the sample. The lower magnification lens provided a larger field of view. Once the lithium globules began to grow, the higher magnification lens was used to image smaller regions of the sample. A table showing the beam current, beam energy, exposure time, and other scanning parameters for each image in the stop-motion sequence is given in Supplementary Table 1. The ex situ samples were imaged at 20 keV using an exposure time of 350 ms. Under these conditions, the sample was exposed to approximately 43 kGy of radiation per scan (1 Gy = 1 J/kg) [68]. No change in voltage response, cycling behavior, or microstructure was observed in irradiated samples even after repeated scans. However, radiation damage from X-ray microtomography imaging has been reported in hydrated polymer electrolytes used for fuel cell experiments and in bone fracture toughness experiments [66-68]. The damage is thought to stem from the release of free radicals via the radiolysis of water that induce degradation in the polymer. Because our samples are dry, they are likely more stable to radiation.

5.2.7 SEM and FIB

After cycling and X-ray imaging, the samples were brought back into the glovebox for disassembly. The pouch material was removed and the samples were submerged in a 10:1 solution of anhydrous benzene and anhydrous tetrahydrofuran heated at 40 °C and stirred at 300 rpm for 10 hours to dissolve the polymer electrolyte. At this point, tweezers were used to gently pull the two electrodes apart. Much of the polymer electrolyte remained stuck to the lithium electrodes. The samples were removed from the solution and allowed to dry under vacuum in an antechamber for a few minutes. The samples were then transferred to the SEM in a dessicator. The samples were exposed to air for less than 20 seconds upon transferring them from the desiccator to the SEM vacuum chamber. The samples were imaged using 10 keV electrons and a beam current of 10 μA. A 20000 pA gallium ion beam was used to mill a trench through a lithium globule. After milling

out a large enough area to see the globule cross-section, a 3000 pA gallium ion beam was used to polish the cross-section.

5.3 Results and Discussion

Cell name	Sample architecture	Cycling history	Imaging history	Figure
Cell A	Ex situ	Uncycled	X-ray microtomography	5.1a
Cell B	Ex situ	Cycled	X-ray microtomography	5.1b, 5.2b, 5.2d
Cell C	Ex situ	Cycled	SEM, FIB	5.5
Cell D	Ex situ	Polarized	X-ray microtomography	5.1c, 5.2a, 5.2c
Cell E	In situ	Polarized	X-ray microtomography, SEM, FIB	5.3, 5.4, 5.6, 5.7, 5.8, 5.9

Table 5.1 The electrochemical treatment and imaging history of the samples discussed in this study.

This paper is based on five cells that we label A, B, C, D and E. The experiments performed on these cells are summarized in Table 1. We begin by describing the results of ex situ cycling. Our main objective is to study the growth of lithium globules in cells that were polarized by the application of dc current passed primarily in one direction (cells D and E). For simplicity, we refer to these as polarized cells. The digital cross section slices through reconstructed X-ray volumes of cells A, B, and D shown in Figure 5.1 are representative examples of cross sections through uncycled, cycled, and polarized cells. The uncycled cell is devoid of any noteworthy features (Figure 5.1a). Structures comprising several agglomerated globules of lithium appear in cycled cells (Figure 5.1b). We refer to these structures as multi-globular structures. The dark regions of the globular structure are lithium globules surrounded by a sac that we tentatively call the "electrolyte sac." The reason for this term will be clarified shortly. Samples that have failed by short-circuit typically contain one globular structure like the one shown in Figure 5.1b that spans the electrolyte (and several others that do not span the electrolyte). All globular structures exhibit impurity particles that lie at the base. The formation of a globule on one electrode does not appear to stimulate the growth of a globule from the opposite electrode in a position directly across the electrolyte. The occurrence of two globules growing toward each other from both electrodes is rare. The morphology of globular structures described above are consistent with previous publications [109,163]. In Figure 5.1c we show an X-ray tomography digital slice through a polarized cell (cell D). Here we see one globule with an electrolyte sac and an impurity at the base. The thickness of the lithium layer transported across the electrolyte is 40 um for cell D. While this results in undulatory lithium/electrolyte interfaces, the macroscopic distance between the lithium electrodes is more or less constant at all points except those in the vicinity of the globular structure. The characteristic length scale of the undulations is about 300 – 400 μm, and the lithium/electrolyte interface is convex on the deposition side and concave on the stripping side. Notably, in both cycled and polarized cells (Figures 5.1b and 5.1c) a large portion of the electrolyte layer thickness is identical to that in the uncycled cell (Figure 5.1a). In cycled cells, 0.2 % of the lithium/electrolyte interface is occupied by multi-globular structures, while in polarized cells 0.5 % of the interface is occupied by the structures. These values were obtained by examining xy slices through the lithium/electrolyte interfaces (eg. Figures 5.2c and 5.2d).

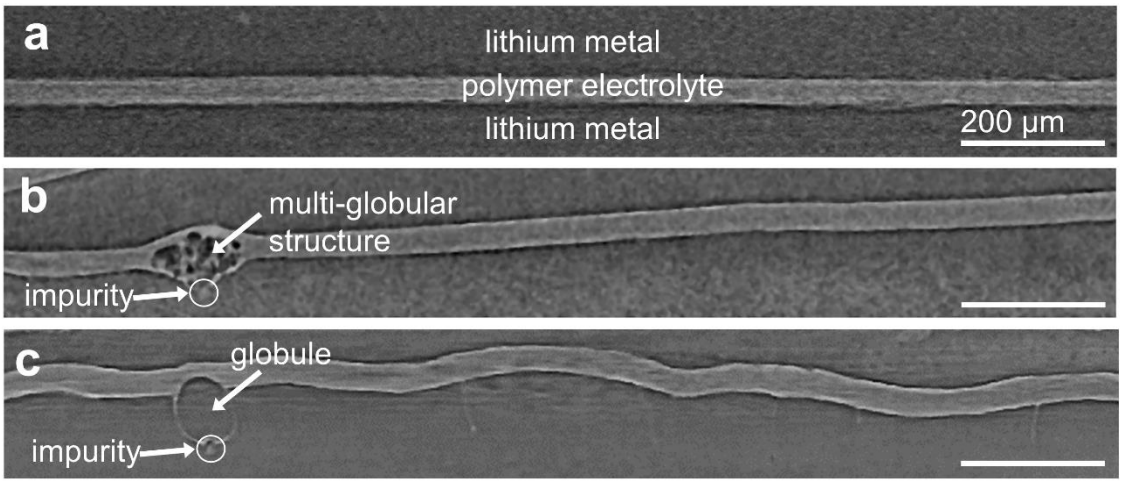

Figure 5.1 **Cross-section slices through reconstructed X-ray tomograms of a lithium metal, polymer electrolyte, lithium metal symmetric cell**. **a** Before the passage of current, the polymer electrolyte film is an unbroken membrane separating the two lithium metal electrodes. **b** After cycling, lithium-filled multi-globular structures form in the polymer electrolyte. **c** When lithium is passed in one direction, from the top to the bottom electrode, structures containing a single globule form. Additionally, ripples form as lithium is deposited unevenly on the bottom electrode.

In the literature, structures that short cells with lithium metal electrodes are assumed to be dendritic [9,75]. In many studies, images of dendritic structures have been presented [26,88]. The structures obtained in our study bear no resemblance to classical dendritic structures which have sharp tips and are highly branched [34]. In contrast, the globular structures obtained in our study are blunt and not branched. We therefore do not use the term dendrite to describe the globular structures observed in this study.

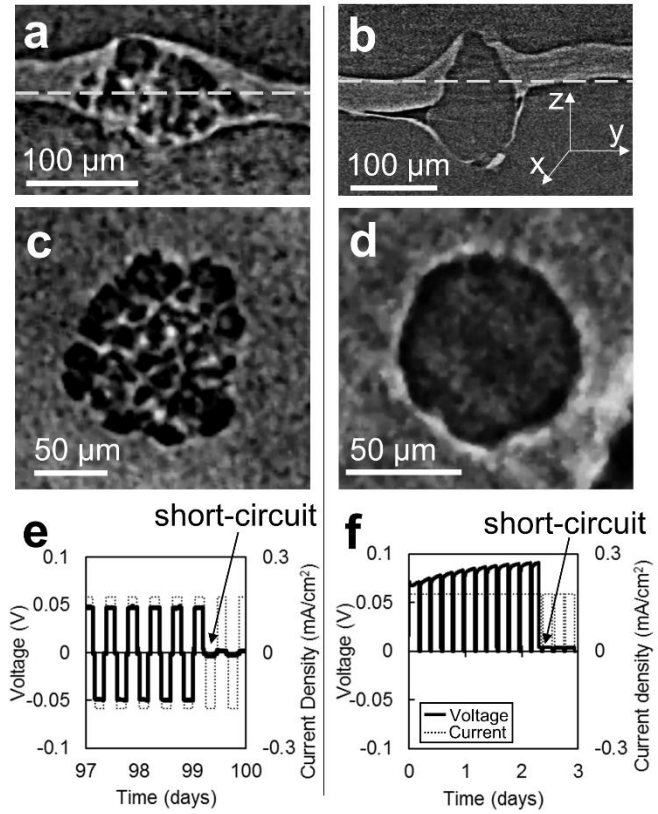

Figure 5.2 **a-d** X-ray tomograms showing globular structures short-circuiting the cell. **a** A side-view image of a structure grown after passing ionic current in both directions as shown in part **e**. **b** Slices of a structure grown by passing ionic current in one direction as shown in part **f**. **c** A top-view of the same structure shown in part **a**. **d** A top view of the same structure shown in part **b**. **e** The charging routine used to form the multi-globular morphology shown in parts **a** and **c**. **f** The charging routine used to form the globular morphology shown in parts **b** and **d**.

Figure 5.2 shows a close-up image of the globular structures formed in cycled (Figures 5.2a and 2c) and polarized (Figures 5.2b and 5.2d) cells. Figures 5.2a and b show cross sectional, digital slices through the yz plane. Figure 5.2c and d show cross sectional digital slices through the xy plane at z-values indicated by the yellow dashed line in Figures 5.2a and 5.2b. The cycling profiles used to grow these structures are shown in 5.2e and 5.2f. The structure shown in 5.2a and 5.2c comprises many small lithium globules surrounded by electrolyte sacs that amass to form one large structure that punctures the polymer electrolyte membrane. The structure shown in Figure 5.2b and 5.2d consists of one large lithium globule encased in an electrolyte sac. The bright sac surrounds most of the egg-shaped globule. However, there are regions of the sac that appear broken, allowing for the passage of electronic current through the globule.

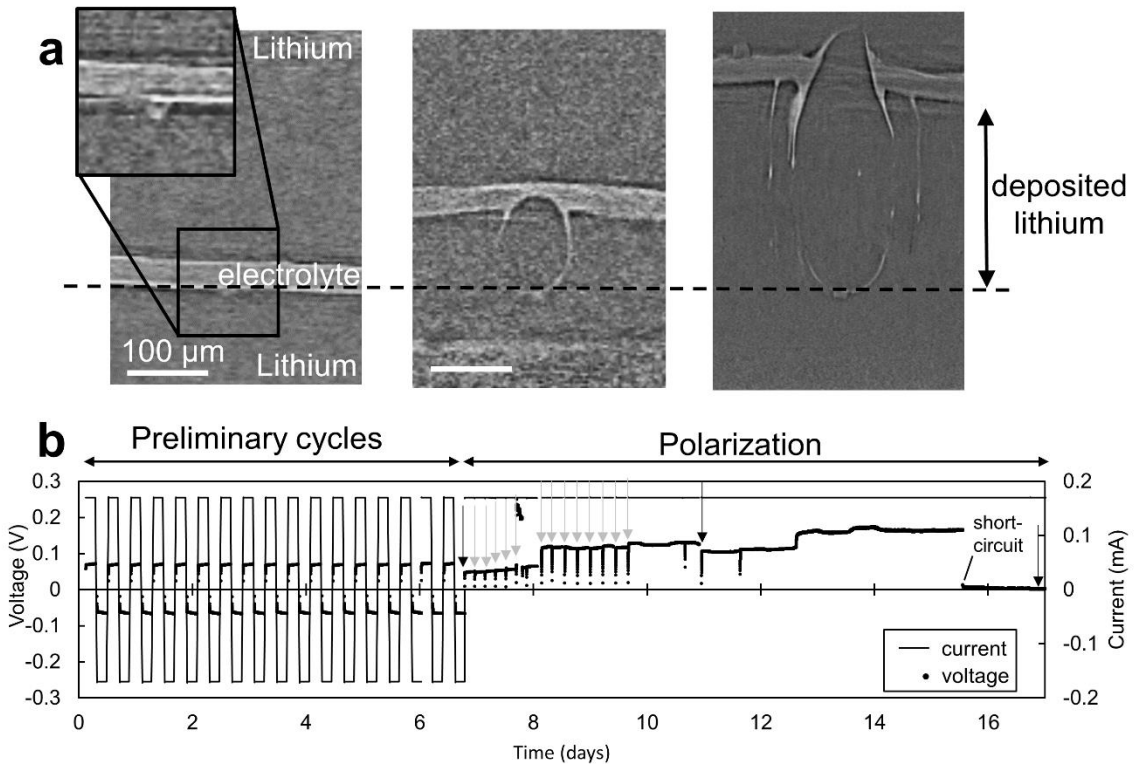

Figure 5.3 **a** A sequence of X-ray microtomography images showing the same location in cell E as a lithium globule grows and eventually punctures the polymer electrolyte membrane. The total amount of lithium transported through the electrolyte before failure by short-circuit corresponds to a 167 µm layer of lithium metal. **b** The cycling profile for cell E. The first image was taken after 17 preliminary cycles. At this time, a lithium globule had not yet begun to form in the position shown above. Times where the polarization was paused for imaging are denoted with an arrow. The three images shown in part **a** correspond to the black arrows. Pauses are not shown for simplicity. The sample failed by short-circuit after about 9 days of active polarization.

The sequence of tomograms shown in Figure 5.3 show the results of an in situ experiment on cell E. These tomograms were obtained from the same location as lithium is stripped from the top electrode and deposited on the bottom electrode. After preliminary cycles, a small impurity particle is seen at the lower lithium/electrolyte interface (Figure 5.3a). As lithium is deposited on the bottom electrode, the polymer electrolyte membrane moves upward. However, a disturbance occurs in the vicinity of the impurity particle and a globular structure like that shown in Figures 5.2b and 5.2d begins to form. Eventually, the structure grows large enough to puncture the electrolyte membrane. In this case, this occurs after a 167 µm layer of lithium is transported through the polymer electrolyte membrane. A sequence of sixteen reconstructed volumes was collected from this sample, but only three are shown for simplicity. The amounts of charge passed through cell E before the tomograms in Figure 5.3a, 5.3b, and 5.3c were obtained are 0, 55, and 124 C/cm^2; we do not count coulombs passed during the preliminary cycling. Note that multiple globules were observed growing in this sample, however this is the only globule that appeared to puncture the electrolyte, causing the sample to fail by short-circuit.

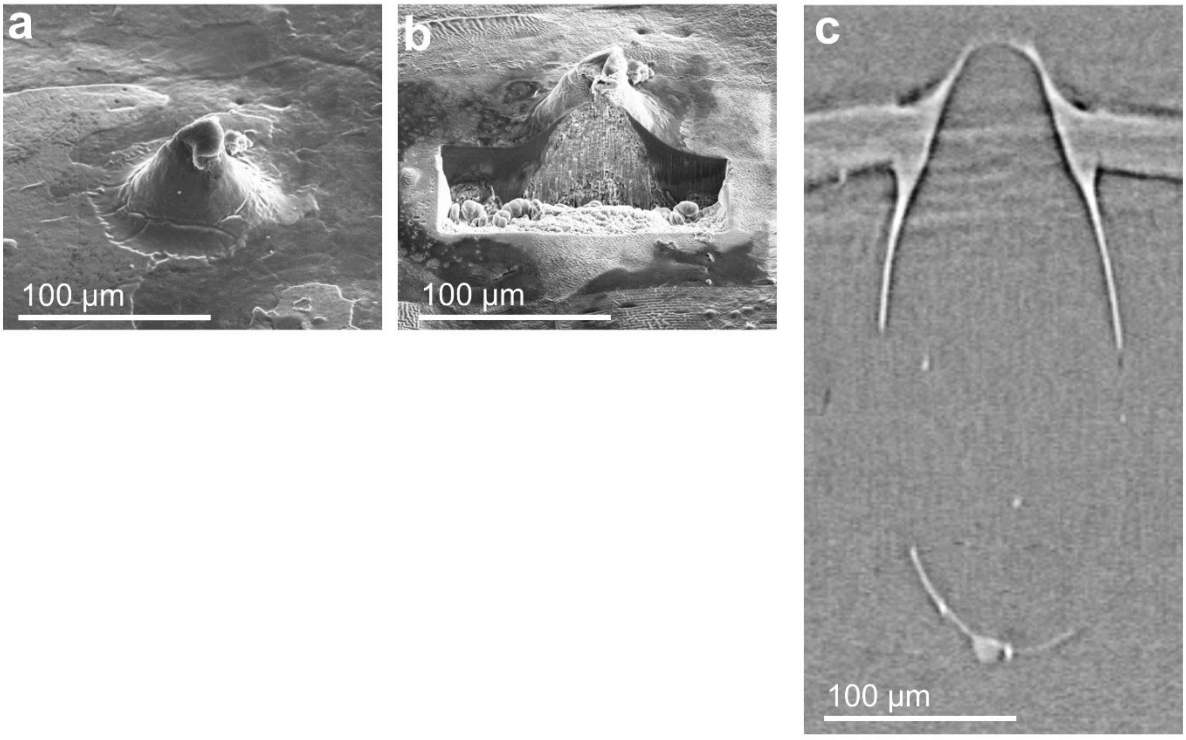

Figure 5.4 **a** An SEM image of the lithium globule shown in Figure 5.3 taken after disassembling the sample. This image is taken at a 52° angle. **b** A focused ion beam was used to mill into the globule revealing its cross-section. This scanning electron micrograph shows the same globule as shown in part **a** after milling. **c** The cross-section X-ray micrograph of the same globule. Only the upper tip of the globule was studied using SEM.

After cell E had shorted, it was disassembled for high-resolution imaging using scanning electron microscopy (SEM). Immersing the cell in 10:1 benzene to THF mixture separated the top electrode from the polymer and bottom electrode. An image of the surface of the polymer stuck to the bottom electrode, taken at a 52° angle from normal, is shown in Figure 5.4a. This image shows a portion of the globule that protrudes into the space originally occupied by the top electrode. When the two electrodes were pulled apart, the globular structures remained lodged in the electrode where lithium was deposited. The position where the globule broke away from the top electrode is visible in the SEM micrographs (Figure 5.4a). A focused ion beam (FIB) was used to mill a trench through the globule shown in 4a. The SEM image shown in 4b is of the same globule shown in Figure 5.4a after FIB milling. The cross-section of the globule is revealed and matches that of the cross-sectional image taken using X-ray microtomography shown in Figure 5.4c. In Figure 5.4b, the large dome-like structure in the middle of the image is the lithium globule while the polymer electrolyte dominates the remainder of the image. Most of the globule is hidden within the bottom lithium electrode and is too deep to expose via FIB milling.

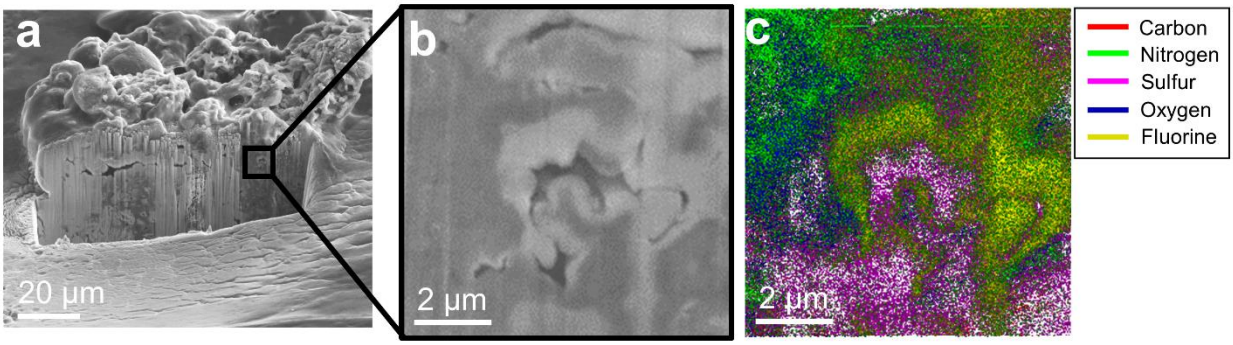

Figure 5.5 **a** An SEM image taken at a 52° angle of the cross-section of a multi-globular structure in cell 5 after milling with a FIB. **b** A blown up image of the region where energy dispersive spectroscopy was used to map the elements. **c** A map of the elements detected using energy dispersive spectroscopy. The absence of signal is interpreted to be lithium metal. The interior of the structure consists of lithium metal regions and regions containing elements from the electrolyte. These elements appear as the bright, X-ray absorbing electrolyte sacs surrounding lithium globules in X-ray microtomography images.

Figure 5.5a shows an SEM image of the cross-section of a globule in cell C (a cycled ex situ cell) milled using the FIB. Figure 5.5b shows a magnified view of the interior of a structure that contains multiple globules. The results of elemental mapping on the micrograph shown in Figure 5.5b are shown in Figure 5.5c. It should be noted that the sample could be imaged with the SEM and analyzed with EDS after FIB milling without removing the sample from the vacuum chamber. Figure 5.5c is dominated by two regions: a colored region that contains elements found in the electrolyte and a white region where no signal is detected which we assume represents lithium metal. The EDS system used for these experiments was not capable of resolving lithium because of the low energy of the Li Kα X-rays. It is evident that the electrolyte is trapped within the interior of the multi-globular structure obtained during cycling. The extent to which the electrolyte trapped within this structure is degraded is not clear. The length-scales seen in Figure 5.5b and 5.5c are consistent with the length-scales of the globules and sacs seen in the X-ray tomograms (Figures 5.1b, 5.2a, 5.2c). We have thus established that the lithium globules in multi-globular structures are surrounded by electrolyte sacs.

The brightness of the features seen in the X-ray tomograms corresponds to the amount of X-rays absorbed by the elements contained in that feature. Since the electrolyte contains elements that are heavier than lithium, one would expect for the sacs surrounding the lithium globules to absorb more X-rays. This is consistent with the results shown in Figure 5.5.

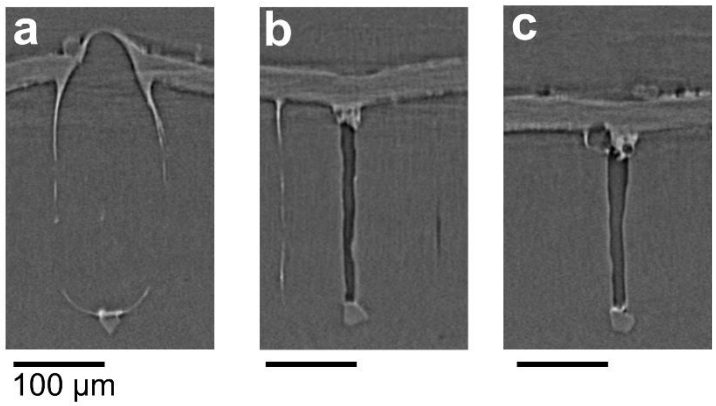

Figure 5.6 **Morphology of defects in the deposited lithium electrode**. Faceted impurity particles are located at the base of all defects. a A lithium globule. B A void. C A void with a globule on the top.

Having focused thus far on the globular structures, we turn our attention to the impurity particles. Other structures, in addition to the lithium globules, formed on top of impurity particles that were initially located at the lithium/electrolyte interface. In Figure 5.6, we show examples of such structures seen in cell E at the end of the experiment (charge passed = 124 C/cm^2). A different globule from the one discussed previously is shown in Figure 5.6a. A faceted impurity particle is located at the base of the globule. Figure 5.6b shows a large void formed on top of the impurity particle. At the top of the void we see the beginnings of a lithium globule and another phase that appears to be degraded electrolyte. Note that after preliminary cycling, charge was passed in only one direction, so this void was formed by the lack of lithium deposition on the impurity particle rather than preferential stripping. Figure 5.6c shows a different void formed on top of a faceted impurity particle. In this case, there is no evidence of a globular lithium structure forming on the void. To the left of the void we see a thin polymer streak. We show below that this occurs at grain boundaries. The prevalence of voids and globules that form on impurity particles is approximately equal (55 % globules and 45 % voids in cell E).

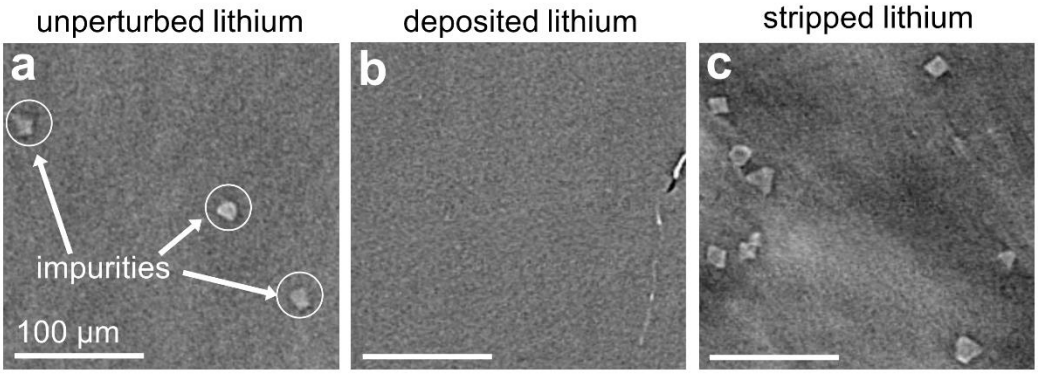

Figure 5.7 **Reconstructed X-ray tomography slices**. **a** Unperturbed lithium metal. Bright impurity particles are embedded in the lithium foil. **b** Electrochemically reduced lithium electrode devoid of visible impurity particles. The feature on the right is a grain boundary. Slice obtained 50 µm from the lithium/electrolyte interface. **c** Electrochemically oxidized

lithium electrode showing a high concentration of impurity particles. Slice obtained 10 µm from the lithium/electrolyte interface.

As lithium is stripped from the top electrode and deposited on the bottom electrode, the relative concentration of impurity particles changes. This is illustrated in Figure 5.7 where three slices through cell E (charge passed = 124 C/cm^2) are presented. Figure 5.7a shows a slice through an unperturbed region of lithium foil. We obtained this slice from the stripped electrode at a location 150 µm away from the lithium/electrolyte interface. The slice in Figure 5.7a shows a relatively low concentration of faceted impurity particles. The particles are octahedral in shape and are generally about 20 µm from tip to tip. These particles are circled for clarity. Figure 5.7b shows a slice through the deposited lithium layer (50 µm from lithium/electrolyte interface). We see no evidence of impurity particles in this slice. The feature on the right of the image is polymer trapped in a grain boundary. There were many slices of this size that were devoid of any features. Figure 5.7c shows a slice 10 µm above the lithium/electrolyte interface on the stripped electrode. Here we see a high concentration of faceted impurity particles. The approximate concentration of impurity particles in unperturbed lithium foil is 880 particles/mm^3. After electrochemical stripping, the impurity concentration increases sharply to 2400 particles/mm^3 at the lithium/electrolyte interface. Notably, there are no impurities present in the layer of deposited lithium metal. Therefore, it is evident that the impurity particles are left behind as lithium is stripped from the electrode.

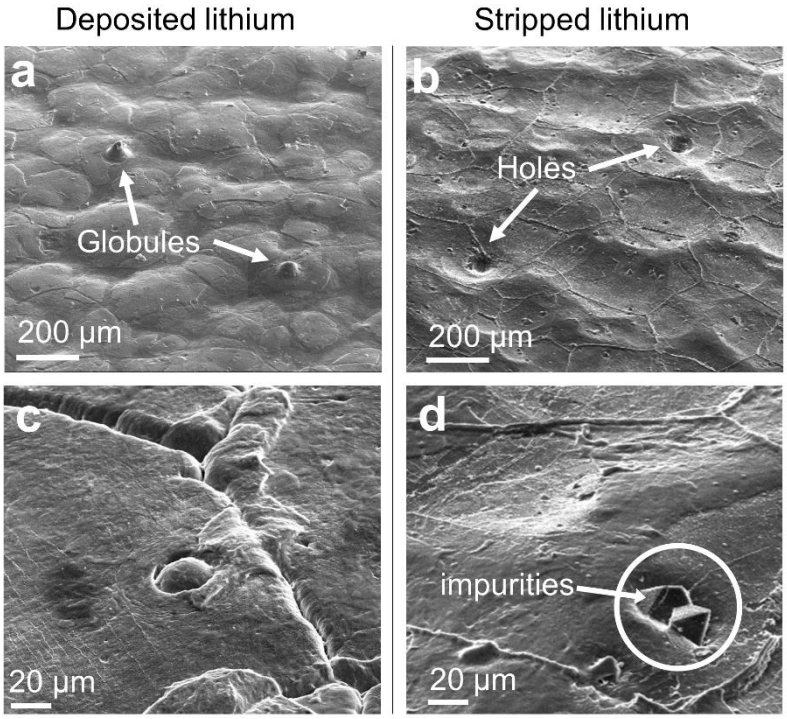

Figure 5.8 **a** An SEM image of the electrochemically reduced electrode covered with polymer electrolyte. The surface shows convex rippling. Two lithium globules are seen pushing through the polymer electrolyte. **b** An SEM image of the electrochemically oxidized electrode shows the corresponding impressions of the lithium globules as they pushed through the electrolyte. **c** Higher magnification SEM images of the deposited

lithium without an electrolyte cover shows grooving at the lithium grain boundaries. **d** Impurity particles and grain boundary protrusions are visible on the higher magnification SEM image of the stripped lithium surface. All images are taken at a 52° angle.

The SEM images shown in Figure 5.8a and b show the surface morphology of the two electrodes from in situ, polarized cell E. The regions shown here faced each other in the cell prior to disassembly. Figure 5.8a shows the bottom electrode, where lithium was deposited, after disassembly. This electrode is partially blanketed with the polymer electrolyte in spite of the fact that the cell was soaked in a solvent that dissolves the block copolymer electrolyte. The entire region shown in Figure 5.8a is blanketed with polymer, but there were other regions that were not blanketed. The tips of two globules are observed pushing through the electrolyte film. Convex ripples are observed on this electrode. Figure 5.8b shows the top lithium electrode where lithium was stripped. Two indentations are seen in the top electrode corresponding to the positions where the tips of the lithium globules pressed up into the electrode. Concave ripples are seen on the surface of the stripped electrode. The stripped electrode appears to be an impression of the deposited electrode.

Figure 5.8c and 5.8d show higher magnification images of the deposited and stripped electrodes of cell E. Figure 5.8c shows a region of the deposited electrode that was not blanketed by polymer electrolyte. The tip of a small globule can be seen in the center of the image. Grain boundary grooving is observed on this electrode indicating that lithium reduction at grain boundaries is slower than that on the crystal faces. Figure 5.8d shows the surface of the stripped electrode. The grain boundaries protrude from this electrode surface, indicating that lithium is more readily oxidized from the crystal faces. The locations of the grain boundaries on the two electrodes are not correlated. The stripped electrode is littered with faceted impurity particles. Regions of the deposited electrode that were not blanketed by polymer showed no evidence of faceted impurities. Regions of the deposited electrode that were blanketed by polymer showed a few faceted particles. It is likely that these particles stuck to the polymer as the two electrodes were separated.

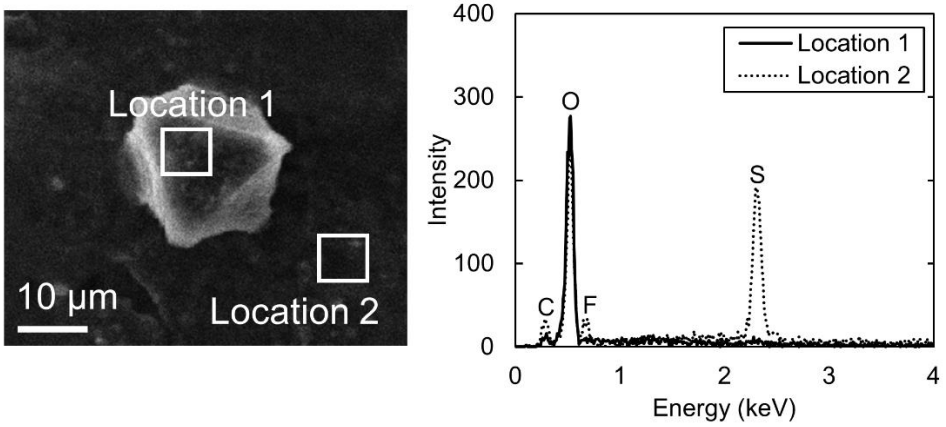

Figure 5.9 Energy dispersive spectroscopy was used to identify the elements in an impurity particle stuck to the polymer electrolyte. The spectra for location 1 shows a large peak in intensity at an energy that corresponds to the oxygen K-edge. Location 2 shows peaks corresponding to the K-edges of carbon, oxygen, fluorine, and sulfur.

Figure 5.9 shows energy dispersive spectroscopy (EDS) data from an impurity particle that was stuck to the polymer electrolyte in cell E. Spectra were collected for two locations within the sample. The first location is on top of the faceted impurity particle. This location shows a large intensity peak at 0.53 keV, associated with the oxygen K-edge. No other elements are detected in this region. The second location is on the polymer electrolyte film. The spectra collected at this location shows intensity peaks at energies that correspond to carbon, oxygen, fluorine, and sulfur. These elements are all components of the polymer electrolyte. The beam energy for these measurements was 15 keV. Generally, signal is obtained from elements in the top few micrometers of the region examined using EDS. Light elements like hydrogen, helium, and lithium are undetectable. Based on the spectra collected at location 1, the identity of the impurity particle is likely either lithium oxide (Li_2O) or lithium hydroxide (LiOH). Lithium oxide assumes an antifluorite crystal structure that tends to exhibit octahedral cleavage planes, consistent with the faceted shape of the impurity particles seen in this study. Further work is needed to systematically characterize the impurity particles.

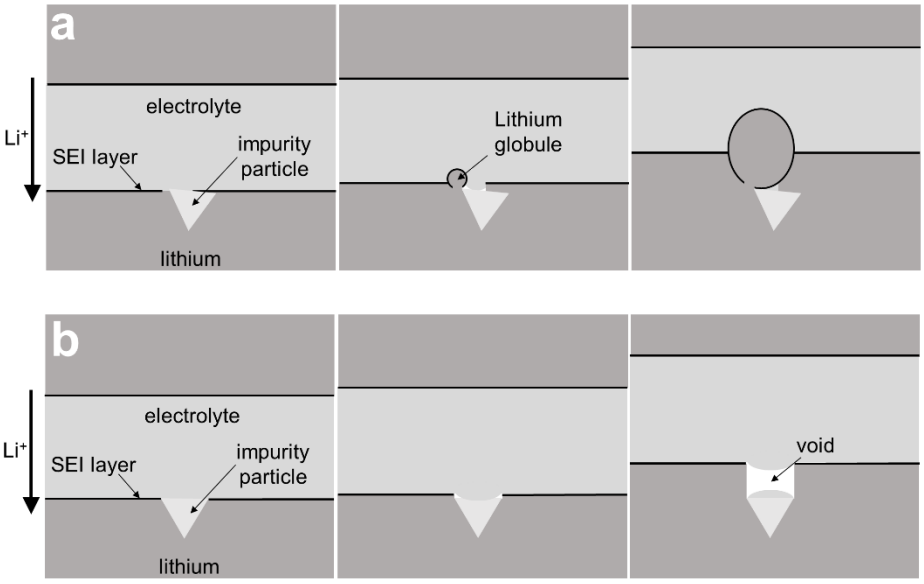

Figure 5.10 A schematic showing a proposed mechanism for the nucleation and growth of **a** lithium globule, and **b** formation of voids.

One hypothesis for the irregular deposition of lithium at these impurity particles is that the insulating nature of the particles prevent the reduction of lithium metal directly on top of the impurity due to the lack of access to electrons. Mechanisms by which this may result in the formation of globules and voids are presented schematically in Figure 5.10. We assume the presence of a stabilizing solid electrolyte interface (SEI) layer between lithium metal and our electrolyte. The SEI layer is too thin for detection by X-ray microtomography. We posit that the SEI is interrupted at the edges of the impurity particle. This could lead to preferential lithium deposition at the corner of the impurity particle as shown in Figure 5.10a due to an increase in local conductivity or concentration of electric field lines. On the other hand, a void may be generated on top of the impurity as shown in Figure 5.10b. The corresponding tomograms through the voids (Figures 5.6b and 5.6c) show a bright phase at the top of the void. We propose that this is degraded polymer electrolyte with excess salt. Presumably, the polymer electrolyte on top of

these particles could be more susceptible to side-reactions. As the lithium/electrolyte interface surrounding the impurity particle moves upward and the impurity particle remains adhered to the electrode at its original location, the degraded polymer separates from the surface of the impurity leaving a void.

Since the block copolymer electrolyte acts like a filter for the lithium metal, one could take advantage of this phenomenon to produce a clean layer of deposited lithium that is free of impurities. Using such a layer in a battery is likely to improve cycle life as we have demonstrated a relationship between the globules that short the cell and the impurities.

5.4 Conclusion

We have used X-ray microtomography and SEM imaging to study lithium deposition and stripping in symmetric lithium-polymer-lithium cells wherein a rigid polystyrene-*b*-poly(ethylene oxide) block copolymer serves as the electrolyte. This enabled identification of lithium structures that caused cell shorting. When charge is passed in one direction, these structures consist of a single lithium globule encased in an electrolyte sac. When charge is passed in both directions, simulating the charge and discharge cycling experienced by full batteries, they consist of many small globules connected together as an agglomerate. In both cases, an impurity particle lies at the base of the structure. It is generally assumed that failure of lithium metal electrodes is due to the formation of dendrites, a highly-branched structure with pointed tips. The globular structures identified in this study are qualitatively different from dendrites; they are unbranched and rounded. Our work suggests that the growth of branched structures is thwarted by rigid electrolytes.

Stop-motion X-ray tomography was used to track the evolution of globules obtained when charge is passed in one direction. The impurity particles are rich in oxygen and electronically insulating. We hypothesize that ionic current is localized at the edge of the particles due to disruption of the SEI layer, resulting in the nucleation and growth of lithium globules. We also observed void formation on top of the particles, consistent with the fact that they are electronically insulating. When lithium is stripped from an electrode, the impurity particles are left behind, resulting in a high concentration of impurities in the oxidized electrode, particularly in the vicinity of the lithium/electrolyte interface. Conversely, the deposited lithium is devoid of visible impurities. Electrolytic refining of lithium metal using a block copolymer electrolyte could be used to prepare clean lithium foils for lithium metal batteries with improved cycle life.

5.5 Acknowledgements

Primary funding for the work was provided by the Electron Microscopy of Soft Matter Program from the Office of Science, Office of Basic Energy Sciences, Materials Sciences and Engineering Division of the U.S. Department of Energy under Contract No. DE-AC02-05CH11231. The FIB and SEM work was performed as a user project at the Molecular Foundry at Lawrence Berkeley National Laboratory, which is supported by the U.S. Department of Energy under Contract # DE-AC02-05CH11231. Hard X-ray microtomography experiments were performed at the Advanced Light Source which is supported by the Director, Office of Science, Office of Basic Energy Sciences, of the U.S. Department of Energy under Contract No. DE-AC02-05CH11231. Katherine J. Harry was supported by a National Science Foundation Graduate Research Fellowship.

5.6 Supplementary Information

Image Number	Ring Current (mA)	Beam energy (keV)	Number of angles	Exposure time (ms)	Rotation angle range
1	500	20	1025	350	180
2	500	20	1025	350	180
3	500	20	1025	450	180
4	500	20	1025	350	180
5	500	20	1025	300	180
6	500	20	1025	300	180
7	500	20	1025	300	180
8	500	20	1025	1000	180
9	35	22	2049	1500	360
10	35	22	2049	1500	360
11	35	22	4097	1500	360
12	35	22	4097	1500	360
13	34	22	4097	1500	360
14	35	22	4097	1500	360
15	33	22	4097	1500	360
16	500	22	2049	600	180

Table 5.S1 X-ray tomography imaging parameters used to obtain images of cell E.

	Tool name	**Detectors**	**Mode**	**Acceleration voltage**
Figure 5.4	FEI Strata 235 dual beam FIB	SED	Normal	10 kV
Figure 5.5	FEI Strata 235 dual beam FIB	Image: SED Spectra: EDAX 32	Image: Normal Spectra: EDX	Image: 10 kV Spectra: 20 kV
Figure 5.8	FEI Strata 235 dual beam FIB	SED	Normal	10 kV
Figure 5.9	JEOL JSM-7500F	Image: SEI Spectra: NanoTrace EDS	Image: Normal Spectra: EDX	Image: 15 kV Spectra: 15 kV

Table 5.S2 Imaging, elemental analysis, and FIB milling parameters used to collect SEM images and EDS spectra shown in figures 5.4, 5.5, 5.8 and 5.9.

Chapter 6 – Influence of electrolyte modulus on the local current density at a dendrite tip on a lithium metal electrode

ABSTRACT

Understanding and controlling the electrochemical deposition of lithium is imperative for the safe use of rechargeable batteries with a lithium metal anode. Solid block copolymer electrolyte membranes are known to enhance the stability of lithium metal anodes by mechanically suppressing the formation of lithium dendrites during battery charging. Time-resolved hard X-ray microtomography was used to monitor the internal structure of a symmetric lithium-polymer cell during galvanostatic polarization. The microtomography images were used to determine the local rate of lithium deposition, i.e. local current density, in the vicinity of a dendrite growing through the electrolyte. Measurements of electrolyte displacement enabled estimation of local stresses in the electrolyte. At early times, the current density was maximized at the dendrite tip, as expected from simple current distribution arguments. At later times, the current density was maximized at the dendrite perimeter. We show that this phenomenon is related to the local stress fields that arise as the electrolyte is deformed. The local current density, normalized for the radius of curvature, decreases with increasing compressive stresses at the lithium-polymer interface. To our knowledge, our study provides the first direct measurement showing the influence of local mechanical stresses on the deposition kinetics at lithium metal electrodes.

6.1 Introduction

There is increasing interest in the transport of ions at lithium metal electrodes due to the current focus on increasing the energy density of rechargeable lithium batteries [169]. In theory, replacing the graphite electrode with lithium metal will result in a 40% increase in gravimetric energy density [170]. Battery chemistries with energy densities that are substantially larger than that of the lithium-ion chemistry, such as lithium-sulfur and lithium-air, rely on the availability of a rechargeable lithium metal anode. Electrodeposition of metallic films is also an integral step in the manufacture and use of a broad range of devices spanning consumer electronics to energy storage [171-173]. Conventionally, in both batteries and electrochemical processing, metals are electrodeposited from liquid electrolytes [14,174,175]. However, recent advances in polymer and ceramic electrolytes have allowed for the deposition (and stripping) of metals from electrolytes with a high modulus [11,23,176]. These stiff electrolyte materials influence the mechanism of metallic electrodeposition. Notably, stiff polymer electrolytes are known to suppress the growth of dendrites in batteries containing a lithium metal anode [33,163]. Suppressing the growth of metallic dendrites is imperative for the safe and reliable use of high energy density, rechargeable batteries with metallic anodes [8,9].

[†] This chapter was submitted for publication in April 2016.

Numerous experimental studies have addressed the issue of dendrite growth in lithium batteries [14,26,28,31,32,55-57,84,85,177]. While the increase in current density in the vicinity of a dendrite is, perhaps, the most important driving force in the process, this increase has thus far escaped experimental scrutiny. To our knowledge, only the average current density has been reported in previous studies on cells containing lithium metal electrodes. In this study, we use time-resolved X-ray microtomography to quantify the topology of the lithium metal electrode and local current density over the entire electrode of a symmetric lithium-lithium cell with a solid block copolymer electrolyte as a function of charge passed. We naturally focus our attention on regions within the cell in the vicinity of growing dendrites. Our experiments also enable determination of the local strain in the solid polymer electrolyte, which in turn enables estimation of local stress. We present data on the interplay between local stress and lithium deposition in the vicinity of the dendritic tip.

Conventionally, when one models lithium dendrite growth, the projected area, or cross-section, of the dendrite at the interface between the electrode and the electrolyte is assumed to stay constant as it propagates through the electrolyte, like a lengthening needle [41-43]. In the case of dendrite growth through a solid electrolyte, we show that this projected area grows as the dendrite propagates through the electrolyte. This increase in area blunts the tip, significantly slowing the vertical growth rate of the lithium dendrites. Consequently, increasing the electrolyte modulus not only suppresses dendrite growth by slowing deposition kinetics at the dendrite tip, but also results in an increased radius of curvature at the tip, which leads to slower growth through current delocalization.

This paper is part of a series on the study of lithium-lithium cell cycling by X-ray microtomography. After initially detecting the formation of lithium dendrites in cycled cells using ex situ X-ray microscopy, a variety of experiments were performed to determine the influence of parameters like temperature and charging time on the dendrite morphology in cells using a solid block copolymer electrolyte membrane [109,163,178]. Next, cells were designed to fit into the X-ray microtomography beamline for in situ characterization of dendrite growth. A qualitative description of these results was reported previously [170]. The present study seeks to quantify the kinetics of lithium deposition on and near a dendrite as it grows through a solid polymer electrolyte.

6.2 Experimental

Polystyrene-*b*-poly(ethylene oxide) was synthesized by anionic polymerization as described previously [167,168]. The molecular weight of the block copolymer was 240-260 kg/mol with a poly(ethylene oxide) volume fraction of 0.5 and a polydispersity index of 1.26. After its synthesis, the polymer was freeze dried and stored in a glovebox filled with argon where oxygen and water levels were controlled and remained less than 5 ppm.

To prepare an electrolyte membrane, the block copolymer was dissolved in N-Methyl-2-pyrrolidone (NMP) with lithium bis(trifluoromethane)sulfonamide salt (LiTFSI) at a concentration of 0.085 Li^+ to ethylene oxide moieties. The solution was poured onto a flat surface covered with nickel foil and spread into a film using a doctor blade. The film was allowed to dry on the flat surface at 60 °C overnight. At this point, the film was peeled off of the nickel foil with tweezers. The freestanding film was allowed to dry for an additional 24 hours at 90 °C under vacuum in a glovebox antechamber. Once dry, the 30 μm thick freestanding solid polymer electrolyte film was wrapped in nickel foil and stored in a sealed container inside of the glovebox. 99.9% pure lithium

metal foil was purchased from FMC Lithium. The roll of 150 μm thick foil was stored in a desiccator inside of the glovebox.

Symmetric lithium – polymer electrolyte – lithium samples for in situ X-ray microtomography imaging were assembled as follows. First, a 13 mm diameter round metal punch was used to punch out a piece of electrolyte from the freestanding polymer electrolyte film. Three layers of lithium metal foil were stacked on top of each other on a clean piece of nickel foil to create a 450 μm thick lithium electrode backed with nickel foil. A 11 mm diameter round metal punch was used to punch out two lithium electrodes from the stack of lithium on nickel foil. The two lithium electrodes were placed on either side of the polymer electrolyte membrane. A 0.57 mm stainless steel shim was placed on one side of the sample and a 0.35 mm stainless steel shim was placed on the other side of the sample. These shims keep the sample flat, which is important for imaging. Aluminum current collector tabs were placed on either side of the sample and the sample was vacuum sealed in nylon and polypropylene lined aluminum pouch material.

This thick lithium electrode backed with nickel foil is helpful for in situ X-ray microtomography imaging because the lithium creates a region of low X-ray absorption around the lithium-polymer interface. If materials that are highly absorbing of 22 keV X-rays, like nickel or stainless steel, are in the path of the X-ray beam, they tend to cause significant artifacts in the reconstructed volumes, obscuring features of interest at the lithium-polymer interface. The thick lithium electrodes move these highly absorbing materials away from the region of interest, allowing for clear reconstructed volumes. The aluminum tabs are X-ray transparent enough to achieve good quality images even though they do block the path of the beam. The tabs are not contacted directly with the lithium foil because aluminum is known to react with lithium. The stainless steel shims sandwiching the sample are of different thicknesses so that when vacuum sealed, the lithium-polymer interface will sit slightly above the central plane of the sample where excess pouch material from the vacuum seal may add noise to the resulting tomography images. A series of six samples of this type were assembled.

One of the samples was cycled until it failed by short circuit using the following routine. A current of 0.175 mA/cm^2 of lithium was passed for four hours followed by a 45 minute rest. Then, a current of -0.175 mA/cm^2 was passed for four hours following by a 45 minute rest. This cycling routine was repeated until the sample failed by short circuit after 32 cycles. The other five samples were then cycled in the same way but were stopped after 17 cycles. The intention was to get the samples close to failure in order to reduce the beamtime required to see the sample fail by short circuit.

At this stage, one of the five samples was imaged using hard X-ray microtomography then polarized for an additional 4.5 hours. This polarization, where charge was passed in a single direction for 4.5 hours, was repeated fourteen times with X-ray microtomography images taken at each 4.5 hour increment. The sample was then polarized for 31 hours before the next image. Finally, the sample was polarized for an additional 114 hours when it finally failed by short circuit and was imaged. All electrochemical polarization and cycling was done while the sample was maintained at 90 °C in an oven.

The sample was removed from the electrochemical cycling equipment and cooled to room temperature before each imaging session. Imaging was performed at the hard X-ray microtomography beamline at the Advanced Light Source (Beamline 8.3.2). Parameters used to image the sample are tabulated in supplementary Table 1. The largest dendrites were found in the

final reconstructed volumes and were tracked back to the initial image where they had not yet begun to form. The image processing program Avizo was used to measure the dendrite height, volume, and area.

The large reconstructed volumes were cropped to contain only the dendrite that shorted the cell. The sequence of cropped reconstructed volumes were binarized for subsequent analysis in Matlab. The position of the bottom lithium-polymer interface was calculated in Matlab relative to a fixed reference, the bottom of the electrode. The current density, i_{jk}, at a pixel with indices j, k was calculated using the volume of lithium deposited, V_{jk}, at that pixel:

$$i_{jk} = \frac{V_{jk}\rho F}{M_{Li} at}. \tag{1}$$

This calculation assumes that all of the charge deposited on the lithium anode is deposited in the form of lithium metal. SEI formation was assumed to occur during the conditioning cycles.

The tomography data directly yield the displacement on the polymer electrolyte at the electrode interface. These measurements were used to determine local stresses near the growing lithium globule in the following manner. First, because the dendrite is approximately axisymmetric, a smooth, axisymmetric surface was constructed, as described in the Appendix, to approximately represent the interface between the dendrite and electrolyte for each of the imaged states. The smoothed surface was then fit to a parabolic shape so that the slope of the curve at the globule tip was zero, consistent with the tomography images.

For each surface, a cylindrical coordinate system was defined, with the z axis coinciding with the axis of symmetry for the surface. The variable r was defined to be the perpendicular distance to the z axis. Except in the immediate vicinity of the dendrite, the lithium surfaces are approximately parallel planes, so the origin was taken to be the intersection of the z axis with the plane from which the dendrite is growing. The positive z direction was defined as the direction of dendrite growth.

As the system is axisymmetric and the mechanical response of the electrolyte is the phenomenon of interest, it was only necessary to solve for electrolyte displacement within any r-z plane.

The electrolyte regions in the vicinity of dendrites experienced severe displacements. Stresses were computed using a large-deformation formulation. The numerical implementation closely follows parts of the work detailed in a previous paper [179]. An overview of the mathematical formulation for the present model is described below, and additional implementation details are provided in the Supplementary material.

6.2.1 Momentum equation.

As inertia is negligible under the experimental conditions, displacement of the electrolyte is described by the equation of mechanical equilibrium, expressed in the spatial description as:

$$\nabla_{\boldsymbol{x}} \cdot \boldsymbol{\sigma} = 0. \tag{2}$$

The subscript $\boldsymbol{x}$ indicates that differentiation is performed with respect to present positions; in finite-deformation models in which material can experience significant displacement, it is

necessary to clearly define the meaning of position. The Cauchy stress tensor, $\boldsymbol{\sigma}$, is modeled using Hooke's law of linear elasticity:

$$\boldsymbol{\sigma} = \frac{E\,\nu}{(1+\nu)(1-2\nu)}(tr\,\boldsymbol{E})\boldsymbol{I} + \frac{E}{1+\nu}\boldsymbol{E}, \tag{3}$$

where Young's modulus E has been determined from experimental rheological measurements, ν is Poisson's ratio, $\boldsymbol{I}$ is the identity tensor, and $tr\,\boldsymbol{E}$ is the trace of Almansi's strain tensor $\boldsymbol{E}$. The shear modulus for this polymer was previously measured and is about 1×10^6 Pa in the low deformation rate limit.[163] This shear modulus value was converted to the Young's modulus assuming a Poisson's ratio of 0.33. In this finite-deformation model, $\boldsymbol{E}$ may be computed as

$$\boldsymbol{E} = (\boldsymbol{I} - \boldsymbol{F}^{-T}\boldsymbol{F}^{-1})/2, \tag{4}$$

where the deformation gradient $\boldsymbol{F}$ is given by

$$\boldsymbol{F} = \nabla_{\boldsymbol{x}_0}\boldsymbol{x}. \tag{5}$$

The subscript $\boldsymbol{x}_0$ likewise indicates that differentiation is to be performed with respect to initial positions, and $\boldsymbol{x}$ refers to present position of material.

We note that the use of the Hooke's law as a constitutive equation is likely to lead to over-predictions of stresses under large displacements; however, there are presently no available constitutive equations which are specifically tailored to describing this electrolyte material.

6.2.2 Boundary conditions.

The simulated electrolyte region extends in the z direction from one lithium electrode to the other. A simple inspection of the tomography data does not provide all of the required boundary displacement information because the electrolyte region does not contain identifiable markers, so some assumptions must be made. It is assumed that the electrolyte remains firmly attached to both lithium surfaces, so that there is no displacement along the top interface. The displacement along the bottom interface (which includes the interface with the dendrite) is assumed to be in the z direction only. In addition, as this is an axisymmetric system, there is no displacement in the r direction at the axis, and there is zero stress in the axial direction on a control surface coinciding with the axis.

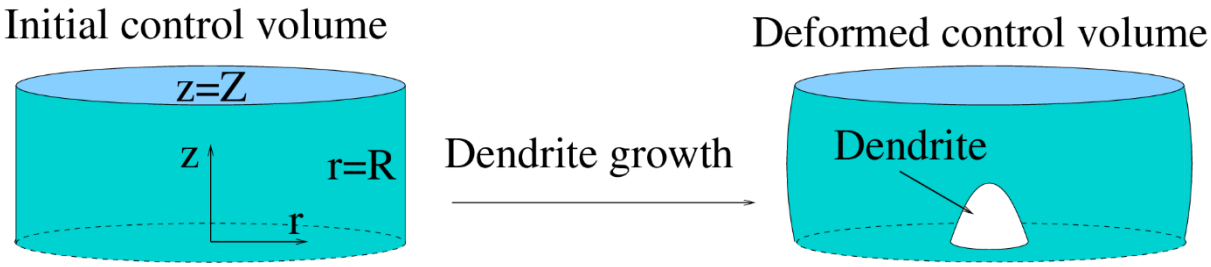

Figure 6.1 Diagram of computational domain in initial and deformed states. The top and bottom surfaces remain stationary, except in the dendrite region. The outer edge of the domain displaces outward to compensate for the intrusion of the dendrite and the limited compressibility of the electrolyte.

At the outer radial surface of the initially cylindrical control volume a simple displacement boundary condition is imposed, as shown in Figure 6.1. The electrolyte is fixed at the top and bottom interfaces, so the outer surface of the initially cylindrical control volume can be described by a curve describing the displacement as a function of z. The true displacement of the outer radial surface could be described in terms of a Fourier sine series. For simplicity, it is assumed that there is no vertical displacement, and that the horizontal displacement of this outer surface (initially at $r = \mathrm{R}$) is given by

$$\Delta \mathrm{R}(z) = A \sin \frac{\pi z}{Z} \tag{6}$$

Figure 6.1 shows a schematic of the computational domain in the initial and the deformed state.

This form uses only the first non-constant term of a Fourier sine series. Here, $z = Z$ is the vertical position of the upper lithium surface. The magnitude A is determined from an estimate of the total volume change experienced by the electrolyte within the control volume, and is calculated by solving the following quadratic equation in A:

$$AZ(8\mathrm{R} + \pi A) = 8\,\pi[1 - \nu] \int_0^R r\, h(r)\, dr. \tag{7}$$

The derivation of this equation is given in the Appendix. A Poisson's ratio of 0.33 and a shear modulus of 1×10^6 Pa was assumed for the polymer electrolyte in these simulations.

In our approach, local current density is calculated from differences between consecutive images while stress is calculated based on an individual image alone. The amount of charge passed before the first of two images used to calculate the current density is reported in the figure legends. For example, when the charge passed is reported as 0 C/cm^2 for a series of current density data, that current density was obtained by analyzing images where the amount of charge deposited prior to the images was 0 C/cm^2 and 8.27 C/cm^2.

6.3 Results and Discussion

Theoretically, the electrolyte modulus should be about twice that of lithium metal to completely suppress lithium dendrite growth [49]. Lithium metal has a room temperature shear modulus of about 4×10^9 Pa [47]. Polystyrene-*b*-poly(ethylene oxide) with a molecular weight of 240-260 kg/mol has a shear modulus that is 2-3 orders of magnitude lower than that at about 10^6 - 10^7 Pa at 90 °C [163]. Poly(ethylene oxide) homopolymer with a molecular weight of 360 kg/mol has a shear modulus of about 10^5 Pa [33]. The ratio of the shear modulus of the electrolyte to lithium metal is approximately 0.0003 for our polystyrene – *b* – poly(ethylene oxide) membrane and 0.00003 for poly(ethylene oxide) homopolymer. Given that these ratios are far less than two, even the stiffened block copolymer electrolyte membrane is far too soft to completely suppress dendrite growth, according to the theoretical models.

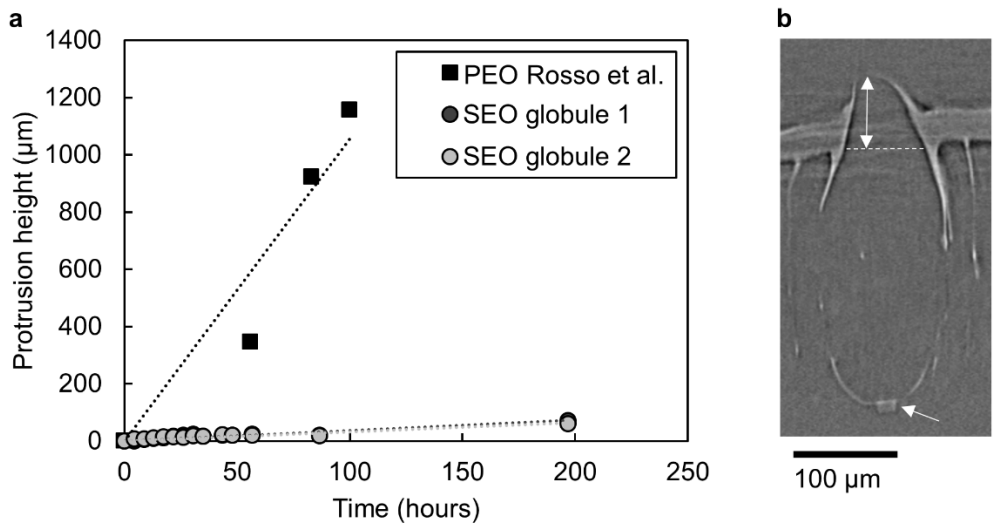

Figure 6.2 **a** The growth rate of the lithium globules through a poly(ethylene oxide) stiffened by copolymerization with polystyrene (SEO) is compared to the growth rate of a lithium dendrite through a traditional poly(ethylene oxide) homopolymer electrolyte as reported by Rosso, M. *et al.* in 2006. The protrusion height is given by the height of the portion of the lithium globule protruding into the polymer electrolyte layer as indicated by the double white arrow in **b**. An impurity particle is visible at the base of the globule as indicated by the lower white arrow. **b** An X-ray tomogram showing globule 2 puncturing an SEO electrolyte membrane. The dark gray phase is lithium metal and the light gray phase is the polymer electrolyte.

Figure 6.2a shows the height of a globular protrusion as a function of time for the two fastest growing lithium globules measured in our study, named globule 1 and globule 2. Figure 6.2b shows an X-ray microtomogram of a lithium globule after it punctured the electrolyte and caused the cell to fail by short-circuit. The dark gray phase in the image is lithium metal while the light gray phase is the polymer electrolyte. An impurity particle is visible at the base of the lithium globule. This particle was initially at the lithium-polymer interface as shown in Figure 6.3. The white arrow indicates the height of the portion of the globule that protrudes into the block copolymer electrolyte and into the top lithium electrode. Additionally, the protrusion height of a dendrite monitored as it grew through 300 kg/mol poly(ethylene oxide) homopolymer in a study performed by Rosso et al. is shown for comparison [31]. In both studies, the applied current density was 0.175 mA/cm^2, and the voltage response was about 0.07 V. The primary difference between the two studies is the sample thickness. In the Rosso study, the electrolyte thickness was 1.2 mm, while the electrolyte thickness in our study is 30 µm.

It is evident from the data shown in Figure 6.2 that the growth rate of the lithium protrusions is significantly slower through the polystyrene reinforced block copolymer electrolyte. The fastest growing lithium globule measured in this experiment protruded into the polystyrene-*b*-poly(ethylene oxide) electrolyte at a rate of 0.37 µm/hr. In the poly(ethylene oxide) homopolymer case, the dendrite grew at a rate of 11 µm/hr, over an order of magnitude faster than in the block copolymer. It is surprising that a relatively small increase in electrolyte modulus had such a large

influence on dendrite growth rate. The following series of figures will help us understand this phenomenon.

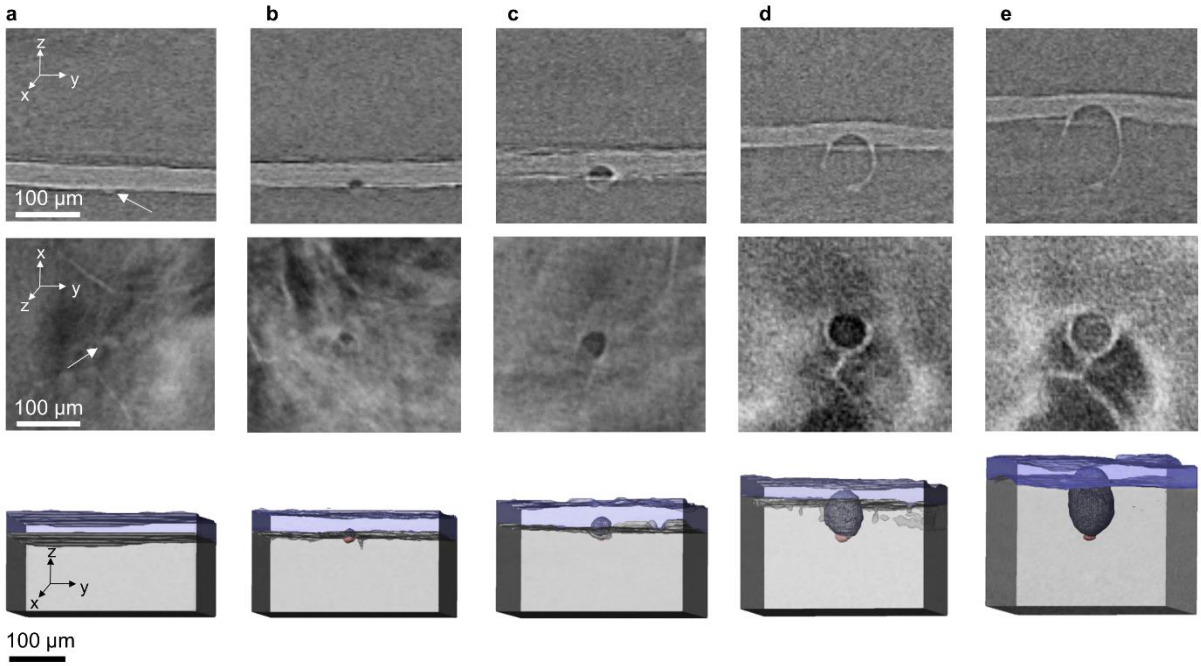

Figure 6.3 Top row: X-ray tomograms of the yz plane in a symmetric lithium – polymer electrolyte – lithium cell showing the growth of a globular lithium dendrite. The dark gray phase is lithium metal and the light gray phase is the polymer electrolyte. The small, light gray spot at the base of the globule is an impurity particle that was initially present in the lithium foil. Middle row: The corresponding xy plane showing the interface between the bottom lithium electrode and the polymer electrolyte. The circular structure in the center of the image is the growing lithium globule. Bottom row: 3D renderings from X-ray microtomography images showing the growth of the lithium globule. The light gray region is the lithium electrode where lithium is deposited. The light blue region is the solid polymer electrolyte membrane. The light red structure at the base of the globule is an impurity particle that was initially in the lithium metal foil. The gray lithium globule is outlined with a wire mesh for clarity. The amount of charge passed before each image is **a** 0 C/cm^2 The white arrows are pointing at the impurity particle that was initially present at the lithium-polymer interface. **b** 8.27 C/cm^2 **c** 16.53 C/cm^2 **d** 35.82 C/cm^2 **e** 54.72 C/cm^2.

Figure 6.3 shows X-ray tomograms and 3D renderings of globule 2 at five stages during its growth through the block copolymer electrolyte. The initial image, shown in part 3a, shows an impurity particle at the lower lithium-polymer interface. The globular structure seen in subsequent images had not yet begun to form. The following images shown in part 3b, 3c, 3d, and 3e show the same location in the sample after 8.27 C/cm^2, 16.53 C/cm^2, 35.82 C/cm^2, and 54.72 C/cm^2 of lithium was deposited on the entire lower lithium electrode, as measured from the potentiostat readings. The top row shows the yz plane through the growing lithium globule. The images are aligned to the bottom of the lithium electrode such that the absolute position of the image is consistent from frame to frame. The polymer electrolyte rises as lithium is stripped from the upper

electrode and deposited on the lower electrode. The impurity particle that was initially at the lithium-polymer interface in Figure 6.3a remains at the base of the lithium globule as it grows. The central row shows the xy plane through the interface between the bottom lithium electrode and the polymer electrolyte for the same lithium globule. Images in the zy, xy, and yz planes are obtained by rendering orthoslices through the stack of reconstructed X-ray microtomography images. The bottom row shows a 3D rendering of the growing lithium globule. The bottom gray layer is the bottom lithium metal electrode in the lithium – polymer – lithium symmetric cell. In the volume renderings, the light blue layer is the block copolymer electrolyte membrane. The top lithium electrode was not included in the rendering for clarity. The dark gray globule forming in the center of the images is filled with lithium. The bottom lithium electrode becomes thicker as lithium is stripped from the top electrode and deposited on the bottom electrode. The lithium globule grows into the electrolyte as the lithium deposits. Eventually, the lithium globule punctures the electrolyte membrane, causing failure by short-circuit.

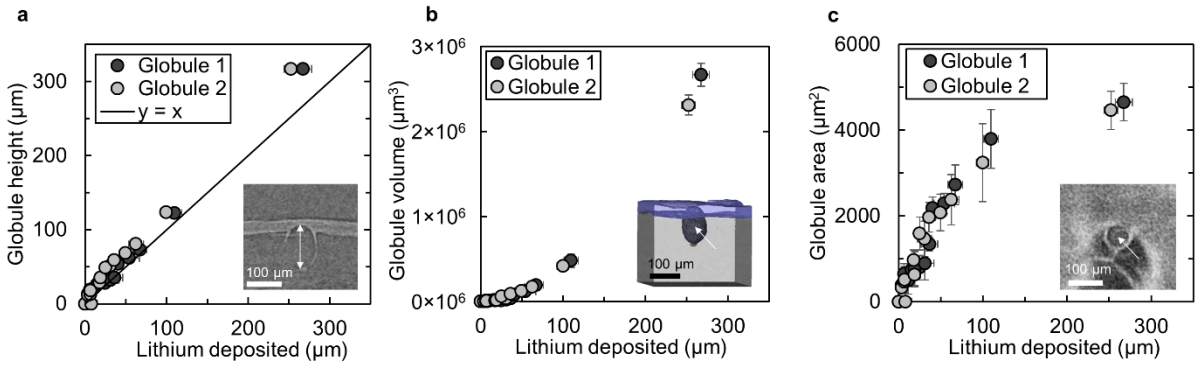

Figure 6.4 The height (**a**), volume (**b**), and area (**c**) of the two fastest growing lithium globules is shown as a function of the amount the lithium deposited. Note that all of these quantities, including the amount of lithium deposited, are directly measured from X-ray microtomography images. The inset images indicate what is defined as the globule height, volume, and area. The difference between the globule height shown in **a** and the y = x line is the height of the globular protrusion into the polymer electrolyte membrane.

Figure 6.4 shows the globule height, volume, and area as a function of the thickness of lithium deposited in the vicinity of the globule, t_{Li}. The abscissa in Figure 6.4 represents the thickness of lithium deposited about 5 – 10 μm from the edge of the globule measured from the X-ray microtomography images. The globule height, measured from the base of the ellipsoidal globule to the tip, increases only slightly faster than the surrounding lithium electrode. Positive deviation from the y = x line in Figure 6.4a corresponds to the height of the globule tip protruding into the electrolyte. The rest of the globule becomes buried by the planar lithium deposition surrounding the globule.

Since the X-ray microtomography images give three-dimensional information about the interior of the sample, one can measure the volume of the globule as a function of the lithium deposited, t_{Li}. The globule volume, V_g, increases quadratically as a function of t_{Li} (the curve in Figure 6.4b represents $V_g = 33t_{Li}^2 + 915t_{Li} - 4437$). One can also measure the area of the dendrite at the planar interface between the bottom lithium electrode and the electrolyte. Curiously, it is evident from Figure 6.4c that the globule grows in area in addition to height. The globule

broadens quickly in the initial stages of growth then begins to level off as it reaches an area of about 4000 - 5000 μm^2.

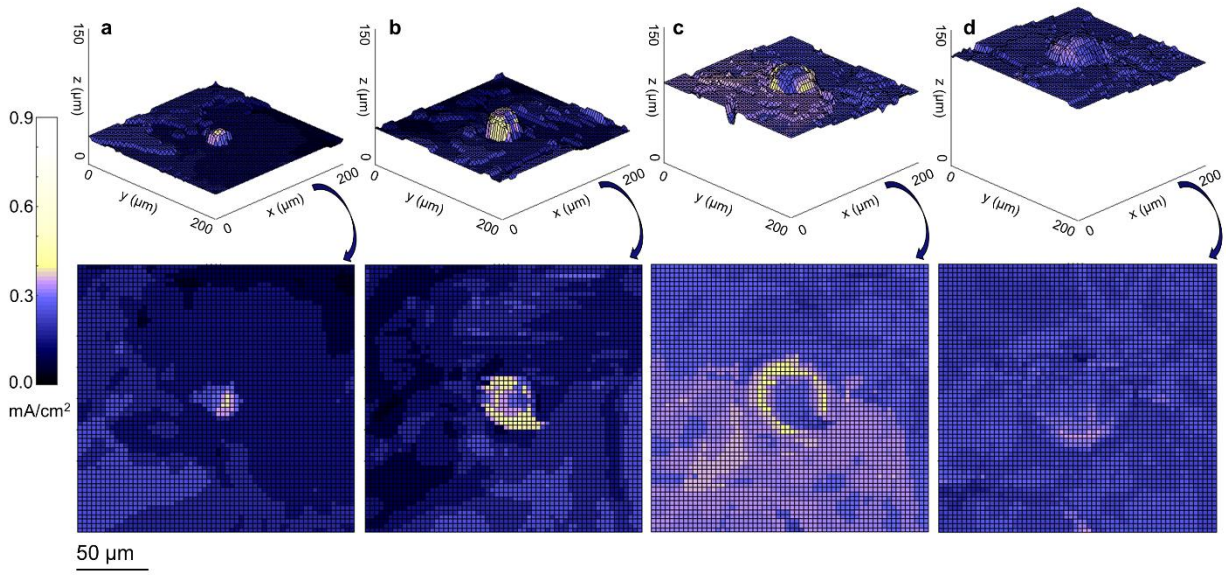

Figure 6.5 Local current density is mapped for four stages during the growth of lithium globule 2. **a** In the initial stages, a perturbation at the lithium/electrolyte interface results in a higher than average current density at the tip of the small globule. This current density is measured between time points 0 C/cm^2 and 8.27 C/cm^2. **b** As the globule grows, the current delocalizes away from the tip of the globule. This map is measured between time points 8.27 C/cm^2 and 16.53 C/cm^2. **c** This delocalization is more pronounced between 16.53 C/cm^2 and 35.82 C/cm^2. **d** As the globule's area gets larger in the late stages of globule growth, the current concentration caused by the globule is greatly reduced. Measured between time points 35.82 C/cm^2 and 54.72 C/cm^2.

Because the X-ray microtomography imaging technique allows one to measure the thickness of lithium deposited at every position on the bottom lithium electrode, one can use Faraday's law to calculate the amount of charge deposited at every point on the lower lithium electrode surface. With two consecutive images, one can map the amount of charge deposited at a given pixel on the lithium surface. Dividing this value by the time interval between images gives the local current density (Equation 1). Figure 6.5 shows current density maps for four distinct stages of growth of lithium globule 2. The maps shown on the top row give the topography of the interface between the bottom lithium electrode and the polymer electrolyte. The tip of the lithium globule is seen in the center of the maps. The color corresponds to the current density. The overall average current density provided by the potentiostat was 0.175 mA/cm^2. A current density of 0 mA/cm^2 appears as black on the color scale, while 0.175 mA/cm^2 appears as a dark blue. Note that when the charge passed is 8.27 C/cm^2 (early stage of dendrite growth) most of the current map is dark blue. This indicates quantitative agreement between local current determined by X-ray microtomography and that applied by the potentiostat.

In Figure 6.5a, the current density is concentrated at the tip of the protruding lithium globule. This current concentration at the protrusion tip is expected based on traditional dendrite growth

theories [42,43]. As the globule grows, however, the current density delocalizes from the protrusion tip to the perimeter. This gives a clear picture of the broadening of the lithium globule. Eventually, the globule becomes wide enough that the current density is only slightly higher on the lithium globule than on the surrounding planar electrode.

We hypothesize that the current delocalization effect shown in Figure 6.5b and 6.5c is caused by the mechanical stiffness of the polymer electrolyte. Since the block copolymer electrolyte is stiff, there is a penalty for a lithium ion reduction event at the globule tip, where the polymer is highly strained. To quantify this effect, we use previously measured moduli values coupled with the X-ray microtomography renderings reported in this study to calculate and map the stress in the polymer [163].

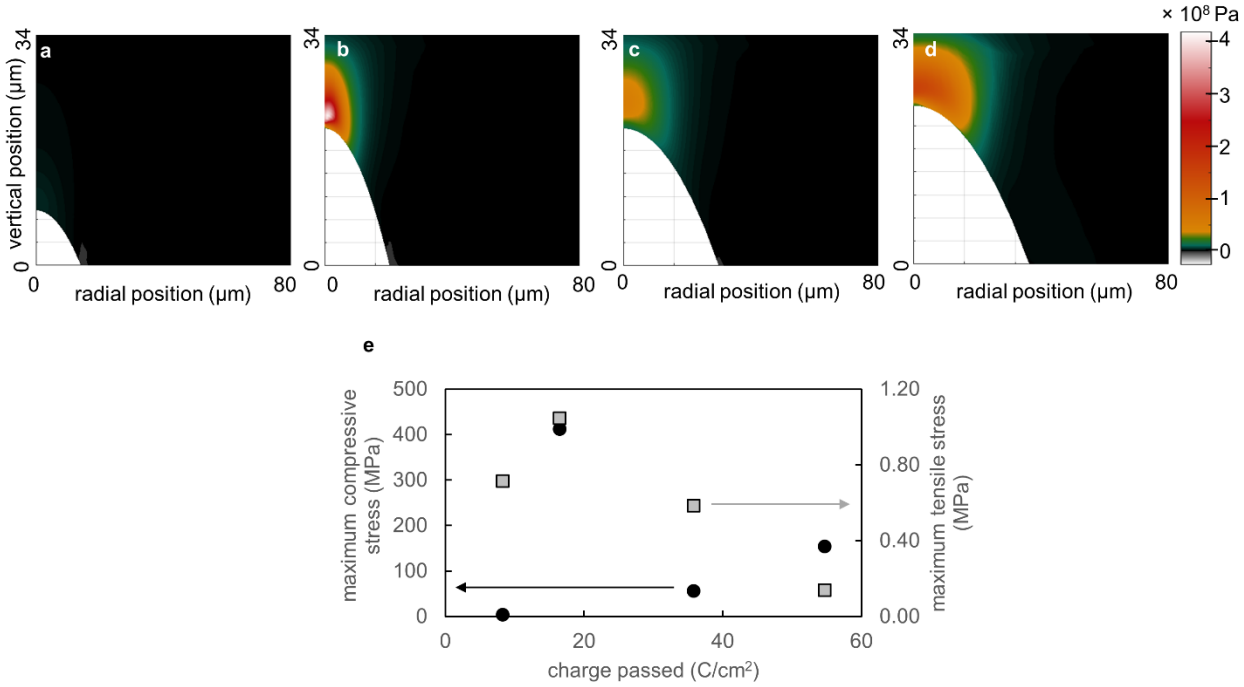

Figure 6.6 **Map of stresses in the polymer electrolyte due to compression from the growing lithium globule**. Stresses are based on an electrolyte modulus of 10^6 Pa. The polymer electrolyte experiences compressive stresses at the tip of the lithium globule and tensile stresses at the perimeter. **a** 8.27 C/cm^2 **b** 16.53 C/cm^2 **c** 35.82 C/cm^2 **d** 54.72 C/cm^2 **e** The maximum compressive (black circles) and tensile (gray squares) stresses are plotted as a function of the charge passed.

Figure 6.6 shows a map of the vertical component of the stress vector on initially horizontal control surfaces in the polymer electrolyte from the growing lithium globule. The stress vector is based on the initial area and force relative to a fixed amount of material. The 1D profile of the globule is the colorless region in the lower left portion of the plot. The globule tip lies at a radial position of 0 μm. This stress vector, reported in Pa, is shown by the color in the plot. Stress maps were calculated based on the globule shape after 8.27 C/cm^2, 16.53 C/cm^2, 35.82 C/cm^2, and 54.72 C/cm^2 of lithium was deposited on the lower lithium electrode as shown in Figure 6.6a – d. The plot in Figure 6.6b shows the maximum compressive and tensile stresses in the polymer as a

function of the charge passed. In early stages of growth, the globule grows mainly in height, and, consequently, both the compressive stress at the globule tip and the tensile stresses at the globule perimeter increase substantially between 8.27 and 16.53 C/cm^2 as shown in Figure 6.5e. These stresses relax as the globule broadens in intermediate stages of growth. The maximum compressive stress occurs at a finite distance above the tip, not at the tip. This is a consequence of severe stretching experienced by the electrolyte.

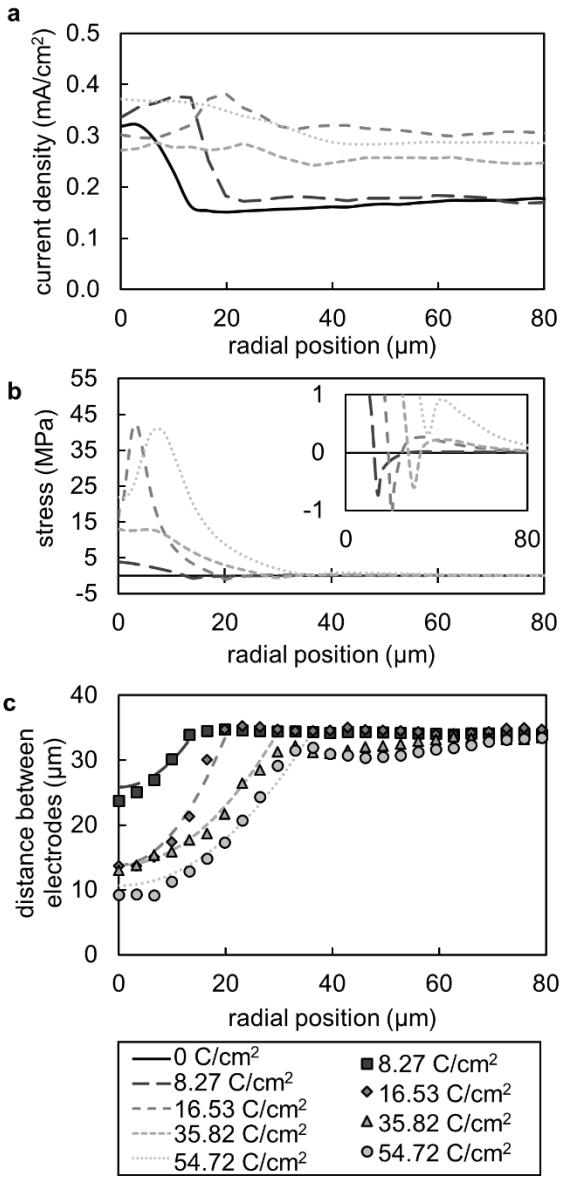

Figure 6.7 **a** Curves showing the current density as a function of the radial distance from the globule tip for five stages of dendrite growth. **b** The stress at the lithium-polymer interface as a function of radial distance from the globule tip. Note that the radial position at which the stress becomes negative aligns with the maximum current density for the subsequent time step shown in part **a**. The inset shows a magnified view of the stresses near zero MPa. The negative, or tensile, stresses are evident in this plot. **c** The parabolic

fits to the lithium globule used to simulate the stress in the block copolymer electrolyte (lines) and the corresponding electrolyte thickness data from the X-ray tomograms (markers).

The current density maps shown in Figure 6.5 were radially averaged about the globule tip and the resulting curves are shown in Figure 6.7a. The peak current density shifts from the globule tip towards the perimeter as the globule grows. When the charge passed is less than 16.53 C/cm^2, the current density at radial positions between 20 and 80 μm away from the globule center is about 0.175 mA/cm^2 as expected based on the potentiostat setting. During the later stages of deposition, the current density at radial positions between 50 and 80 μm away from the globule center increases to a value as high as 0.3 mA/cm^2. The cause of this increase in average current density is unknown. It is worth noting however, that the thickness of the lithium layer deposited based on the potentiostat setting at this juncture is 48 μm, which is substantially larger than the thickness of the electrolyte. Small imperfections in the cell may influence local current densities in this regime.

The vertical component of the stress vector at the lithium-polymer interface is plotted as a function of radial position in Figure 6.7b. Stress at the interface increases substantially as the globule grows significantly in height. These stresses in the electrolyte relax as the globule broadens in intermediate and late stages of growth. At later stages, stress at the interface peaks at a radial position of 6 μm. This is due to the delocalization of the stress maximum away from the tip as described above. Figure 6.7c shows the radially averaged distance between the electrodes extracted from the X-ray microtomography images and the corresponding parabolic fits used to simulate the stresses in the polymer. In Figure 6.7b, the stress dips below zero at radial positions that align with the edge of the globule as shown in Figure 6.7c. Furthermore, the radial positions that have the peak current density shown in Figure 6.7a align with the radial positions that show negative, or tensile, stresses in Figure 6.7b. In the latest stage of globule growth, charge passed equals 54.72 C/cm^2, the stresses at the globule perimeter are compressive and there is no longer a corresponding peak in the current density (Figure 6.7a).

Based on the theory developed by Newman and Monroe, one would expect for the deposition kinetics of lithium to slow in regions of compressive stress and quicken in regions of tensile stress [49]. Consistently, we see that the globule broadens as lithium is preferentially deposited at the globule perimeter. As the globule continues to grow, the stresses at the globule tip relax slightly, likely due to the flattening of the globule tip. Importantly, one would expect for the geometric current concentration effect at the globule tip to lessen as the globule tip flattens [42].

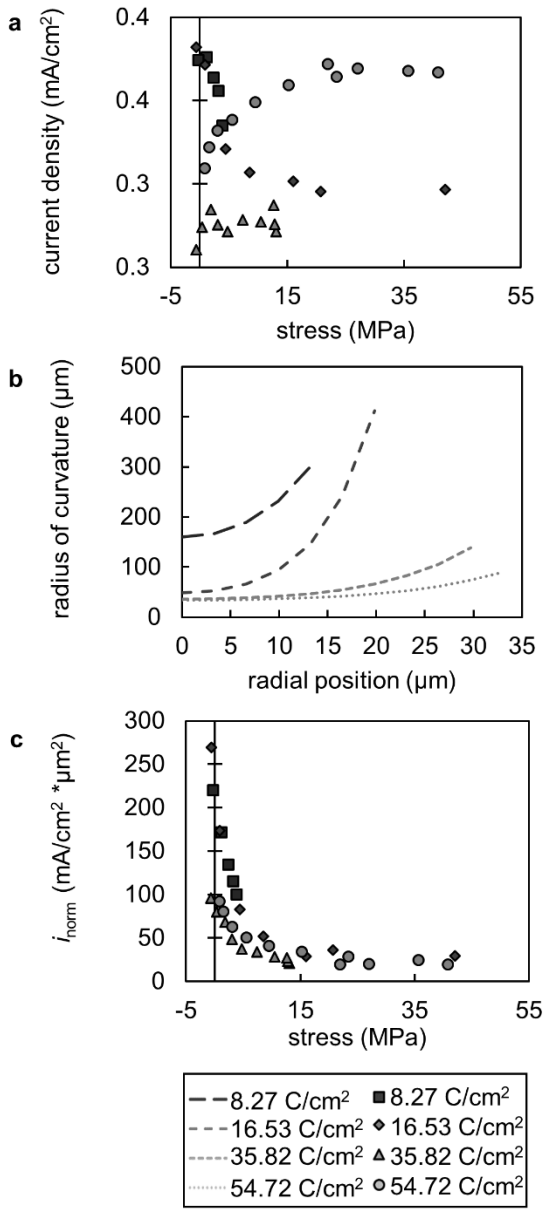

Figure 6.8 **a** The current density does not directly correlate to the stress at the lithium-polymer interface. **b** The radius of curvature of the lithium metal on the globule is shown as a function of the distance from the globule tip. It is minimized at the globule tip and increases with radial position. **c** The normalized current density at a given radial position is plotted against the corresponding stress at that position.

In Figure 6.8a, we plot local current density versus local stress. Current density does not show a strong dependence on stress in this plot. In early stages, the current density appears to decrease with increasing stress, as expected. However, in later stages of growth, the current density appears to increase with stress. An important parameter to consider in this case is the radius of curvature of the growing dendrite. The dendrite broadens as it grows, lessening the driving force for dendrite growth since current tends to concentrate at regions with small radii of curvature. Therefore, it is

important to normalize the current density for this changing radius of curvature at the lithium electrode. The charge density, C, at the surface of a conductor is known to be approximately proportional to the fourth root of the Gaussian curvature, K, of the surface in an electrostatic system [45,46].

$$C \propto \sqrt[4]{K}. \tag{8}$$

The Gaussian curvature for a sphere is:

$$K = \frac{1}{R^2} \tag{9}$$

where R is the radius of the sphere, or the radius of curvature. Therefore, in the simplest model, one would expect the local current density at a given radial position, i_r, to be proportional to the charge density, or

$$i_r \propto \frac{1}{\sqrt{R_r}} \tag{10}$$

where R_r is the radius of curvature at radial position r. Additionally, one would expect for the current density to be inversely proportional to the distance between the electrodes, t_p, due to ohmic losses. To account for these factors, we normalize the local current density as follows,

$$i_{norm} = i_r t_p \sqrt{R_r}\,. \tag{11}$$

It is important to note that we have assumed that the charge density on the electrode surface in our dynamic system is similar to that in an electrostatic system. The radius of curvature is calculated from the parabolic fit to the lithium-polymer interface. Figure 6.8b shows the radius of curvature as a function of radial position. The normalized current density is shown as a function of stress at four different stages of globule growth in Figure 6.8c. In all cases, the normalized current density decreases as the stress increases meaning that the measured current density is lower than geometric effects can account for in regions of high local stress. This is consistent with the theory that suggests that compressive stresses at the lithium-polymer interface should slow lithium deposition kinetics.

In summary, there are several compounding effects that influence the deposition kinetics of lithium on a growing lithium globule in a solid polymer electrolyte membrane. First, as the electrolyte modulus increases, the energetic penalty for electrodeposition of lithium at a globular tip increases. Additionally, there is an energetic driving force for deposition at the globule perimeter. The combination of these effects leads to a broadening of the lithium globule which consequently reduces the current concentration effect at the globule tip. Given this information, it is sensible that relatively small increases in electrolyte modulus can have a large influence on the growth rate of lithium globules.

6.4 Conclusion

The growth of lithium globules through a polystyrene – *b* – poly(ethylene oxide) block copolymer electrolyte was monitored in symmetric lithium – polymer – lithium cells using hard X-ray microtomography. The change in globule height, volume, and projected area were measured as a function of the amount of lithium deposited in the region local to the growing globule. The local current density was mapped in the vicinity of a growing globule by measuring the amount of charge deposited at every location as a function of charge time. The current density maps highlight

the delocalization of current density from the globule tip at early stages of growth to the globule perimeter. In late stages of growth, the globule broadened significantly resulting in minimal current concentration on the lithium globule.

Stress profiles in the polymer electrolyte membrane were calculated based on the deformation of the polymer due to globule formation and the modulus of the polymer based on previously reported rheological measurements [163]. The stress profiles showed a region of compressive stress at the globule tip and tensile stress at the globule perimeter. Given this stress profile, one would expect slowed deposition kinetics at the globule tip and more rapid deposition at the perimeter. This is consistent with the experimental current density maps. Furthermore, as the globule broadened, one would expect the geometric current concentration effect caused by the curvature of the growing globule to decrease. This is also consistent with the minimized current concentration shown in the late-stage current density maps. The combination of these effects leads to a significant reduction in growth rate of lithium globules.

6.5 Nomenclature

i_{jk}	Current density at pixel j, k (mA/cm^2)
V_{jk}	Volume of lithium deposited at pixel j, k (cm^3)
ρ	Density of lithium metal (g/cm^3)
F	Faraday's constant (C/mol)
M_{Li}	Molecular weight of lithium metal (g/mol)
a	Pixel area (cm^2)
t	Time (s)
r	Radial position (μm)
R	Initial radial position (μm)
$\boldsymbol{\sigma}$	Cauchy stress tensor
E	Young's modulus (Pa)
ν	Poisson's ratio
I	Identity tensor
F	Deformation gradient
A	Volume change of electrolyte in control volume (m^3)
t_{Li}	Thickness of lithium deposited (μm)
V_g	Volume of lithium globule (μm^3)
C	Charge density
K	Gaussian curvature
R	Radius of curvature
R_r	Radius of curvature at radial position r
i_r	Current density at radial position r (mA/cm^2)
i_{norm}	Normalized current density ($mA/cm^2 * \mu m^{3/2}$)
t_p	Distance between lithium electrodes (μm)

6.6 Acknowledgements

Primary funding for the work was provided by the Electron Microscopy of Soft Matter Program from the Office of Science, Office of Basic Energy Sciences, Materials Sciences and Engineering Division of the U.S. Department of Energy under Contract No. DE-AC02-05CH11231 (KC11BN). Hard X-ray microtomography experiments were performed at the

Advanced Light Source which is supported by the Director, Office of Science, Office of Basic Energy Sciences, of the U.S. Department of Energy under Contract No. DE-AC02-05CH11231. Katherine J. Harry was supported by a National Science Foundation Graduate Research Fellowship. Kenneth Higa was supported by the Assistant Secretary for Energy Efficiency and Renewable Energy, Vehicle Technologies Office, of the U.S. Department of Energy under Contract No. DE-AC02-05CH11231, under the Advanced Battery Materials Research (BMR) Program. We would also like to acknowledge Professor Bryan McCloskey and Professor John Newman for their helpful technical discussion and advice.

6.7 Supplementary Information

Image Number	Charge passed before image (C/cm^2)	Charge passed ($mA*h/cm^2$)	Ring Current (mA)	Beam energy (keV)	Number of angles	Exposure time (ms)	Rotation angle range
1	0.00	0.00	500	20	1025	350	180
2	2.76	0.77	500	20	1025	350	180
3	5.51	1.53	500	20	1025	450	180
4	8.27	2.30	500	20	1025	350	180
5	11.02	3.06	500	20	1025	300	180
6	13.78	3.83	500	20	1025	300	180
7	16.53	4.59	500	20	1025	300	180
8	19.29	5.36	500	20	1025	1000	180
9	22.04	6.12	35	22	2049	1500	360
10	24.80	6.89	35	22	2049	1500	360
11	27.55	7.65	35	22	4097	1500	360
12	30.31	8.42	35	22	4097	1500	360
13	33.07	9.18	34	22	4097	1500	360
14	35.82	9.95	35	22	4097	1500	360
15	54.72	15.20	33	22	4097	1500	360
16	124.33	34.54	500	22	2049	600	180

Table 6.S1 **X-ray tomography imaging parameters used to obtain images**. Note that the amount of charge passed before the image does not include charge from the preliminary cycling. The average thickness of the layer of deposited lithium is calculated via Faraday's law.

Chapter 7 – Summary

The purpose of this work was to learn about the influence of mechanical rigidity of the electrolyte on the formation of lithium dendrites. First, a robust technique was identified to image the interior of electrochemical cells without requiring intensive cell disassembly or exposure of the sample materials to humid air. Initial studies identified the morphology of lithium dendrites grown in symmetric lithium cells using a 240 – 260 kg/mol polystyrene – *block* – poly(ethylene oxide) copolymer electrolyte with LiTFSI salt. Early studies showed that dendrites formed in these systems have a significantly different morphology than conventional dendrites. Specifically, the lithium dendrites have a globular structure, with a large portion of the globule volume located inside of the lithium electrode, beneath the lithium – electrolyte interface. Additionally, the location of the globular dendrites appeared to be correlated to impurity particles initially present in the lithium foil used as the electrodes in these studies.

Next, an experiment was performed showing the influence of operating temperature on the cycle life and dendrite morphology of symmetric lithium cells. Polystyrene – *block* – poly(ethylene oxide) block copolymer electrolytes only have reasonable ionic conductivity above the melting point of poly(ethyelene oxide), about 55 °C. Additionally, the modulus of the electrolyte decreases rapidly as the temperature increases past the glass transition temperature of the polystyrene block, about 107 °C. It was found that cells operated at and above the glass transition temperature of polystyrene failed significantly earlier than those cycled at lower temperatures. Additionally, the portion of the dendrite located in the lithium electrode decreased as the temperature was increased. This suggests that the subsurface structures seen are a result of the stiffness of the polymer electrolyte.

Stop-motion X-ray microtomography experiments directly showing the formation and growth of lithium dendrites until cell failure by short-circuit allowed for a more detailed understanding of the growth process. Impurity particles that were initially located at the lithium – electrolyte interface appear to disrupt the smooth deposition of lithium metal on the anode surface resulting in the formation of lithium dendrites and other defects. We hypothesize that the particles disturb the integrity of the protective solid electrolyte interphase (SEI) layer resulting in an inhomogeneous current distribution. Because the thickness of lithium deposited on the electrode between two time points was measurable from the X-ray tomograms, we were able to map the current density, or amount of charge deposited per unit time. These maps showed that the current density delocalized from the tip of a dendrite growing into the block copolymer electrolyte. Conventional dendrite growth models neglect the influence of the electrolyte modulus on the current density. When this is neglected, the current density is always maximized at the dendrite tip. However, in rigid electrolytes, the current density is maximized in regions of tension at the dendrite perimeter. This results in a broadening of the dendrite as it grows, blunting the dendrite tip and significantly slowing its growth.

References

[1] M. Armand and J.-M. Tarascon, Building better batteries, Nature **451**, 7179, 652 (2008).

[2] B. Dunn, H. Kamath, and J.-M. Tarascon, Electrical energy storage for the grid: a battery of choices, Science **334**, 6058, 928 (2011).

[3] E. Tate, M. O. Harpster, and P. J. Savagian, *The electrification of the automobile: from conventional hybrid, to plug-in hybrids, to extended-range electric vehicles* (Citeseer, 2008).

[4] V. T. Program, Multi-year program plan 2011 - 2015, 2010.

[5] N. P. Balsara and J. Newman, Comparing the Energy Content of Batteries, Fuels, and Materials, J Chem Educ **90**, 4, 446 (2013).

[6] M. Doyle, J. Newman, A. S. Gozdz, C. N. Schmutz, and J. M. Tarascon, Comparison of modeling predictions with experimental data from plastic lithium ion cells, Journal of the Electrochemical Society **143**, 6, 1890 (1996).

[7] V. Srinivasan and J. Newman, Design and optimization of a natural graphite/iron phosphate lithium-ion cell, Journal of the Electrochemical Society **151**, 10, A1530 (2004).

[8] D. Aurbach, E. Zinigrad, Y. Cohen, and H. Teller, A short review of failure mechanisms of lithium metal and lithiated graphite anodes in liquid electrolyte solutions, Solid State Ionics **148**, 3, 405 (2002).

[9] J.-M. Tarascon and M. Armand, Issues and challenges facing rechargeable lithium batteries, Nature **414**, 6861, 359 (2001).

[10] G. Girishkumar, B. McCloskey, A. Luntz, S. Swanson, and W. Wilcke, Lithium− air battery: promise and challenges, The Journal of Physical Chemistry Letters **1**, 14, 2193 (2010).

[11] P. G. Bruce, S. A. Freunberger, L. J. Hardwick, and J. M. Tarascon, Li-O-2 and Li-S batteries with high energy storage, Nat Mater **11**, 1, 19 (2012).

[12] S. Evers and L. F. Nazar, New approaches for high energy density lithium–sulfur battery cathodes, Accounts of chemical research **46**, 5, 1135 (2012).

[13] I. Epelboin, M. Froment, M. Garreau, J. Thevenin, and D. Warin, Behavior of Secondary Lithium and Aluminum-Lithium Electrodes in Propylene Carbonate, Journal of The Electrochemical Society **127**, 10, 2100 (1980).

[14] L. Gireaud, S. Grugeon, S. Laruelle, B. Yrieix, and J.-M. Tarascon, Lithium metal stripping/plating mechanisms studies: A metallurgical approach, Electrochemistry communications **8**, 10, 1639 (2006).

[15] R. Selim and P. Bro, Some observations on rechargeable lithium electrodes in a propylene carbonate electrolyte, Journal of The Electrochemical Society **121**, 11, 1457 (1974).

[16] J. S. Dunning, W. H. Tiedemann, L. Hsueh, and D. N. Bennion, A Secondary, Nonaqueous Solvent Battery, Journal of The Electrochemical Society **118**, 12, 1886 (1971).

[17] D. Aurbach, M. Daroux, P. Faguy, and E. Yeager, Identification of surface films formed on lithium in propylene carbonate solutions, Journal of The Electrochemical Society **134**, 7, 1611 (1987).

[18] C. Arbizzani, G. Gabrielli, and M. Mastragostino, Thermal stability and flammability of electrolytes for lithium-ion batteries, Journal of Power Sources **196**, 10, 4801 (2011).

[19] P. Balakrishnan, R. Ramesh, and T. P. Kumar, Safety mechanisms in lithium-ion batteries, Journal of Power Sources **155**, 2, 401 (2006).

[20] D. Fenton, J. Parker, and P. Wright, Complexes of alkali metal ions with poly (ethylene oxide), Polymer **14**, 11, 589 (1973).

[21] P. Bruce and C. Vincent, Polymer electrolytes, J. Chem. Soc., Faraday Trans. **89**, 17, 3187 (1993).

[22] D. T. Hallinan Jr and N. P. Balsara, Polymer electrolytes, Annual Review of Materials Research **43**, 503 (2013).

[23] M. Singh, O. Odusanya, G. M. Wilmes, H. B. Eitouni, E. D. Gomez, A. J. Patel, V. L. Chen, M. J. Park, P. Fragouli, H. Iatrou, N. Hadjichristidis, D. Cookson, and N. P. Balsara, Effect of molecular weight on the mechanical and electrical properties of block copolymer electrolytes, Macromolecules **40**, 13, 4578 (2007).

[24] R. Bouchet, S. Maria, R. Meziane, A. Aboulaich, L. Lienafa, J.-P. Bonnet, T. N. Phan, D. Bertin, D. Gigmes, and D. Devaux, Single-ion BAB triblock copolymers as highly efficient electrolytes for lithium-metal batteries, Nat Mater **12**, 5, 452 (2013).

[25] D. H. Wong, J. L. Thelen, Y. Fu, D. Devaux, A. A. Pandya, V. S. Battaglia, N. P. Balsara, and J. M. DeSimone, Nonflammable perfluoropolyether-based electrolytes for lithium batteries, Proceedings of the National Academy of Sciences **111**, 9, 3327 (2014).

[26] C. Brissot, M. Rosso, J. N. Chazalviel, and S. Lascaud, In Situ Concentration Cartography in the Neighborhood of Dendrites Growing in Lithium/Polymer-Electrolyte/Lithium Cells, Journal of the Electrochemical Society **146**, 12, 4393 (1999).

[27] C. Brissot, M. Rosso, J.-N. Chazalviel, and S. Lascaud, Dendritic growth mechanisms in lithium/polymer cells, Journal of power sources **81**, 925 (1999).

[28] C. Brissot, M. Rosso, J.-N. Chazalviel, and S. Lascaud, Study of the evolution of the Li/electrolyte interface during cycling of Li/polymer batteries, Studies in Surface Science and Catalysis **132**, 947 (2001).

[29] M. Dollé, L. Sannier, B. Beaudoin, M. Trentin, and J.-M. Tarascon, Live scanning electron microscope observations of dendritic growth in lithium/polymer cells, Electrochemical and solid-state letters **5**, 12, A286 (2002).

[30] D. T. Hallinan, S. A. Mullin, G. M. Stone, and N. P. Balsara, Lithium metal stability in batteries with block copolymer electrolytes, Journal of The Electrochemical Society **160**, 3, A464 (2013).

[31] M. Rosso, C. Brissot, A. Teyssot, M. Dolle, L. Sannier, J. M. Tarascon, R. Bouchetc, and S. Lascaud, Dendrite short-circuit and fuse effect on Li/polymer/Li cells, Electrochim Acta **51**, 25, 5334 (2006).

[32] M. Rosso, T. Gobron, C. Brissot, J.-N. Chazalviel, and S. Lascaud, Onset of dendritic growth in lithium/polymer cells, Journal of power sources **97**, 804 (2001).

[33] G. Stone, S. Mullin, A. Teran, D. Hallinan, A. Minor, A. Hexemer, and N. Balsara, Resolution of the modulus versus adhesion dilemma in solid polymer electrolytes for rechargeable lithium metal batteries, Journal of The Electrochemical Society **159**, 3, A222 (2012).

[34] D. A. Porter, K. E. Easterling, and M. Sherif, *Phase Transformations in Metals and Alloys, (Revised Reprint)* (CRC press, 2009).

[35] H. D. Brody, Massachusetts Institute of Technology, 1965.

[36] J. Lipton, M. Glicksman, and W. Kurz, Dendritic growth into undercooled alloy metals, Materials Science and Engineering **65**, 1, 57 (1984).

[37] T. Aoyama, Y. Takamura, and K. Kuribayashi, Dendrite growth processes of silicon and germanium from highly undercooled melts, Metallurgical and Materials Transactions A **30**, 5, 1333 (1999).

[38] P. Galenko and D. Danilov, Model for free dendritic alloy growth under interfacial and bulk phase nonequilibrium conditions, Journal of crystal growth **197**, 4, 992 (1999).

[39] M. C. Flemings, Solidification processing, Metallurgical transactions **5**, 10, 2121 (1974).

[40] J. Gibbs, K. Mohan, E. Gulsoy, A. Shahani, X. Xiao, C. Bouman, M. De Graef, and P. Voorhees, The three-dimensional morphology of growing dendrites, Scientific reports **5**, (2015).

[41] J. Diggle, A. Despic, and J. M. Bockris, The mechanism of the dendritic electrocrystallization of zinc, Journal of The Electrochemical Society **116**, 11, 1503 (1969).

[42] J. Barton and J. M. Bockris, The electrolytic growth of dendrites from ionic solutions, Proceedings of the Royal Society of London. Series A. Mathematical and Physical Sciences **268**, 1335, 485 (1962).

[43] C. Monroe and J. Newman, Dendrite growth in lithium/polymer systems a propagation model for liquid electrolytes under galvanostatic conditions, Journal of The Electrochemical Society **150**, 10, A1377 (2003).
[44] R. A. Serway, R. J. Beichner, and J. W. Jewett, Physics for scientists and engineers with modern physics, (2000).
[45] K. M. Liu, Relation between charge density and curvature of surface of charged conductor, American Journal of Physics **55**, 9, 849 (1987).
[46] K. Bhattacharya, On the Dependence of Charge Density on Surface Curvature of an Isolated Conductor, arXiv preprint arXiv:1509.09252, (2015).
[47] G. V. Samsonov, *Handbook of the Physicochemical Properties of the Elements* (Springer Science & Business Media, 2012).
[48] A. J. Bard, L. R. Faulkner, J. Leddy, and C. G. Zoski, *Electrochemical methods: fundamentals and applications* (Wiley New York, 1980), Vol. 2.
[49] C. Monroe and J. Newman, The impact of elastic deformation on deposition kinetics at lithium/polymer interfaces, J Electrochem Soc **152**, 2, A396 (2005).
[50] M. Watanabe and N. Ogata, Ionic conductivity of polymer electrolytes and future applications, British polymer journal **20**, 3, 181 (1988).
[51] F. S. Bates, Polymer-polymer phase behavior, Science **251**, 4996, 898 (1991).
[52] D. Aurbach, E. Zinigrad, H. Teller, and P. Dan, Factors which limit the cycle life of rechargeable lithium (metal) batteries, Journal of The Electrochemical Society **147**, 4, 1274 (2000).
[53] E. Eweka, J. Owen, and A. Ritchie, Electrolytes and additives for high efficiency lithium cycling, Journal of power sources **65**, 1, 247 (1997).
[54] J. Y. Huang, L. Zhong, C. M. Wang, J. P. Sullivan, W. Xu, L. Q. Zhang, S. X. Mao, N. S. Hudak, X. H. Liu, and A. Subramanian, In situ observation of the electrochemical lithiation of a single SnO2 nanowire electrode, Science **330**, 6010, 1515 (2010).
[55] H. Ghassemi, M. Au, N. Chen, P. A. Heiden, and R. S. Yassar, Real-time observation of lithium fibers growth inside a nanoscale lithium-ion battery, Appl Phys Lett **99**, 12, (2011).
[56] R. Bhattacharyya, B. Key, H. Chen, A. S. Best, A. F. Hollenkamp, and C. P. Grey, In situ NMR observation of the formation of metallic lithium microstructures in lithium batteries, Nat Mater **9**, 6, 504 (2010).
[57] S. Chandrashekar, N. M. Trease, H. J. Chang, L.-S. Du, C. P. Grey, and A. Jerschow, 7Li MRI of Li batteries reveals location of microstructural lithium, Nat Mater **11**, 4, 311 (2012).
[58] A. MacDowell, D. Parkinson, A. Haboub, E. Schaible, J. Nasiatka, C. Yee, J. Jameson, J. Ajo-Franklin, C. Brodersen, and A. McElrone, in *SPIE Optical Engineering+ Applications* (International Society for Optics and Photonics, 2012), pp. 850618.
[59] A. C. Kak and M. Slaney, *Principles of computerized tomographic imaging* (IEEE press, 1988).
[60] T. S. Curry, J. E. Dowdey, and R. C. Murry, *Christensen's physics of diagnostic radiology* (Lippincott Williams & Wilkins, 1990).
[61] B. L. Henke, E. M. Gullikson, and J. C. Davis, X-ray interactions: photoabsorption, scattering, transmission, and reflection at E= 50-30,000 eV, Z= 1-92, Atomic data and nuclear data tables **54**, 2, 181 (1993).
[62] A. Groso, M. Stampanoni, R. Abela, P. Schneider, S. Linga, and R. Müller, Phase contrast tomography: an alternative approach, Appl Phys Lett **88**, 21, 214104 (2006).
[63] M. Langer, P. Cloetens, J.-P. Guigay, and F. Peyrin, Quantitative comparison of direct phase retrieval algorithms in in-line phase tomography, Medical physics **35**, 10, 4556 (2008).
[64] P. Cloetens, W. Ludwig, J. Baruchel, D. Van Dyck, J. Van Landuyt, J. Guigay, and M. Schlenker, Holotomography: Quantitative phase tomography with micrometer resolution using hard synchrotron radiation x rays, Appl Phys Lett **75**, 19, 2912 (1999).

[65] Beamline 8.3.2 Manual, 2015.
[66] J. Roth, J. Eller, and F. N. Buchi, Effects of Synchrotron Radiation on Fuel Cell Materials, Journal of the Electrochemical Society **159**, 8, F449 (2012).
[67] J. Eller and F. N. Buchi, Polymer electrolyte fuel cell performance degradation at different synchrotron beam intensities, J Synchrotron Radiat **21**, 82 (2014).
[68] H. D. Barth, M. E. Launey, A. A. MacDowell, J. W. Ager, and R. O. Ritchie, On the effect of X-ray irradiation on the deformation and fracture behavior of human cortical bone, Bone **46**, 6, 1475 (2010).
[69] DOE, Multi-Year Program Plan 2011 - 2015: Vehicle Technologies Program, (2010).
[70] J. M. Tarascon and M. Armand, Issues and challenges facing rechargeable lithium batteries, Nature **414**, 6861, 359 (2001).
[71] C. L. Yaws, *Yaws' Handbook of Properties of the Chemical Elements* (Knovel.
[72] D. Aurbach, E. Zinigrad, Y. Cohen, and H. Teller, A short review of failure mechanisms of lithium metal and lithiated graphite anodes in liquid electrolyte solutions, Solid State Ionics **148**, 3-4, 405 (2002).
[73] E. Eweka, J. R. Owen, and A. Ritchie, Electrolytes and additives for high efficiency lithium cycling, J Power Sources **65**, 1-2, 247 (1997).
[74] J. B. Goodenough and Y. Kim, Challenges for Rechargeable Li Batteries, Chem Mater **22**, 3, 587 (2010).
[75] S. Kalnaus, A. S. Sabau, W. E. Tenhaeff, N. J. Dudney, and C. Daniel, Design of composite polymer electrolytes for Li ion batteries based on mechanical stability criteria, J Power Sources **201**, 280 (2012).
[76] T. Tatsuma, M. Taguchi, M. Iwaku, T. Sotomura, and N. Oyama, Inhibition effects of polyacrylonitrile gel electrolytes on lithium dendrite formation, J Electroanal Chem **472**, 2, 142 (1999).
[77] C. Monroe and J. Newman, Dendrite growth in lithium/polymer systems - A propagation model for liquid electrolytes under galvanostatic conditions, J Electrochem Soc **150**, 10, A1377 (2003).
[78] M. Z. Mayers, J. W. Kaminski, and T. F. Miller, Suppression of Dendrite Formation via Pulse Charging in Rechargeable Lithium Metal Batteries, The Journal of Physical Chemistry C, (2012).
[79] P. J. Gellings and H. J. M. Bouwmeester, *The CRC Handbook of Solid State Electrochemistry* (CRC Press, 1997).
[80] B. Dunn, H. Kamath, and J. M. Tarascon, Electrical Energy Storage for the Grid: A Battery of Choices, Science **334**, 6058, 928 (2011).
[81] L. Gireaud, S. Grugeon, S. Laruelle, B. Yrieix, and J. M. Tarascon, Lithium metal stripping/plating mechanisms studies: A metallurgical approach, Electrochem Commun **8**, 10, 1639 (2006).
[82] C. Brissot, M. Rosso, J. N. Chazalviel, and S. Lascaud, In situ concentration cartography in the neighborhood of dendrites growing in lithium/polymer-electrolyte/lithium cells, J Electrochem Soc **146**, 12, 4393 (1999).
[83] G. M. Stone, S. A. Mullin, A. A. Teran, D. T. Hallinan, A. M. Minor, A. Hexemer, and N. P. Balsara, Resolution of the Modulus versus Adhesion Dilemma in Solid Polymer Electrolytes for Rechargeable Lithium Metal Batteries, J Electrochem Soc **159**, 3, A222 (2012).
[84] S. Liu, N. Imanishi, T. Zhang, A. Hirano, Y. Takeda, O. Yamamoto, and J. Yang, Lithium Dendrite Formation in Li/Poly(ethylene oxide)-Lithium Bis(trifluoromethanesulfonyl)imide and N-Methyl-N-propylpiperidinium Bis(trifluoromethanesulfonyl)imide/Li Cells, Journal of the Electrochemical Society **157**, 10, A1092 (2010).
[85] M. Dolle, L. Sannier, B. Beaudoin, M. Trentin, and J. M. Tarascon, Live scanning electron microscope observations of dendritic growth in lithium/polymer cells, Electrochem Solid St **5**, 12, A286 (2002).

[86] R. Bhattacharyya, B. Key, H. L. Chen, A. S. Best, A. F. Hollenkamp, and C. P. Grey, In situ NMR observation of the formation of metallic lithium microstructures in lithium batteries, Nat Mater **9**, 6, 504 (2010).
[87] S. Chandrashekar, N. M. Trease, H. J. Chang, L. S. Du, C. P. Grey, and A. Jerschow, Li-7 MRI of Li batteries reveals location of microstructural lithium, Nat Mater **11**, 4, 311 (2012).
[88] T. Tatsuma, M. Taguchi, and N. Oyama, Inhibition effect of covalently cross-linked gel electrolytes on lithium dendrite formation, Electrochim Acta **46**, 8, 1201 (2001).
[89] C. M. Lopez, J. T. Vaughey, and D. W. Dees, Morphological Transitions on Lithium Metal Anodes, J Electrochem Soc **156**, 9, A726 (2009).
[90] I. Yoshimatsu, T. Hirai, and J. Yamaki, Lithium Electrode Morphology during Cycling in Lithium Cells, J Electrochem Soc **135**, 10, 2422 (1988).
[91] A. A. MacDowell, D. Y. Parkinson, A. Haboub, E. Schaible, J. R. Nasiatka, C. A. Yee, J. R. Jameson, J. B. Ajo-Franklin, C. R. Brodersen, and A. J. McElrone, in *SPIE Optics and Photonics Conference*San Jose, 2012), pp. 850618.
[92] A. Groso, M. Stampanoni, R. Abela, P. Schneider, S. Linga, and R. Muller, Phase contrast tomography: An alternative approach, Appl Phys Lett **88**, 21, (2006).
[93] A. M. F. R. N. C. Maia, S. Marchesini, H. A. Padmore, D. Y. Parkinson, J. Pien, A. Schirotzek, C. Yang, in *SPIE 7800*2010).
[94] T. C. Frianeza-Kullberg and D. J. Salmon, (Lithium Corporation of America, United States, 1988).
[95] C. Brissot, M. Rosso, J. N. Chazalviel, and S. Lascaud, in *Studies in Surface Science and Catalysis*, edited by N. O. Yasuhiro Iwasawa, and K. Hironobu (Elsevier, 2001), pp. 947.
[96] M. Rosso, E. Chassaing, J. N. Chazalviel, and T. Gobron, Onset of current-driven concentration instabilities in thin cell electrodeposition with small inter-electrode distance, Electrochim Acta **47**, 8, 1267 (2002).
[97] M. Rosso, T. Gobron, C. Brissot, J. N. Chazalviel, and S. Lascaud, Onset of dendritic growth in lithium/polymer cells, J Power Sources **97-8**, 804 (2001).
[98] S. A. Mullin, G. M. Stone, A. Panday, and N. P. Balsara, Salt Diffusion Coefficients in Block Copolymer Electrolytes, Journal of the Electrochemical Society **158**, 6, A619 (2011).
[99] P. G. Bruce and C. A. Vincent, Polymer Electrolytes, J Chem Soc Faraday T **89**, 17, 3187 (1993).
[100] A. Panday, S. Mullin, E. D. Gomez, N. Wanakule, V. L. Chen, A. Hexemer, J. Pople, and N. P. Balsara, Effect of Molecular Weight and Salt Concentration on Conductivity of Block Copolymer Electrolytes, Macromolecules **42**, 13, 4632 (2009).
[101] G. Girishkumar, B. McCloskey, A. C. Luntz, S. Swanson, and W. Wilcke, Lithium - Air Battery: Promise and Challenges, J Phys Chem Lett **1**, 14, 2193 (2010).
[102] C. Monroe and J. Newman, Dendrite Growth in Lithium/Polymer Systems, Journal of The Electrochemical Society **150**, 10, A1377 (2003).
[103] J. L. Barton and J. O. Bockris, The Electrolytic Growth of Dendrites from Ionic Solutions, Proceedings of the Royal Society A: Mathematical, Physical and Engineering Sciences **268**, 1335, 485 (1962).
[104] P. Arora, R. E. White, and M. Doyle, Capacity fade mechanisms and side reactions in lithium-ion batteries, Journal of the Electrochemical Society **145**, 10, 3647 (1998).
[105] M. Ebner, F. Marone, M. Stampanoni, and V. Wood, Visualization and quantification of electrochemical and mechanical degradation in Li ion batteries, Science **342**, 6159, 716 (2013).
[106] Y. Qi and S. J. Harris, In Situ Observation of Strains during Lithiation of a Graphite Electrode, Journal of the Electrochemical Society **157**, 6, A741 (2010).
[107] D. S. Eastwood, P. M. Bayley, H. J. Chang, O. O. Taiwo, J. Vila-Comamala, D. J. Brett, C. Rau, P. J. Withers, P. R. Shearing, and C. P. Grey, Three-dimensional characterization of electrodeposited

lithium microstructures using synchrotron X-ray phase contrast imaging, Chemical Communications, (2014).
[108] J.-L. Shui, J. S. Okasinski, P. Kenesei, H. A. Dobbs, D. Zhao, J. D. Almer, and D.-J. Liu, Reversibility of anodic lithium in rechargeable lithium–oxygen batteries, Nature communications **4**, (2013).
[109] K. J. Harry, D. T. Hallinan, D. Y. Parkinson, A. A. MacDowell, and N. P. Balsara, Detection of subsurface structures underneath dendrites formed on cycled lithium metal electrodes, Nat Mater **13**, 1, 69 (2014).
[110] J. Baruchel, P. Bleuet, A. Bravin, P. Coan, E. Lima, A. Madsen, W. Ludwig, P. Pernot, and J. Susini, Advances in synchrotron hard X-ray based imaging, Cr Phys **9**, 5-6, 624 (2008).
[111] B. P. Flannery, H. W. Deckman, W. G. Roberge, and K. L. D'Amico, Three-Dimensional X-ray Microtomography, Science **237**, 4821, 1439 (1987).
[112] C. Monroe and J. Newman, The Impact of Elastic Deformation on Deposition Kinetics at Lithium/Polymer Interfaces, Journal of The Electrochemical Society **152**, 2, A396 (2005).
[113] J. Schindelin, I. Arganda-Carreras, E. Frise, V. Kaynig, M. Longair, T. Pietzsch, S. Preibisch, C. Rueden, S. Saalfeld, and B. Schmid, Fiji: an open-source platform for biological-image analysis, Nature methods **9**, 7, 676 (2012).
[114] C. A. Schneider, W. S. Rasband, and K. W. Eliceiri, NIH Image to ImageJ: 25 years of image analysis, Nat methods **9**, 7, 671 (2012).
[115] B. L. Henke, E. M. Gullikson, and J. C. Davis, X-Ray Interactions - Photoabsorption, Scattering, Transmission and Reflection at E=50-30,000 Ev, Z=1-92 (Vol 54, Pg 181, 1993), Atom Data Nucl Data **55**, 2, 349 (1993).
[116] R. Rauh, K. Abraham, G. Pearson, J. Surprenant, and S. Brummer, A lithium/dissolved sulfur battery with an organic electrolyte, Journal of the Electrochemical Society **126**, 4, 523 (1979).
[117] P. G. Bruce, L. J. Hardwick, and K. Abraham, Lithium-air and lithium-sulfur batteries, MRS bulletin **36**, 07, 506 (2011).
[118] S.-E. Cheon, K.-S. Ko, J.-H. Cho, S.-W. Kim, E.-Y. Chin, and H.-T. Kim, Rechargeable lithium sulfur battery I. Structural change of sulfur cathode during discharge and charge, Journal of The Electrochemical Society **150**, 6, A796 (2003).
[119] K. Abraham and Z. Jiang, A polymer electrolyte-based rechargeable lithium/oxygen battery, Journal of The Electrochemical Society **143**, 1, 1 (1996).
[120] T. Ogasawara, A. Débart, M. Holzapfel, P. Novák, and P. G. Bruce, Rechargeable Li2O2 electrode for lithium batteries, Journal of the American Chemical Society **128**, 4, 1390 (2006).
[121] H. Kitaura and H. Zhou, Electrochemical performance and reaction mechanism of all-solid-state lithium–air batteries composed of lithium, Li 1+ x Al y Ge 2− y (PO 4) 3 solid electrolyte and carbon nanotube air electrode, Energy & Environmental Science **5**, 10, 9077 (2012).
[122] K. G. Gallagher, S. Goebel, T. Greszler, M. Mathias, W. Oelerich, D. Eroglu, and V. Srinivasan, Quantifying the promise of lithium–air batteries for electric vehicles, Energy & Environmental Science **7**, 5, 1555 (2014).
[123] S.-i. Tobishima and J.-i. Yamaki, A consideration of lithium cell safety, Journal of Power Sources **81**, 882 (1999).
[124] H. Honbo, K. Takei, Y. Ishii, and T. Nishida, Electrochemical properties and Li deposition morphologies of surface modified graphite after grinding, Journal of Power Sources **189**, 1, 337 (2009).
[125] J. Weston and B. Steele, Effects of inert fillers on the mechanical and electrochemical properties of lithium salt-poly (ethylene oxide) polymer electrolytes, Solid State Ionics **7**, 1, 75 (1982).
[126] K. Abraham and M. Alamgir, Li+-conductive solid polymer electrolytes with liquid-Like conductivity, Journal of The Electrochemical Society **137**, 5, 1657 (1990).

[127] J. Bates, N. Dudney, G. Gruzalski, R. Zuhr, A. Choudhury, C. Luck, and J. Robertson, Fabrication and characterization of amorphous lithium electrolyte thin films and rechargeable thin-film batteries, Journal of Power Sources **43**, 1-3, 103 (1993).
[128] G. Appetecchi, F. Croce, L. Persi, F. Ronci, and B. Scrosati, Transport and interfacial properties of composite polymer electrolytes, Electrochim Acta **45**, 8, 1481 (2000).
[129] Y. Lu, S. S. Moganty, J. L. Schaefer, and L. A. Archer, Ionic liquid-nanoparticle hybrid electrolytes, Journal of Materials Chemistry **22**, 9, 4066 (2012).
[130] Q. Lu, J. Fang, J. Yang, G. Yan, S. Liu, and J. Wang, A novel solid composite polymer electrolyte based on poly (ethylene oxide) segmented polysulfone copolymers for rechargeable lithium batteries, Journal of Membrane Science **425**, 105 (2013).
[131] M. Armand, J. Chabagno, M. Duclot, P. Vashishta, J. Mundy, and G. Shenoy, Fast Ion Transport in Solids, Polymer Electrolytes: Fundamental and Technological Applications, 131 (1979).
[132] B. Papke, M. Ratner, and D. Shriver, Vibrational spectroscopy and structure of polymer electrolytes, poly (ethylene oxide) complexes of alkali metal salts, Journal of Physics and Chemistry of Solids **42**, 6, 493 (1981).
[133] J. Weston and B. Steele, Thermal history—conductivity relationship in lithium salt-poly (ethylene oxide) complex polymer electrolytes, Solid State Ionics **2**, 4, 347 (1981).
[134] M. Armand, Polymer solid electrolytes-an overview, Solid State Ionics **9**, 745 (1983).
[135] M. Gauthier, D. Fauteux, G. Vassort, A. Belanger, M. Duval, P. Ricoux, J. M. Chabagno, D. Muller, P. Rigaud, and M. Armand, Assessment of Polymer-Electrolyte Batteries for EV and Ambient Temperature Applications, Journal of The Electrochemical Society **132**, 6, 1333 (1985).
[136] S. Zhang, K. H. Lee, J. Sun, C. D. Frisbie, and T. P. Lodge, Viscoelastic properties, ionic conductivity, and materials design considerations for poly (styrene-b-ethylene oxide-b-styrene)-based ion gel electrolytes, Macromolecules **44**, 22, 8981 (2011).
[137] S.-H. Kim, K.-H. Choi, S.-J. Cho, E.-H. Kil, and S.-Y. Lee, Mechanically compliant and lithium dendrite growth-suppressing composite polymer electrolytes for flexible lithium-ion batteries, Journal of Materials Chemistry A **1**, 16, 4949 (2013).
[138] C. Berthier, W. Gorecki, M. Minier, M. Armand, J. Chabagno, and P. Rigaud, Microscopic investigation of ionic conductivity in alkali metal salts-poly (ethylene oxide) adducts, Solid State Ionics **11**, 1, 91 (1983).
[139] C. Wang, T. Sakai, O. Watanabe, K. Hirahara, and T. Nakanishi, All solid-state lithium-polymer battery using a self-cross-linking polymer electrolyte, Journal of the electrochemical society **150**, 9, A1166 (2003).
[140] S. A. Mullin, University of California, Berkeley, 2011.
[141] J.-i. Yamaki, S.-i. Tobishima, K. Hayashi, K. Saito, Y. Nemoto, and M. Arakawa, A consideration of the morphology of electrochemically deposited lithium in an organic electrolyte, Journal of Power Sources **74**, 2, 219 (1998).
[142] M. S. Park, S. B. Ma, D. J. Lee, D. Im, S.-G. Doo, and O. Yamamoto, A highly reversible lithium metal anode, Scientific reports **4**, (2014).
[143] O. Crowther and A. C. West, Effect of electrolyte composition on lithium dendrite growth, Journal of the Electrochemical Society **155**, 11, A806 (2008).
[144] C. Fringant, A. Tranchant, and R. Messina, Behavior of lithium-electrolyte interface during cycling in some ether-carbonate and carbonate mixtures, Electrochim Acta **40**, 4, 513 (1995).
[145] K. Kanamura, S. Shiraishi, H. Tamura, and Z. i. Takehara, X-Ray Photoelectron Spectroscopic Analysis and Scanning Electron Microscopic Observation of the Lithium Surface Immersed in Nonaqueous Solvents, Journal of The Electrochemical Society **141**, 9, 2379 (1994).
[146] A. A. Teran and N. P. Balsara, Thermodynamics of Block Copolymers with and without Salt, The Journal of Physical Chemistry B **118**, 1, 4 (2013).

[147] F. Maia, A. MacDowell, S. Marchesini, H. A. Padmore, D. Y. Parkinson, J. Pien, A. Schirotzek, and C. Yang, in *SPIE Optical Engineering+ Applications* (International Society for Optics and Photonics, 2010), pp. 78000F.
[148] C. M. López, J. T. Vaughey, and D. W. Dees, Morphological transitions on lithium metal anodes, Journal of The Electrochemical Society **156**, 9, A726 (2009).
[149] C. Monroe and J. Newman, The effect of interfacial deformation on electrodeposition kinetics, Journal of The Electrochemical Society **151**, 6, A880 (2004).
[150] D. Fesko and N. Tschoegl, in *Journal of Polymer Science Part C: Polymer Symposia* (Wiley Online Library, 1971), pp. 51.
[151] R. Cohen and N. Tschoegl, Comparison of the Dynamic Mechanical Properties of Two Styrene-Butadiene-Styrene Triblock Copolymers with 1, 2-and 1, 4-Polybutadiene Center Blocks, Transactions of The Society of Rheology (1957-1977) **20**, 1, 153 (1976).
[152] J. Rosedale and F. Bates, Rheology of ordered and disordered symmetric poly (ethylenepropylene)-poly (ethylethylene) diblock copolymers, Macromolecules **23**, 8, 2329 (1990).
[153] R. H. Colby, Block copolymer dynamics, Current Opinion in Colloid & Interface Science **1**, 4, 454 (1996).
[154] A. J. Patel, S. Mochrie, S. Narayanan, A. Sandy, H. Watanabe, and N. P. Balsara, Dynamic signatures of microphase separation in a block copolymer melt determined by X-ray photon correlation spectroscopy and rheology, Macromolecules **43**, 3, 1515 (2010).
[155] J. D. Ferry, Mechanical properties of substances of high molecular weight. VI. Dispersion in concentrated polymer solutions and its dependence on temperature and concentration, Journal of the American Chemical Society **72**, 8, 3746 (1950).
[156] J. D. Ferry, *Viscoelastic properties of polymers* (John Wiley & Sons, 1980).
[157] C. Lim, R. Cohen, and N. Tschoegl, in *Adv. Chem. Ser.* (American Chemical Society Washington, DC, 1971), p. 397.
[158] D. Fesko and N. Tschoegl, Time-temperature superposition in styrene/butadiene/styrene block copolymers, International Journal of Polymeric Materials **3**, 1, 51 (1974).
[159] X. Ji, K. T. Lee, and L. F. Nazar, A highly ordered nanostructured carbon–sulphur cathode for lithium–sulphur batteries, Nat Mater **8**, 6, 500 (2009).
[160] D. Aurbach, Review of selected electrode–solution interactions which determine the performance of Li and Li ion batteries, Journal of Power Sources **89**, 2, 206 (2000).
[161] E. Peled, The electrochemical behavior of alkali and alkaline earth metals in nonaqueous battery systems—the solid electrolyte interphase model, Journal of The Electrochemical Society **126**, 12, 2047 (1979).
[162] A. Lisowska-Oleksiak, The interface between lithium and poly (ethylene-oxide), Solid State Ionics **119**, 1, 205 (1999).
[163] N. S. Schauser, K. J. Harry, D. Y. Parkinson, H. Watanabe, and N. P. Balsara, Lithium Dendrite Growth in Glassy and Rubbery Nanostructured Block Copolymer Electrolytes, Journal of The Electrochemical Society **162**, 3, A398 (2015).
[164] A. Ferrese, P. Albertus, J. Christensen, and J. Newman, Lithium Redistribution in Lithium-Metal Batteries, Journal of The Electrochemical Society **159**, 10, A1615 (2012).
[165] A. Ferrese and J. Newman, Mechanical Deformation of a Lithium-Metal Anode Due to a Very Stiff Separator, Journal of The Electrochemical Society **161**, 9, A1350 (2014).
[166] A. Ferrese and J. Newman, Modeling Lithium Movement over Multiple Cycles in a Lithium-Metal Battery, Journal of The Electrochemical Society **161**, 6, A948 (2014).
[167] N. Hadjichristidis, H. Iatrou, S. Pispas, and M. Pitsikalis, Anionic polymerization: High vacuum techniques, J Polym Sci Pol Chem **38**, 18, 3211 (2000).

[168] R. P. Quirk, J. Kim, C. Kausch, and M. S. Chun, Butyllithium-initiated anionic synthesis of well-defined poly(styrene-block-ethylene oxide) block copolymers with potassium salt additives, Polym Int **39**, 1, 3 (1996).
[169] D. Aurbach, Advanced Batteries: A Dynamic Field Invited Papers on the Science, Research, and Development, Journal of The Electrochemical Society **162**, 14, A2379 (2015).
[170] K. J. Harry, X. X. Liao, D. Y. Parkinson, A. M. Minor, and N. P. Balsara, Electrochemical Deposition and Stripping Behavior of Lithium Metal across a Rigid Block Copolymer Electrolyte Membrane, Journal of the Electrochemical Society **162**, 14, A2699 (2015).
[171] M. Schlesinger and M. Paunovic, *Modern electroplating* (John Wiley & Sons, 2011), Vol. 55.
[172] B. O'Regan, D. T. Schwartz, S. M. Zakeeruddin, and M. Grätzel, Electrodeposited Nanocomposite n–p Heterojunctions for Solid-State Dye-Sensitized Photovoltaics, Advanced Materials **12**, 17, 1263 (2000).
[173] M. P. Zach, K. H. Ng, and R. M. Penner, Molybdenum nanowires by electrodeposition, Science **290**, 5499, 2120 (2000).
[174] A. Brenner, *Electrodeposition of alloys: principles and practice* (Elsevier, 2013), Vol. 1.
[175] M. Matsushita, M. Sano, Y. Hayakawa, H. Honjo, and Y. Sawada, Fractal structures of zinc metal leaves grown by electrodeposition, Physical review letters **53**, 3, 286 (1984).
[176] M. W. Schulze, L. D. McIntosh, M. A. Hillmyer, and T. P. Lodge, High-Modulus, High-Conductivity Nanostructured Polymer Electrolyte Membranes via Polymerization-Induced Phase Separation, Nano Lett **14**, 1, 122 (2014).
[177] W. Li, H. Yao, K. Yan, G. Zheng, Z. Liang, Y.-M. Chiang, and Y. Cui, The synergetic effect of lithium polysulfide and lithium nitrate to prevent lithium dendrite growth, Nat Commun **6**, (2015).
[178] K. J. Harry, D. Y. Parkinson, and N. P. Balsara, Failure Analysis of Batteries Using Synchrotron-based Hard X-ray Microtomography, JoVE (Journal of Visualized Experiments), 102, e53021 (2015).
[179] K. Higa and V. Srinivasan, Stress and Strain in Silicon Electrode Models, Journal of the Electrochemical Society **162**, 6, A1111 (2015).

Appendix

A.1 In situ cell design and additional experimental details

Imaging pouch cells using hard X-ray microtomography is relatively simple; however, there are a few key considerations one should keep in mind when designing a sample to achieve the clearest image possible.

First, image quality is improved when all of the sample bulk (including pouch material) lies within the horizontal field of view of the lens. For example, the 5x magnification lens has a horizontal field of view of about 3.4 mm. Therefore, the sample would ideally have a diameter no larger than 3.4 mm if one wishes to use the 5x magnification lens. This, however, can be rather difficult when making electrochemical cells. Assembling a battery with < 3.4 mm diameter parts inside of a glovebox is not an easy feat. Additionally, samples of this size have a large electrode edge to electrode area ratio, yielding more complex current distributions that can influence the behavior of the battery. After much effort, I never succeeded at making samples at this dimension with reproducible electrochemical performance. Therefore, all samples described in the body of this dissertation have an electrode diameter of at least 8 mm.

Second, if there are very large differences in the photoelectric absorption coefficient of the materials in the sample, then the reconstructed tomograms will likely have significant artifacts that can obscure features in the sample. For example, a conventional pouch cell with lithium metal electrode(s) contains nickel current collectors because nickel is one of the few metals that is highly stable toward lithium metal. Unfortunately, nickel (z_{Ni} = 28) has a significantly higher photoelectric absorption coefficient than lithium (z_{Li} = 3) and the polymer electrolyte (z_C = 6). Therefore, at X-ray energies that yield good contrast between the lithium and polymer electrolyte (20 – 25 keV), the nickel metal is opaque to the X-ray beam. Therefore, the nickel blocks the beam, preventing the collection of useful data about the structure of the lithium and polymer electrolyte. The tomograph shown in Figure 8.1 was taken from a sample where a nickel wire (approximately 100 μm in diameter) was used at the current collector. Despite the small size of the nickel wire, it caused significant artifacts in the image and most of the features in the sample were obscured by image artifacts. Additionally, the pouch material could not create an air-tight seal around the nickel wire. Therefore, the lithium inside the sample was likely exposed to air, causing the mossy appearance of lithium seen in Figure A.1. If one wants a sample that can be cycled in the beam, it is important that any nickel inside the pouch cell is positioned such that it does not block the path of the incident X-rays.

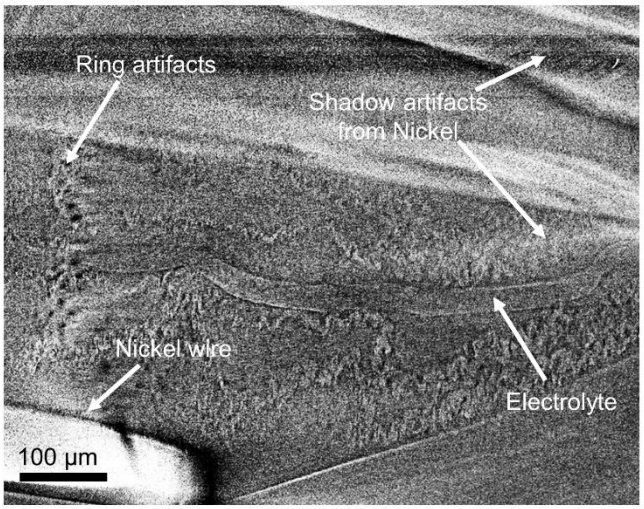

Figure A.1 Nickel current collectors typically used against lithium in pouch cells cause imaging artifacts in X-ray microtomography images. This representative image shows how the artifacts from the nickel obscure many of the features in the image.

Given these challenges, I settled on the sample design shown in Figure A.2 b for my in situ studies. This design moves the nickel current collectors away from the path of the beam while maintaining a geometry that is very similar to a conventional pouch cell (a conventional pouch cell is shown schematically in Figure A.2 a), reducing the probability of systematic error caused by a large change in sample geometry. The key to this design is the 450 µm thick lithium electrodes. These electrodes create a buffer around the lithium-polymer electrolyte interface so that any artifacts caused by the nickel metal will appear far away from the region that we are interested in imaging. The second key to the design, is that the thick lithium metal electrodes are backed with nickel foil. The sample is then sandwiched between two stiff stainless steel shims to keep the sample as flat as possible. This is important because if the sample is bent, the nickel foil may bend into the beam causing artifacts. Aluminum (z_{Al} = 13) tabs are used to collect current from the stainless steel shims. The aluminum has a low enough photoelectronic absorption coefficient to enable reconstructions with an acceptably small enough amount of noise.

Figure A.2 c shows a tomogram through a sample made using the geometry shown schematically in Figure A.2 b. In addition to the aforementioned changes to the interior of the sample, a piece of aluminum mesh was taped to the top of the pouch cell. This allows one to orient the samples in the same manner from image to image. Additionally, once dendrites began to form in the sample, the position on the aluminum grid below which lithium dendrites were growing was marked with a small ball bearing. The sample was then centered about the marker and a higher magnification lens was used to image this section of the sample. This enabled higher resolution imaging of the region of the sample where interesting things were happening. A tomogram showing a slice through the aluminum grid is shown in Figure A.2 d. The position of a growing dendrite relative to the grid on the exterior of the pouch is also shown.

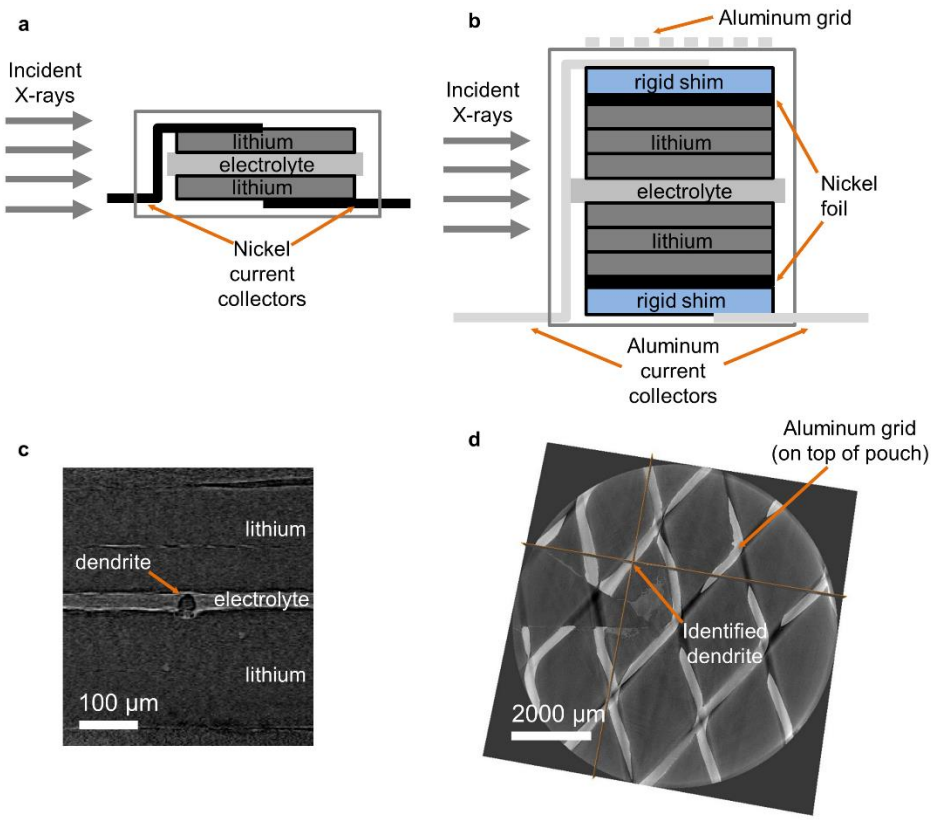

Figure A.2 **a** A schematic of a conventional symmetric lithium – polymer electrolyte – lithium cell with nickel current collectors. **b** The conventional cell geometry was modified to obtain higher quality X-ray microtomography images. The modified cell design for in situ X-ray microtomography imaging is shown here. **c** An X-ray tomogram of a symmetric lithium cell assembled using the geometry shown in part **b**. The stacked layers of lithium are visible in the tomograph. **d** An X-ray tomogram showing a slice through the aluminum grid taped to the top of the pouch. The grid aids in identifying the location of growing dendrites, enabling one to take increased magnification images of the region of interest.

Once I settled on a robust cell design that was compatible with in situ imaging at the hard X-ray microtomography beamline, I could perform experiments like those described in Chapters 5 and 6. Figure A.3 shows a three-dimensional rendering of a region of an in situ sample where seven dendrites are growing. Grain boundaries in the lithium foil are evident in the rendering. The rippled surface of the lithium foil is also visible. This rendering was not included in any publications, but it gives a nice overview of the appearance of a lithium metal anode after electrochemical polarization.

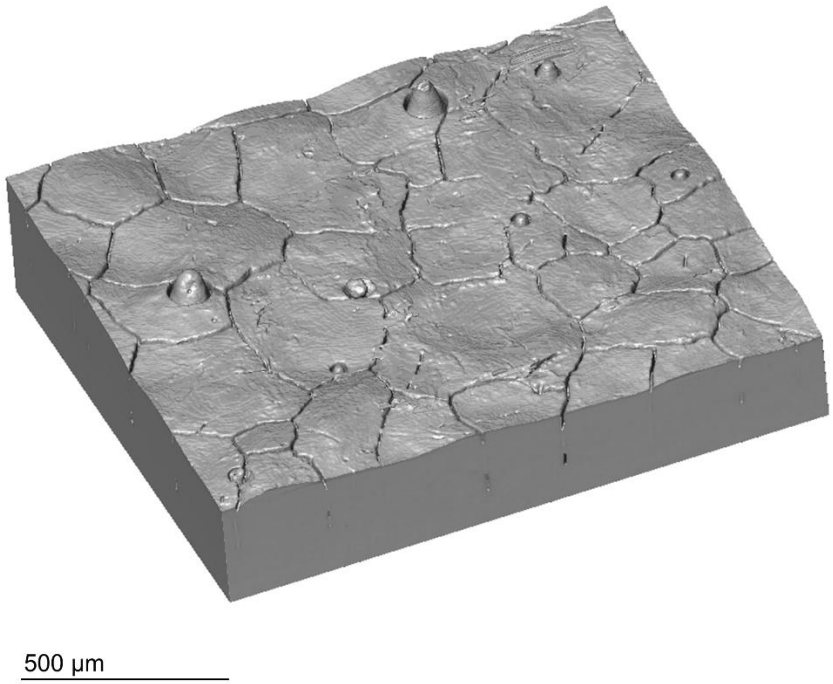

Figure A.3 A three-dimensional rendering of a lithium electrode on which 167 µm of lithium was electrochemically deposited from a solid polymer electrolyte membrane. A variety of dendrites are seen protruding from the electrode surface. The lithium metal grain structure is also apparent.

The amount of lithium deposited at every areal pixel on the lithium metal surface can be measured from the X-ray tomographs. Figure A.4 a and b show the amount of lithium deposited and stripped as a function of the average quantity of charge passed by the potentiostat. If all of the charge that was driven by the potentiostat was transferred in the form of lithium ion oxidation and reduction, the data shown in Figure a and b would lie on the indicated line. This is the case in initial images. However, in later images, the amount of lithium deposited and stripped is larger than one would expect given the amount of charge passed by the potentiostat. It was evident from the tomographs that a larger amount of lithium was transported across the electrolyte in some parts of the sample than in others. It is sensible that dendrites would be more likely to form in regions where a higher than average amount of lithium was transported. The four locations shown in these charts were taken from positions near growing dendrites. These positions were all in the region shown in Figure A.3. Figure A.4 c shows the amount of lithium deposited as a function of the amount of lithium stripped from the electrode at the position directly across the electrolyte. One would expect for these two quantities to be equal. This is the case for all but the final image. The reason for the discrepancy in the last image is unknown. However, several factors may have contributed to this effect. First, the lithium electrode was composed of a stack of three 140 µm thick pieces of lithium foil. Between the second to last and last image, the amount of lithium moved by the potentiostat surpasses 140 µm. The interface between the stacked pieces of lithium foil was visible in the X-ray tomographs, meaning that there was a gap between the foils. Therefore, it is conceivable that the top lithium foil lost contact with the electrolyte as soon as the first 140 µm of lithium was consumed from the top electrode. Lithium would then preferentially strip from other locations on the electrode leading to a discrepancy in the amount of lithium stripped from a given

position on the electrode where lithium oxidation occurred and the amount of lithium deposited at the corresponding position on the electrode where lithium reduction occurred.

Another possible explanation has to do with the impurity particles initially present in the lithium foil. As the lithium is consumed at the electrode where oxidation occurs, the impurity particles become increasingly concentrated in the foil. When the lithium foil is depleted, only the impurities remain. Therefore, when the amount of lithium stripped from the electrode where oxidation occurred surpassed 140 μm, the concentration of impurity particles at the interface of the electrolyte and the electrode becomes high. These impurity particles could result in an inhomogeneous distribution of lithium oxidation rates at the lithium – polymer electrolyte interface.

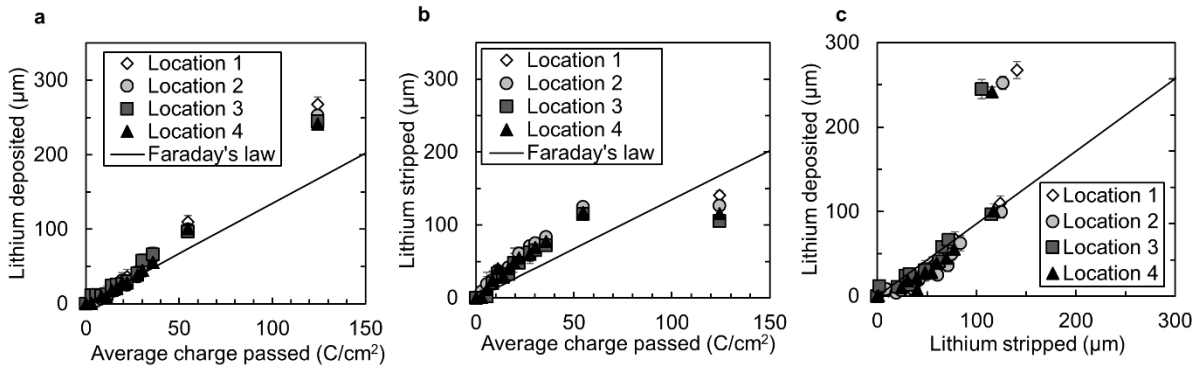

Figure A.4 **a** The amount of lithium deposited in four regions near the positions where lithium globules were observed was measured from X-ray microtomography images. The average amount of lithium deposited on the bottom electrode is given by Faraday's law given a current density of 0.175 mA/cm^2. Note that a higher than average amount of lithium was deposited in the region where a large number of lithium globules were observed. **b** The amount of lithium stripped from the top electrode was measured in the same four locations. The amount of lithium stripped from the top electrode is locally unequal to the amount of lithium deposited on the bottom electrode. **c** The amount of lithium deposited is equal to the amount of lithium stripped within error for all but the final time point.

A.2 Elemental analysis of impurity particles in lithium foil

It was known that even battery grade lithium foil contained impurities. After imaging lithium foil electrodes using hard X-ray microtomography, it was evident that some of the impurities in the lithium foil were in the form of faceted particles with a volume of about 4000 μm^3. The particles are initially distributed uniformly throughout the bulk of the lithium foil. It appears as if particles that are initially located at the interface between the lithium foil and the polymer electrolyte contribute to the nucleation of lithium dendrites and other defects in deposited lithium films as discussed in the main text of this document. Figure A.5 a shows a scanning electron micrograph of a characteristic impurity particle. The lithium metal that initially encased the particle was electrochemically stripped away revealing the particle shape. Figure A.5 b shows three-dimensional renderings made from an X-ray microtomography reconstruction of a different impurity particle that was still embedded in the lithium foil. It is worth noting that while most of the impurity particles in the foil took this octahedral shape, not all of the impurity particles took this shape. Therefore, it is likely that there is some variety in the chemical composition of impurity particles in the lithium foils.

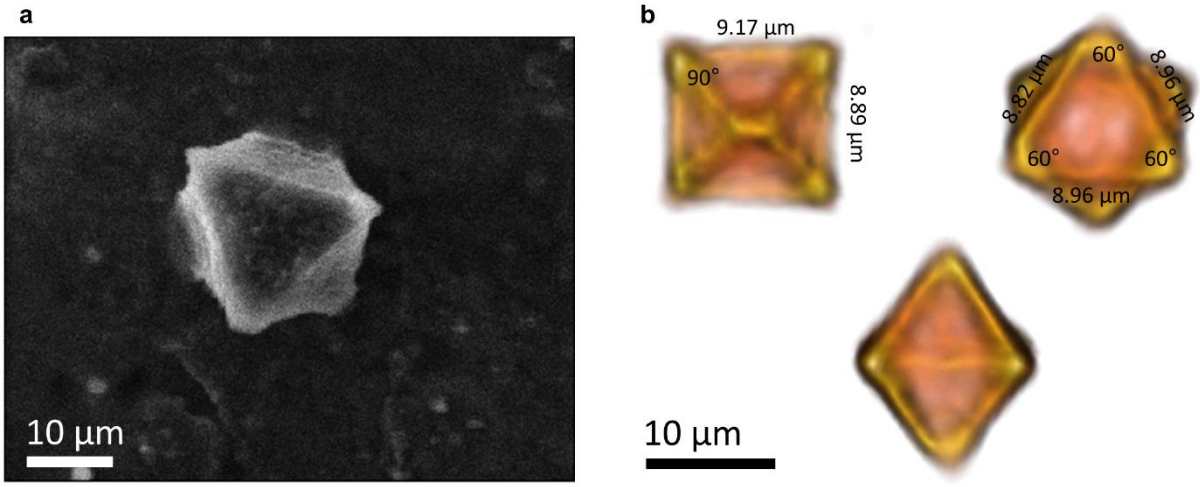

Figure A.5 **a** A scanning electron micrograph of an impurity particle from the lithium foil stuck to a polymer electrolyte film. **b** A three-dimensional rendering of an impurity particle taken from a hard X-ray microtomography reconstruction of a lithium foil electrode.

Energy dispersive spectroscopy was used to try to identify the chemical species present in these impurity particles. Figure A.6 shows a chemical map of the impurity particle shown in Figure A.5 a. The absorption edge of lithium and hydrogen are at energies that are too small to detect using this technique. Bearing that in mind, the chemical mapping suggests that the particle contains primarily oxygen. This means that the particles are probably either lithium oxide or lithium hydroxide. However, this particle was exposed to air for approximately 30 seconds as the sample was transferred into the scanning electron microscope vacuum chamber, therefore, the oxygen signal could come from exposure to air (notably, there is minimal nitrogen signal). The spectra for this particle is shown in Chapter 5, Figure 5.9. The fluorine and sulfur signals are due to the LiTFSI salt in the polymer electrolyte.

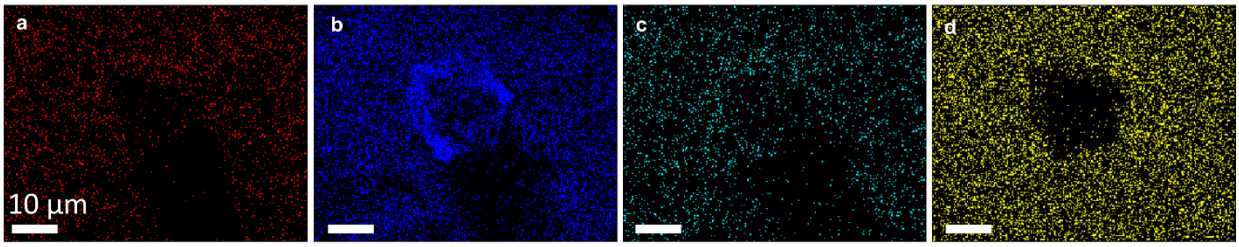

Figure A.6 Energy dispersive spectroscopy maps of the impurity particles pictured in Figure A.5 **a**. **a** Carbon Kα-edge map **b** Oxygen Kα-edge map **c** Fluorine Kα-edge map **d** Sulfur Kα-edge map.

In order to eliminate concern about air exposure, a series of experiments were performed where a gallium ion beam was used to mill into an impurity particle embedded in a lithium foil. The foil was initially imaged using hard X-ray microtomography, so one could identify locations on the lithium foil surface that had an impurity particle buried closely below. Figure A.7 shows a series of scanning electron micrograph images of the cross section of an impurity particle after a gallium ion beam was used to mill into the lithium electrode. All four cross-section images are of the same impurity particle, at different locations in the particle. The faceted edges of the impurity particle are evident in the micrographs. The shape of this particle is different from the particle shown in Figure A.5.

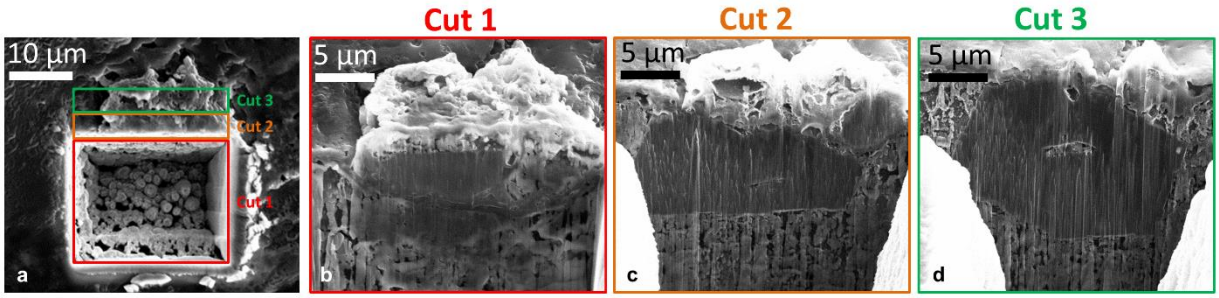

Figure A.7 **a** A scanning electron micrograph showing the regions that were milled using a focused gallium ion beam. **b** A scanning electron micrograph taken at 52° from normal showing the cross-section through the edge of an impurity particle encased in lithium metal. **c** A micrograph showing the cross-section of the impurity particle after a second cut, indicated in part **a**. **d** The cross-section of the impurity particle after the third cut indicated in part **a**.

Unfortunately, the walls of the trench milled with the focused gallium ion beam blocked the signal for energy dispersive analysis yielding unreliable data. To avoid this problem, the focused ion beam was used to isolate a small portion of the impurity particle. A tungsten needle was then lowered down to the impurity particle and platinum was used to adhere the needle to the particle. The gallium beam was then used to detach the section of the particle from the lithium foil sample. The tungsten needle and impurity particle were then moved to a copper grid in the vacuum chamber. Platinum was used to adhere the section of the particle to the copper grid and the gallium focused ion beam was used to detach the tungsten needle from the particle. The scanning electron

micrographs shown in Figure A.8 document the liftout procedure performed on the impurity particle.

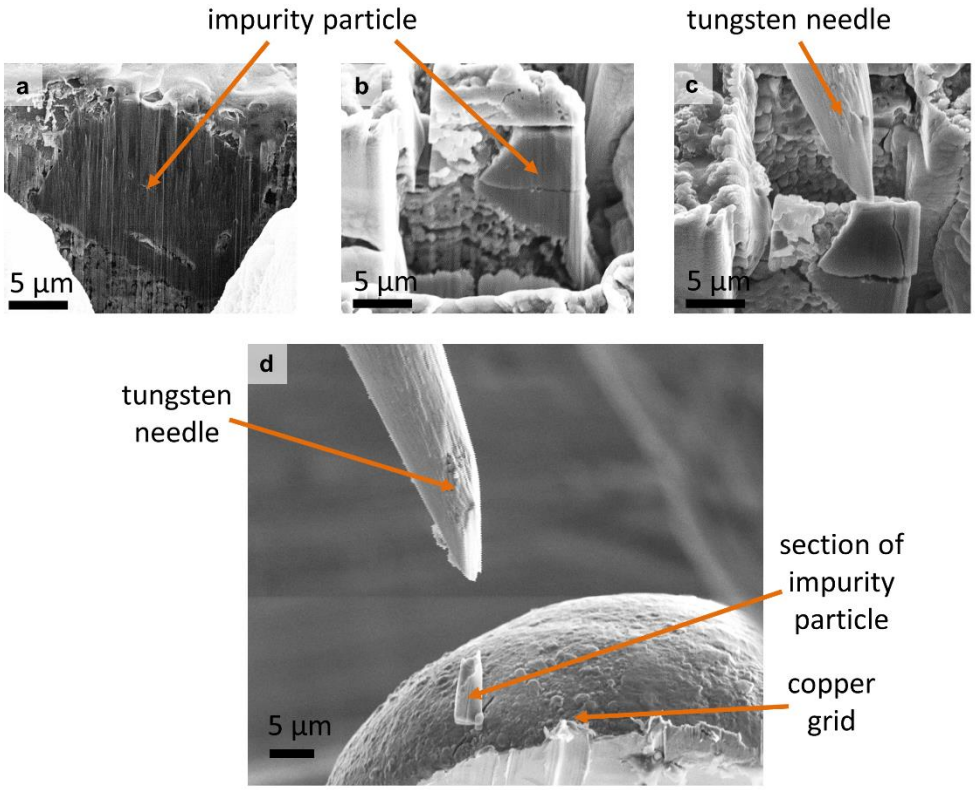

Figure A.8 **Liftout procedure a** A scanning electron micrograph showing the cross-section of an impurity particle embedded in lithium metal. **b** The same impurity particle after a substantial portion of the particle was milled away with a focused gallium ion beam. **c** The tungsten needle used to move a portion of the impurity particle to a copper grid. **d** A section of the impurity particle was affixed to a copper grid with platinum and cut from the tungsten needle.

After a successful liftout, the section of the impurity particle was positioned such that X-rays emitted from the sample during energy dispersive spectroscopy can reach the detector. This liftout procedure was performed on two different impurity particles. Elemental maps of the impurity particle from Figure A.8 are shown in Figure A.9. Carbon and oxygen are the primary elements identified on the sample. Residual platinum from the adhesion process, copper and aluminum from the copper grid, and gallium from the gallium ion beam are also detected. It is possible that the carbon signal could originate from dust on the copper grid.

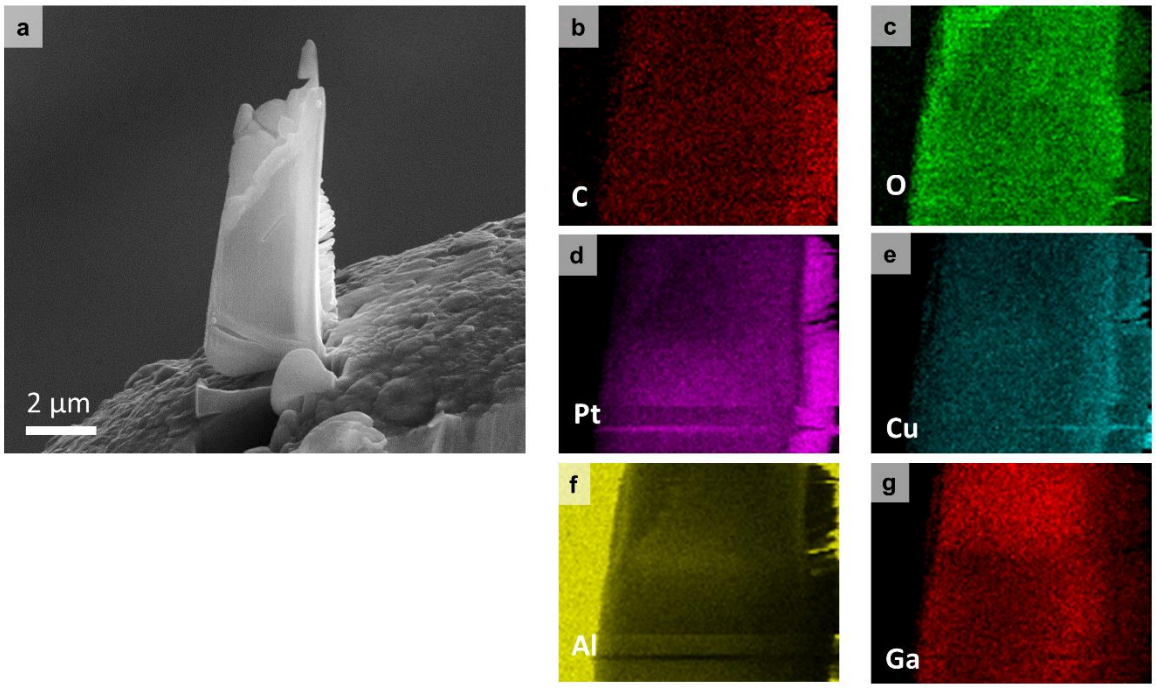

Figure A.9 **Energy dispersive spectroscopy maps of impurity particle a** A scanning electron micrograph showing a small section of an impurity particle adhered with platinum onto a copper grid after a successful liftout. **b** Carbon map **c** Oxygen map **d** Platinum map **e** Copper map **f** Aluminum map **g** Gallium map

Spectra from the energy dispersive spectroscopy experiments on the two impurity particles are shown in Figure A.10. Electron backscatter diffraction was also attempted on the crystallite, but no Kikuchi lines were visible.

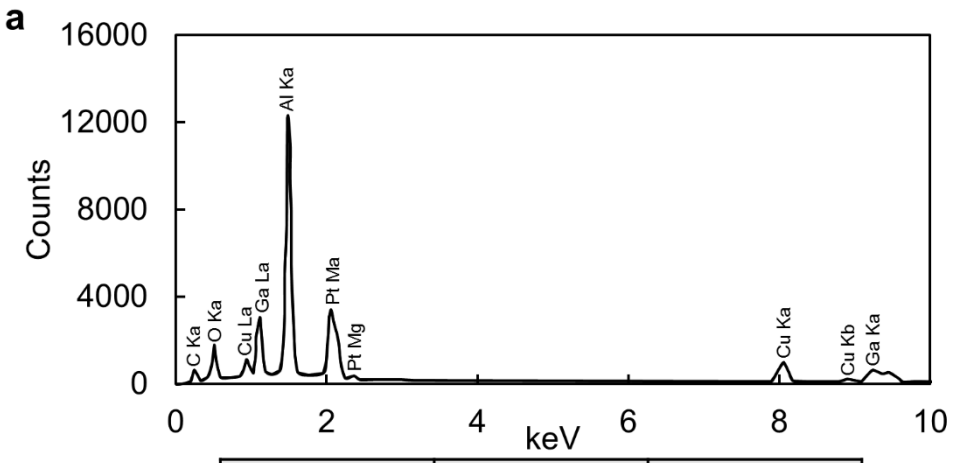

Carbon	21.31 wt%	26.51 at%
Oxygen	78.69 wt%	73.49 at%

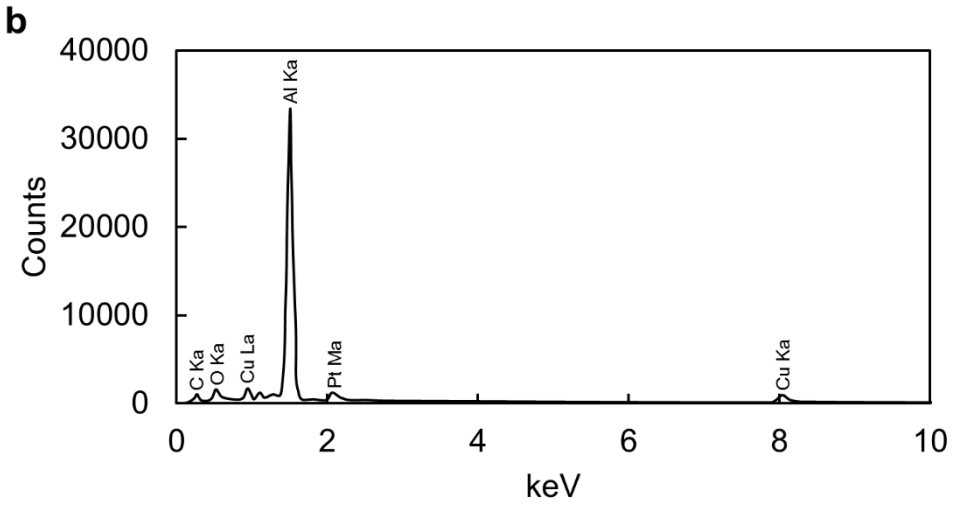

Carbon	25.96 wt%	31.83 at%
Oxygen	74.04 wt%	68.17 at%

Figure A.10 **a** Energy dispersive spectroscopy (EDS) spectra collected from the surface of an impurity particle after liftout. If the signal from the copper, gallium, magnesium, and platinum is disregarded, the wt% and at% of carbon and oxygen are as shown. **b** The EDS spectra for a second impurity particle collected after liftout.

A.3 X-ray microdiffraction

Another method used to attempt to identify the chemical nature of the impurity particles was hard X-ray microdiffraction (beamline 12.3.2 at the Advanced Light Source). 10 keV monochromatic X-rays were used to perform Laue diffraction on a lithium foil. The lithium foil was pouched in a polypropylene pouch that was transparent to visible light. This pouch only protects lithium foil from moisture in the air for approximately one day. This transparent pouch was used because the higher quality laminated aluminum pouch material would also diffract in the beam and likely obscure diffraction from the lithium foil. The X-ray beam was rastered across the sample with a 25 μm step size. A diffraction pattern was collected at each step on the lithium foil surface over a 4 mm by 4 mm area. A characteristic Laue diffraction pattern of the lithium metal foil is shown in Figure A.11 a. The pattern indexed to lithium metal is shown in Figure A.11 b. The grain structure of the lithium foil was mapped from the X-ray microdiffraction experiments as shown in Figure A.11 c.

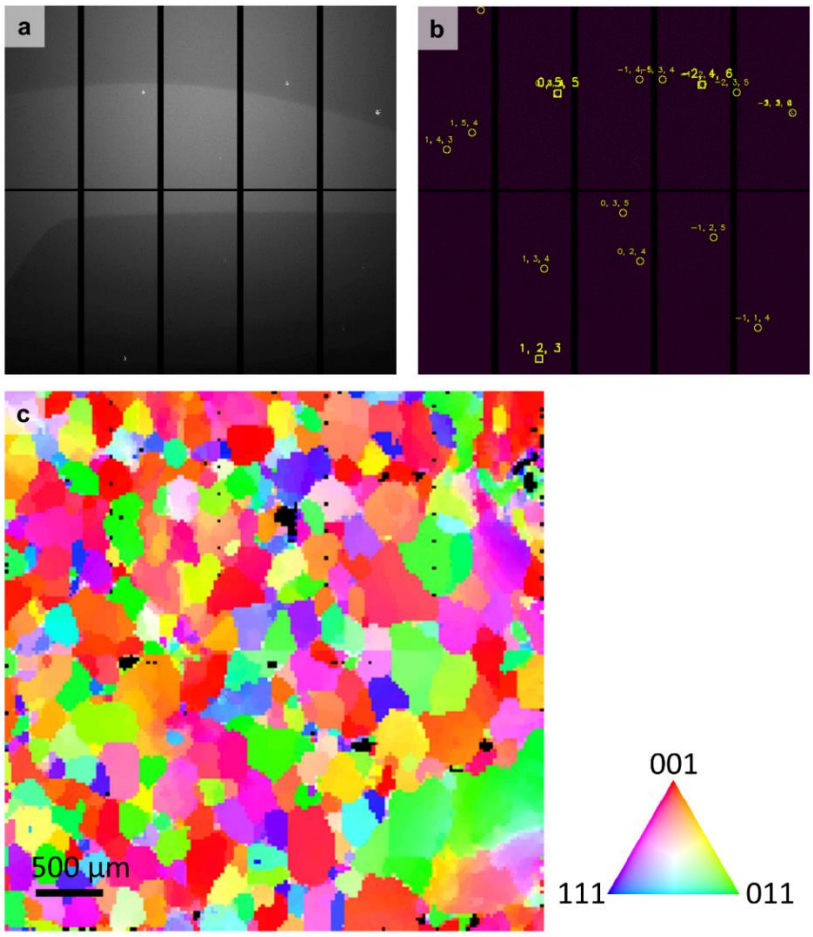

Figure A.11 **a** A Laue diffraction pattern collected from a lithium metal foil. **b** The same pattern indexed to lithium metal. **c** A map of the grain structure and orientation of the lithium metal foil.

A crystalline phase that did not index to lithium metal was also visible in the X-ray microdiffraction experiments. These non-lithium patterns were evenly distributed in the lithium foil and were no larger than the 25 μm step size. It is possible that these non-lithium diffraction patterns belong to the impurity particle phase that is visible in the hard X-ray microtomography images. Unfortunately, these non-lithium diffraction patterns did not index to any common lithium containing compounds. An example of one of these non-lithium diffraction patterns is shown in Figure A.12.

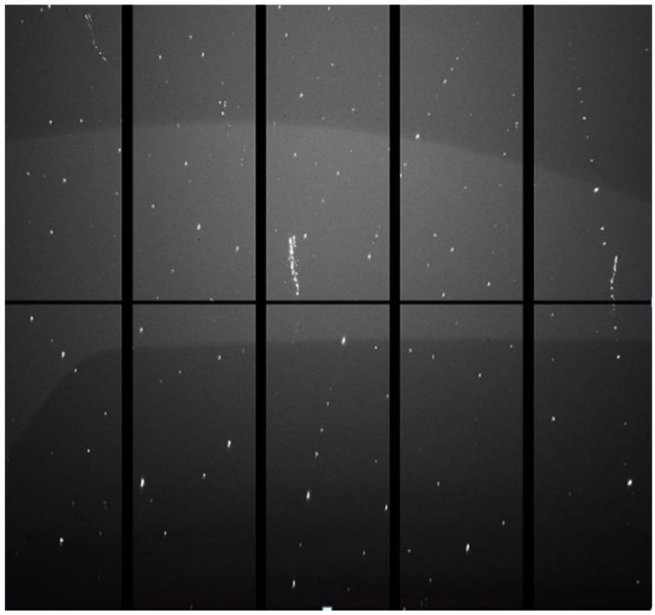

Figure A.12 A Laue diffraction pattern from a non-lithium phase detected in the lithium foil.

A.4 Influence of impurity particle concentration on cell lifetime

Impurity particles initially present in the lithium foil appear to influence the deposition of lithium metal and can nucleate a lithium dendrite. It is therefore reasonable to suspect that altering the concentration of these impurity particles would influence the lifetime of the electrochemical cell. Lithium foil was obtained from an assortment of suppliers claiming different purity levels. A series of symmetric lithium – 240-260 kg/mol SEO – lithium cells were made using five different sources of lithium: lithium chips purchased from MTI, lithium foil purchased from FMC Lithium, lithium chips provided by Hydro Quebec, high purity lithium deposited on copper from Hydro Quebec, and a high purity lithium foil from Hydro Quebec. The purity of each of these foils was not quantified.

Nyquist plots for five samples made using the lithium chips from MTI and five samples made using the high purity lithium foil from Hydro Quebec are shown in Figure A.13. The samples made with the lithium chips from MTI, Figure A.13 a, show a large variation in interfacial resistance while the samples made using the high purity foil from Hydro Quebec show a highly reproducible interfacial resistance, Figure A.13 b. The charge passed before the sample failed by short-circuit was plotted as a function of interfacial resistance for a variety of lithium sources and is shown in Figure A.13 c. Samples that have a long lifetime also have a low interfacial resistance while

samples that have a short lifetime have a high interfacial resistance. However, samples that have a low interfacial resistance do not necessarily have a long lifetime. It is worth noting that a series of samples made using lithium foil from FMC Lithium that were pressed at 90 °C and approximately 1440 psi using a pneumatic hot press for five seconds after assembly had highly reproducible interfacial resistances and achieved a long average lifetime.

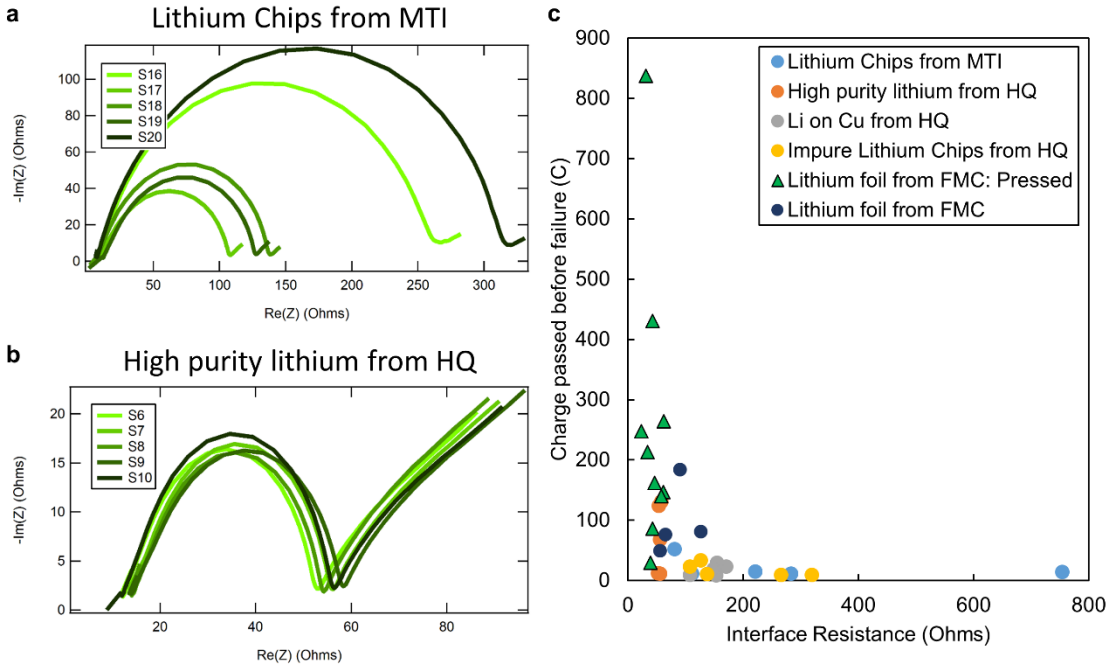

Figure A.13 A Nyquist plot showing the impedance of a series of five symmetric lithium – polymer electrolyte – lithium cells made using **a** lithium chips purchased from MTI **b** high purity lithium foil from Hydro Quebec (HQ). **c** The amount of charge passed before the sample failed by short-circuit is plotted as a function of the interface resistance measured using impedance spectroscopy.

Hard X-ray microtomography was used to image the interior of the samples after they failed by short-circuit. Impurity particles of similar size and shape were found in all of the examined lithium foils. Figure A.14 a shows the average amount of charge passed before failure for three different varieties of lithium. Characteristic voltage and current cycling profiles for samples made with the three different varieties of lithium are shown in Figure A.14 b. Note that the performance of all of these samples is particularly poor, so there may be an unknown systematic error, like a poorly cast polymer electrolyte membrane or poor glovebox conditions, influencing this data. All of these samples were assembled on the same day with the same polymer electrolyte using the same procedure and cell design. A cross-section tomogram through the cycled cells are shown for the three types of lithium. Faceted impurity particles are visible in all three lithium types.

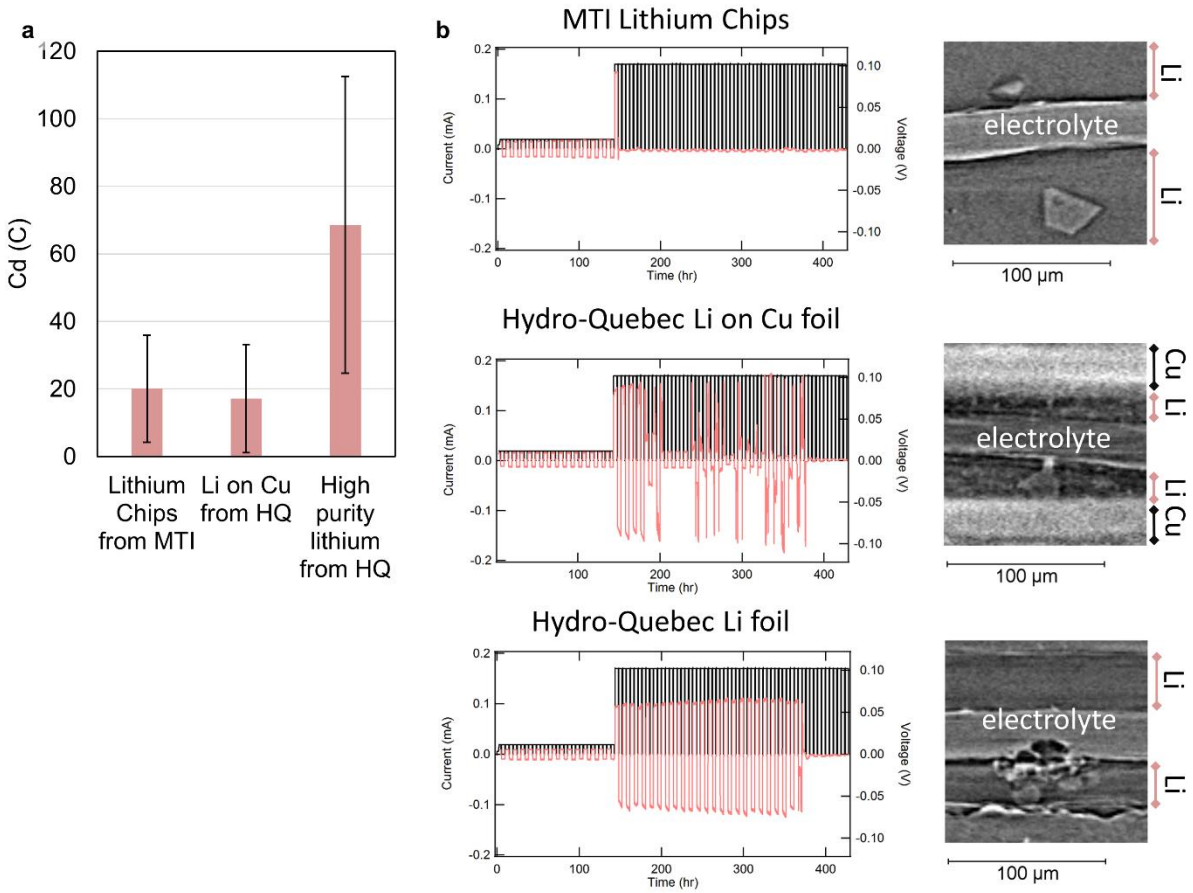

Figure A.14 **a** The total amount of charge passed before samples failed by short-circuit for lithium – polymer electrolyte – lithium symmetric cells made with three different sources of lithium. **b** Characteristic cycling profiles for the three different sources of lithium. Black is the magnitude of the applied current and pink is the voltage response. The cell area was about 0.97 cm^2. Corresponding X-ray tomograms show impurity particles in all of the lithium sources tested.

In an attempt to make a lithium foil free of faceted impurity particles, a lithium deposition chamber was used to deposit a thin film of lithium metal onto a lithium foil substrate. The following procedure was used to evaporate the film of lithium. A new and empty metal boat, used to hold the source lithium metal during the evaporation, was loaded into the lithium evaporator bell jar. The bell jar was evacuated to 1×10^{-6} mbar and the power used to heat the boat was set to 15%, higher than the power used during lithium evaporation. The purpose of this step was to let any impurities off-gas from the boat before attempting to evaporate lithium metal. The bell jar was then refilled with argon and a piece of lithium foil from FMC lithium was rolled into a ball and placed in the boat. The filled boat was then loaded into the evaporator bell jar. A piece of FMC lithium foil was pressed onto nickel foil using a pneumatic press at about 800 psi at room temperature. This pressed foil was used as the substrate for the evaporated lithium film. The target lithium backed with nickel was attached to a rotating sample holder using metal clips and the sample holder was loaded into the evaporator. The glovebox was purged for 5 minutes before

closing the bell jar. The bell jar was then evacuated to 1×10^{-6} mbar. The power setting was slowly ramped up to 13.5% until the lithium was evaporating at a rate of 10 – 11 Å/s as measured using a quartz crystal microbalance. At this point, the shutter that was blocking the lithium sample holder was removed so that lithium evaporating from the boat would deposit on the substrate. Approximately 25 kÅ of lithium was evaporated on the sample. The pressed lithium used as the substrate material is shown in Figure A.15 a. Figure A.15 b shows the sample after the film of lithium was deposited on it. Note that the film appears white and matte, not silver and shiny as would be expected.

Figure A.15 d shows the boat filled with lithium after it was used to evaporate the 25 kÅ of lithium onto the sample. Sludge from the lithium foil floated to the top of the lithium puddle when it melted. A razor blade was used to scrape off the sludge from the lithium source. Figure A.15 e shows the lithium boat after the sludge was removed. Another piece of pressed lithium on nickel was loaded into the lithium evaporator. The glovebox was purged again before closing the bell jar and then the jar was evacuated to 1×10^{-6} mbar. The power to the lithium source was adjusted to achieve a deposition rate of approximately 11 Å/s and then the shutter blocking the substrate was removed. 6.2 kÅ of lithium was deposited on the sample. The resulting film is shown in Figure A.15 c. The film looked shinier than the previous attempt, but it was still white. Every time the bell jar was opened after lithium evaporation, the oxygen level in the glovebox increased slightly (from <0.1 ppm to 0.6 ppm or larger). I suspect that the gaseous lithium reacted with trace impurities in the bell jar before depositing on the lithium metal substrate.

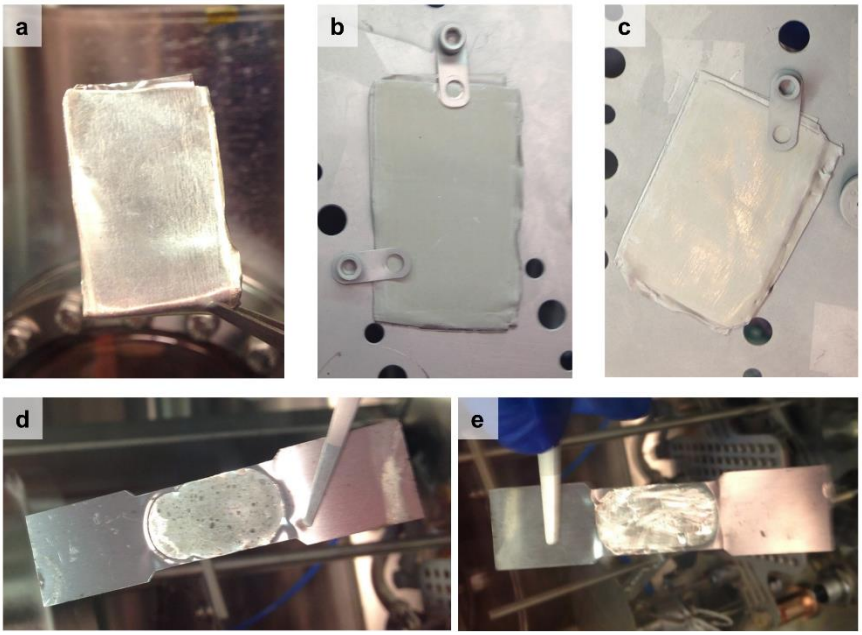

Figure A.15 **a** A lithium foil pressed onto nickel was used as the substrate for lithium evaporation. **b** The lithium foil after 25 kÅ of lithium was evaporated on the sample. **c** A different lithium substrate after 6.2 kÅ of lithium was deposited from the lithium boat shown in part **e**. **d** The boat of lithium metal used as the source after the film shown in part **b** was deposited. **e** The same boat of lithium metal after the sludge was removed with a razor blade. This lithium was used as the source to deposit the film shown in part **c**.

Symmetric lithium – polymer electrolyte – lithium samples using a 240 – 260 kg/mol SEO were assembled with the lithium film shown in Figure A.15 c. Samples made using this deposited lithium failed by short-circuit during the low-current conditioning cycles. When imaged using hard X-ray microtomography, hundreds of multiglobular dendrites were visible. Figure A.16 a shows a tomograph through the plane of the electrolyte for a cycled sample made using the lithium foil shown in Figure A.15 c. Figure A.16 b shows the cross-section view of the same sample. The large number of dendrites that appear in these samples suggest that the deposited lithium film was full of impurity particles that likely resulted in the rapid nucleation of many lithium dendrites.

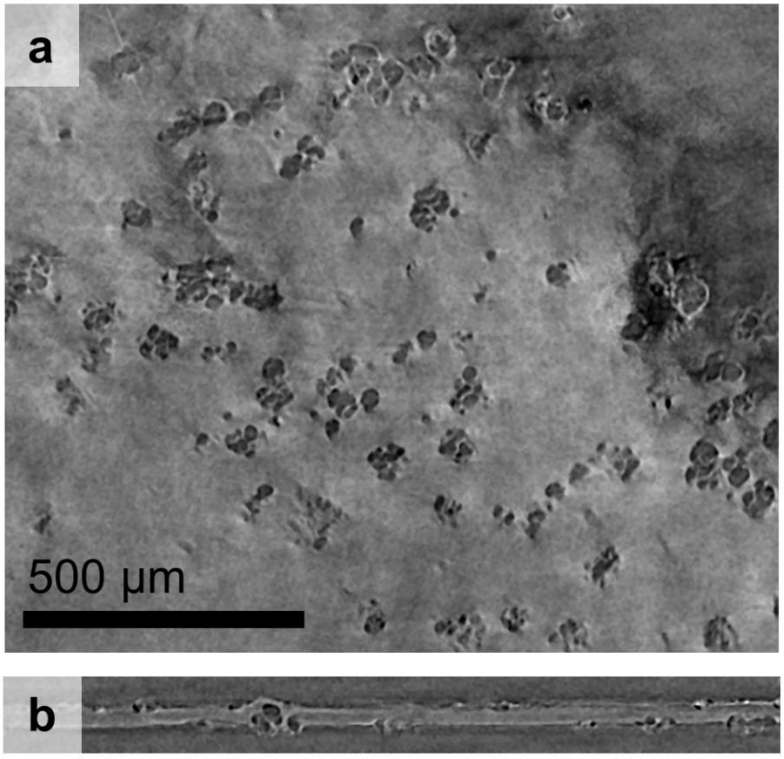

Figure A.16 X-ray tomograms showing many lithium dendrites formed in a lithium symmetric cell with the lithium foil shown in Figure A.15 c. **a** A slice through the sample oriented parallel to the polymer electrolyte, the brighter phase. **b** A slice through the sample oriented normal to the polymer electrolyte. The scale bar applies to both images.